

# Inelastic Photoproduction of $J/\psi$ Mesons at HERA

**Diplomarbeit**

vorgelegt von

**Leif Hendrik Wilden**

II. Institut für Experimentalphysik  
Universität Hamburg

Hamburg  
November 1998



## Abstract

An analysis of inclusive  $J/\psi$  mesons in photoproduction, using the decay channel  $J/\psi \rightarrow \mu^+\mu^-$  is presented. The data have been collected with the H1 detector at the  $ep$  collider HERA and correspond to an integrated luminosity of approximately  $18 \text{ pb}^{-1}$ . The kinematic range covered is  $Q^2 < 1 \text{ GeV}^2$ ,  $40 < W_{\gamma p} < 300 \text{ GeV}$ . The data selection includes the very inelastic region of small inelasticities  $z$ , where a signal was observed. Efficiencies are determined from a mixed Monte Carlo set. Cross sections as function of  $W_{\gamma p}$ ,  $z$  and  $p_{t,J/\psi}^2$  are extracted and compared to recent predictions.

It has been found that data favor higher order predictions in the color octet model with small values of the color octet matrix elements. Leading order color octet calculations show an excess over data at low as well as high inelasticities  $z$ . The color singlet model cannot be ruled out by data yet.

## Kurzzusammenfassung

Eine Analyse inklusiver  $J/\psi$ -Mesonen in Photoproduktion, die den Zerfallskanal  $J/\psi \rightarrow \mu^+\mu^-$  verwendet, wird vorgestellt. Die Daten wurden mit dem H1 Detektor am  $ep$ -Speicherring HERA genommen und entsprechen einer Luminosität von ungefähr  $18 \text{ pb}^{-1}$ . Der kinematische Bereich ist  $Q^2 < 1 \text{ GeV}^2$ ,  $40 < W_{\gamma p} < 300 \text{ GeV}$ . Die Datenselektion umfaßt den Bereich sehr kleiner Inelastizitäten  $z$ , in dem ein Signal beobachtet wurde. Effizienzen werden aus einem gemischten Monte Carlo Datensatz ermittelt. Wirkungsquerschnitte als Funktion von  $W_{\gamma p}$ ,  $z$  und  $p_{t,J/\psi}^2$  werden extrahiert und mit aktuellen Vorhersagen verglichen.

Es wurde festgestellt, daß die Daten Vorhersagen höherer Ordnung im Color Octet Modell mit kleinen Werten der Color Octet Matrixelemente bevorzugen. Vorhersagen führender Ordnung im Color Octet Modell zeigen einen Überschuß im Vergleich zu den Daten bei niedrigen als auch bei hohen Werten der Inelastizität  $z$ . Das Color Singlet Modell kann aufgrund der Daten noch nicht ausgeschlossen werden.

# Contents

<b>Abstract</b>	<b>1</b>
<b>Introduction</b>	<b>5</b>
<b>1 The Experiment</b>	<b>7</b>
1.1 The HERA Collider . . . . .	7
1.2 The H1 Detector . . . . .	8
1.2.1 Tracking Detectors . . . . .	8
1.2.2 Liquid Argon Calorimeter . . . . .	10
1.2.3 Spacal and Backward Drift Chamber . . . . .	10
1.2.4 Muon System . . . . .	11
1.2.5 Luminosity System . . . . .	12
1.2.6 Trigger System . . . . .	13
1.2.7 Software . . . . .	14
<b>2 Theoretical Considerations</b>	<b>17</b>
2.1 The Charmonium System . . . . .	17
2.2 Kinematics of $ep$ Scattering and $J/\psi$ Meson Production . . . . .	17
2.3 Models for $J/\psi$ Meson Production . . . . .	19
2.4 Production Processes at HERA . . . . .	21
2.4.1 Photon Gluon Fusion . . . . .	21
2.4.2 Resolved Photon Processes . . . . .	23
2.4.3 $B$ Meson Decay . . . . .	28
2.4.4 Fragmentation . . . . .	30
2.4.5 Diffraction . . . . .	31
2.4.6 Background Processes . . . . .	31
2.5 The Extraction of Color Octet Matrix Elements . . . . .	33
<b>3 Event Reconstruction</b>	<b>35</b>
3.1 Reconstruction of Kinematical Variables . . . . .	35
3.1.1 Reconstruction of $y$ . . . . .	36
3.1.2 Reconstruction of $x_\gamma$ . . . . .	38

---

3.2	Identification of the Scattered Electron . . . . .	39
3.3	The Forward Region of the H1 Detector . . . . .	41
3.3.1	Invariant Mass Resolution of the FTD and FMD . . . . .	42
3.3.2	Reconstruction Efficiency of the Forward Muon Detector . . . . .	42
<b>4</b>	<b>Data Selection and Monte Carlo Simulation</b>	<b>45</b>
4.1	Preselection . . . . .	46
4.1.1	Track Selection . . . . .	47
4.1.2	Muon Identification . . . . .	48
4.1.3	$J/\psi$ Candidates Selection . . . . .	49
4.2	Selection of Subtriggers . . . . .	50
4.2.1	Trigger Element Efficiencies . . . . .	52
4.2.2	Neural Network Trigger for Muons . . . . .	57
4.2.3	L4 Efficiency . . . . .	57
4.3	Prescaling . . . . .	58
4.4	Comparing Data and Monte Carlo . . . . .	58
4.5	Mixing of Monte Carlo Simulations . . . . .	68
<b>5</b>	<b>Results</b>	<b>73</b>
5.1	Determination of Cross Sections . . . . .	73
5.1.1	Signal Fitting and Background Subtraction . . . . .	73
5.1.2	Determination of $ep$ Cross Sections . . . . .	74
5.1.3	Determination of $\gamma p$ Cross Sections . . . . .	74
5.1.4	Statistical and Systematic Errors . . . . .	75
5.2	Measured Cross Sections . . . . .	76
5.3	Comparison to Previous Measurements . . . . .	85
<b>6</b>	<b>Conclusions and Outlook</b>	<b>89</b>
<b>A</b>	<b>Track Selection</b>	<b>91</b>
<b>B</b>	<b>Muon Selection</b>	<b>92</b>
<b>C</b>	<b>Definition of Subtriggers and Trigger Elements</b>	<b>93</b>
<b>D</b>	<b>Event Class 24</b>	<b>95</b>
<b>E</b>	<b>Monte Carlo Generators</b>	<b>97</b>
	<b>Bibliography</b>	<b>101</b>



# Introduction

The HERA collider (**H**adronen **E**lektronen **R**ing **A**nlage) and its experiments offer the unique possibility to study the collision of electrons and protons at very high energies. The center of mass energy,  $\sqrt{s} \simeq 300$  GeV, is equivalent to a fixed target experiment operating with an electron beam energy of approximately 50 TeV. An extensive physics program is accessible:

- Measurement of the structure functions of proton and pion
- Measurement of parton distributions of real and virtual photons
- Tests of perturbative QCD and electroweak theory
- Study of non perturbative QCD phenomena and diffractive scattering
- Searches for new particles and new interactions

The *standard model* provides a satisfactory framework in which all of these topics can be discussed. Over the last twenty years only very few small deviations from standard model predictions have been found, which were however not statistically significant.

The present analysis deals with  $J/\psi$  mesons in photoproduction events in  $ep$  collisions at HERA. In photoproduction the squared four momentum of the exchanged photon is small and the photon is quasi real. The  $J/\psi$  meson is a bound system of a  $c$  and a  $\bar{c}$  quark which owes its stability to the strong color force. Until 1992 all existing data on  $J/\psi$  meson production could be well described by the *color singlet model*. The data of  $J/\psi$  meson production in  $p\bar{p}$  collisions at the Tevatron however required the introduction of an extended model – the *color octet model*. If the model is applicable in  $p\bar{p}$  collisions there should be consequences for other experiments, such as H1 and ZEUS at HERA. The predictions for  $J/\psi$  meson production in  $ep$  collisions which have originally been derived from the color octet model show poor agreement with data. Additional effort from theorists and experimentalists is required to understand the observed discrepancy.

In this analysis the  $J/\psi$  mesons are identified via their decay into two muons. The branching ratio is only 6% but the identification of the muons in the muon system and the calorimeter allows a good discrimination of real  $J/\psi$  mesons and background processes. More than 2000  $J/\psi$  mesons from the data taking period 1997 corresponding to approximately  $18 \text{ pb}^{-1}$  integrated luminosity have been selected. Compared to previous analyses the kinematic range will be extended to higher photon proton center of mass energies and no cut on the inelasticity of the  $J/\psi$  mesons will be applied.  $J/\psi$  mesons which are produced in resolved photon events, where only a fraction of the photon's momentum interacts with the proton, are explicitly included. The extracted inclusive cross sections are discussed and compared to recent theoretical predictions.

The thesis is structured as follows:

HERA and the H1 detector are introduced in the first chapter including an overview of the trigger system. Chapter 2 describes the kinematics of  $J/\psi$  meson production in  $ep$  interactions and gives an overview of currently discussed theoretical models for  $J/\psi$  meson production at HERA. The typical detector signatures of each production process and issues which are relevant for the data selection are discussed here. Chapter 3 describes the reconstruction of kinematical variables and the selection of photoproduction events. Investigations whether the forward region of the detector can be included in inelastic  $J/\psi$  analyses are undertaken. The data selection is explained in Chapter 4. Emphasis is put on the determination of trigger efficiencies from Monte Carlo simulation. A mixed Monte Carlo data set is derived and Monte Carlo simulations will be compared to data. In chapter 5 inclusive photoproduction cross sections are extracted from data. The results are discussed and compared to recent theoretical predictions. The last chapter ends with conclusions and an outlook to future analysis.

# Chapter 1

## The Experiment

This chapter contains an overview of the HERA collider and the H1 detector including the trigger system. Focus is put on the detector components which are relevant for the present analysis.

### 1.1 The HERA Collider

The HERA collider at DESY, Hamburg was finished in 1990 after six years of construction. In a subterranean ring tunnel of 6 km circumference electrons (or positrons) and protons are accelerated and stored in two separate beam pipes. The counter rotating beams can collide at up to four interaction points with a center of mass energy  $\sqrt{s} \sim 300$  GeV. At present two multi purpose detectors (H1 and ZEUS) are operated in the northern and southern halls. Two further experiments, HERMES and HERA-B, make use of either the electron or the proton beam. Before injection in the HERA ring the particles go through linear (LINACs) and ring pre-accelerators (DESY II/III and PETRA), see figure 1.1. Refer to table 1.1 for further technical details.

During 1997 the ring was filled with positrons instead of electrons. With an enhanced vacuum system one will now return to electrons. Since August 1998 the machine has been running at a higher proton energy of  $\simeq 920$  GeV. In the year 2000 a major luminosity upgrade program will take place.

quantity	electrons	protons
beam energy [GeV]	27.5	820
number of bunches	174+15 pilot	174+6 pilot
average current [mA]	18.4	54.0
beam lifetime [h]	10	100
bunch length [cm]	1	11
bunch size $x \times y$ [ $\mu m$ ]	$280 \times 60$	$180 \times 60$

**Table 1.1:** HERA technical figures.

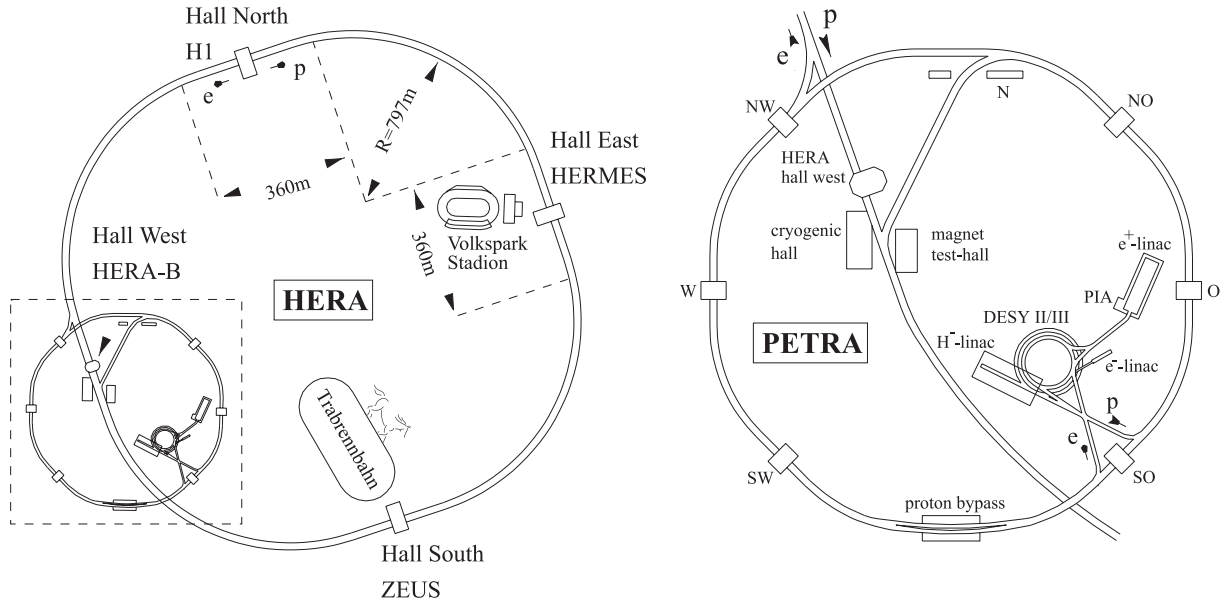


Figure 1.1: Layout of HERA and its pre-accelerators.

## 1.2 The H1 Detector

The H1 detector (see figure 1.2) follows the design principles of a modern multi purpose detector for collider experiments. Enhanced instrumentation has been installed in the forward region (the direction of the protons) to take account of the asymmetric beam energies and in the backward region to precisely measure the scattered electron. The detector has successively been improved and extended. In 1995 an improved backward calorimeter (Spacal) together with a drift chamber (BDC) and a spectrometer for measuring the forward scattered proton (FPS) was installed. Especially the newly installed hadronic part of the Spacal calorimeter is essential for this analysis. In 1997 two silicon vertex detectors (CST, BST) were fully available for physics analysis. In 1998 a new calorimeter and tracking device for the detection of the electron under very small angles (VLQ) has been added. In the following sections only the detector components which are relevant for this analysis will be described. For further details refer to [1, 2].

### 1.2.1 Tracking Detectors

With the help of the central tracking detector (**CTD**) the charges and three momenta of charged particles in the central detector region can be measured. The central jet chambers (**CJC 1,2**) cover the polar angle range  $10^\circ < \theta < 165^\circ$ . The forward tracking detector (**FTD**) covers  $5^\circ < \theta < 30^\circ$ . The FTD consists of three supermodules with radial chambers, planar chamber, MWPC (Multi Wire Proportional Chamber) and transition radiation detector in each. Particles in the polar angle region  $10^\circ \lesssim \theta \lesssim 30^\circ$  will traverse both CTD and FTD. The tracking detectors are shown in figure 1.3. The proportional chambers **CIP** and **COP** (Central Inner/Outer Proportional chambers) are used for triggering purposes only (see 1.2.6). **CIZ** and **COZ** (inner/outer  $z$  chamber) with their wires strung perpendicular to the beam pipe have been installed to improve the  $z$  resolution.



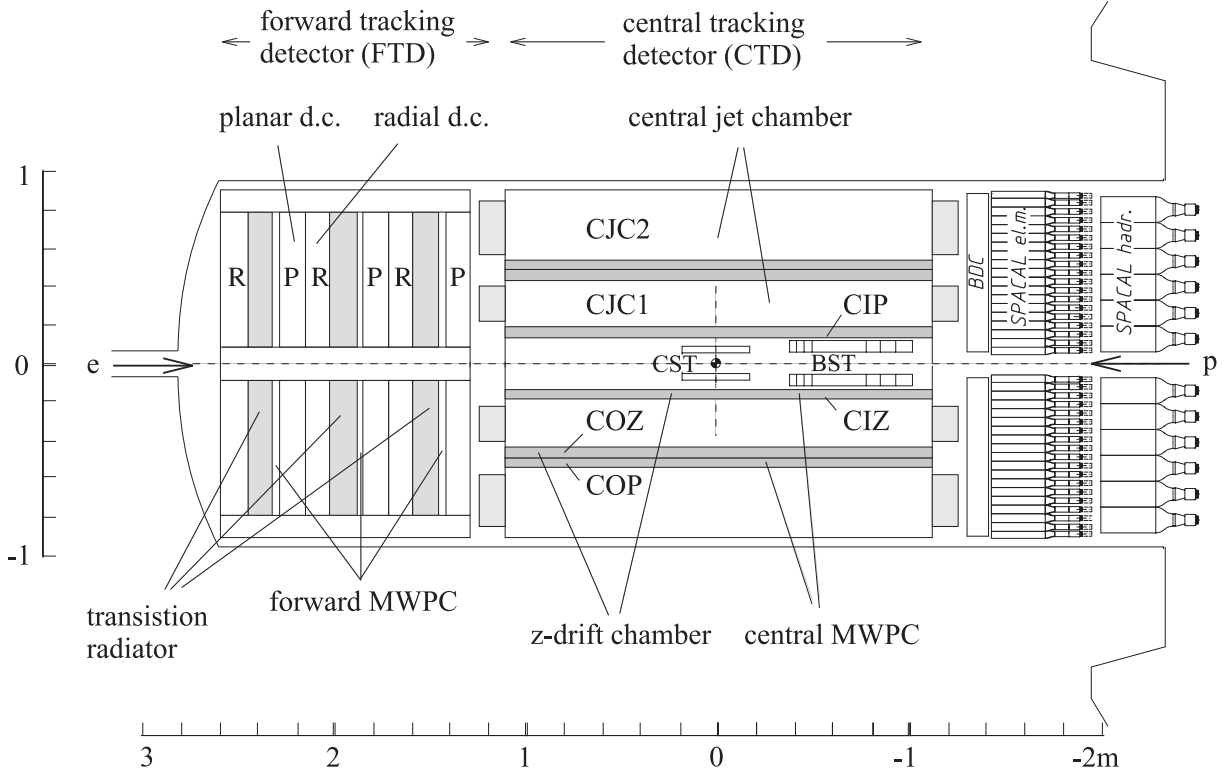


Figure 1.3: Side view of the tracking chambers.

### 1.2.2 Liquid Argon Calorimeter

The liquid argon (**LAr**) calorimeter can be seen in figure 1.2. The purpose of the liquid argon sampling calorimeter is to identify neutral and charged particles and to measure their energies. It covers an angular range of  $4^\circ < \theta < 154^\circ$  and consists of 65000 cells. It is divided into an inner electromagnetic part, using lead as absorber, and an outer hadronic part using stainless steel as absorber. The depth of the electromagnetic section varies with the polar angle between 20 and 30 radiation lengths  $X_0$ . The total depth is between 4.5 and 8 nuclear interaction lengths,  $\lambda$ . In both cases liquid argon is used as active material. Due to the non compensating nature (the response of hadrons being typically 30% less than that for electrons) the calorimeter has been calibrated at two different energy scales. The energy resolution is  $\sigma_E/E \simeq 12\%/\sqrt{E[\text{GeV}]}$  for electrons and  $\sigma_E/E \simeq 50\%/\sqrt{E[\text{GeV}]}$  for pions.

### 1.2.3 Spacal and Backward Drift Chamber

The backward drift chamber (**BDC**) is mounted in front of the backward calorimeter Spacal (see figures 1.2, 1.3, 1.7). The purpose of the BDC is to exactly measure the scattered electron's polar angle and to improve the particle identification (namely to distinguish between photons and electrons — latter particles will be registered in the BDC).

The primary purpose of the lead/scintillating fiber calorimeter Spacal is to precisely measure the cluster shape, position and energy of the scattered electron. Furthermore it comprises a hadronic part. In the present analysis the Spacal will also be used to measure the so called

photon remnant (see Chapter 2). Note that the innermost electromagnetic cells surrounding the beam pipe have irregular shapes (see figure 1.7). See table 1.2 for some more performance figures.

quantity	size
no. of cells	1192 em. + 143 had.
cell size [cm <sup>2</sup> ]	4 × 4 em.; 12 × 12 had.
energy resolution	$\sigma_E/E = 7.5\%/\sqrt{E[\text{GeV}]}$
time resolution	1 ns
polar angle range	$158^\circ < \theta < 178^\circ$

**Table 1.2:** Spacial performance figures.

### 1.2.4 Muon System

The outermost part of the H1 detector next to the super-conducting coil is the **instrumented iron**. It serves as a magnetic return yoke and as a muon detector. Primarily muons with  $p \gtrsim 1.2$  GeV will be detected in the instrumented iron. To a smaller extent hadrons may reach the muon detectors as well, resulting in their misidentification as muons. The instrumented iron has been equipped with limited streamer tubes (eight single and one double layer in between 10 iron plates plus 3 layers inside and 3 layers outside the iron yoke). It comprises 64 modules in total and is divided into a forward and a backward barrel part ( $35^\circ < \theta < 130^\circ$ ) and the forward and backward endcaps ( $5^\circ < \theta < 35^\circ$ ,  $130^\circ < \theta < 175^\circ$ ). The endcaps are further divided into an inner and an outer part (see figure 1.4). With the help of 103700 wires, 28700 strips (running perpendicular to the wires) and pad electrodes the position and direction of particles traversing the instrumented iron can be reconstructed. In addition the pad electrodes serve as a calorimeter. The so called **tail catcher** can detect energy leakage from the LAr and Spacial calorimeters.

The muon system is completed by the forward muon detector (**FMD**) covering the polar angle range  $3^\circ \lesssim \theta \lesssim 17^\circ$ . The FMD consists of six double layers of drift chambers and a toroidal magnet and provides identification and momentum measurement for muons with  $p \gtrsim 5$  GeV.

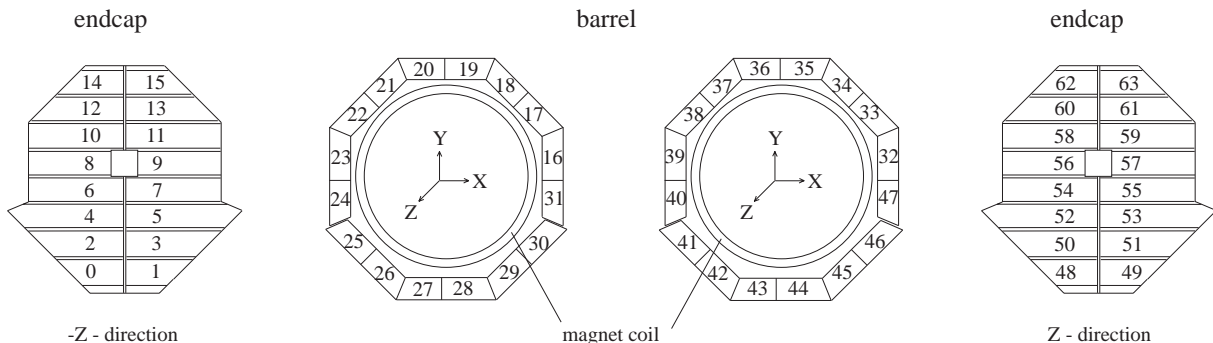


**Figure 1.4:** The 64 modules of the instrumented iron. The instrumented iron detects muons and is used as a return yoke for the magnetic field from the superconducting coil. Modules 6...11 (54...59) belong to the inner backward (forward) endcap.

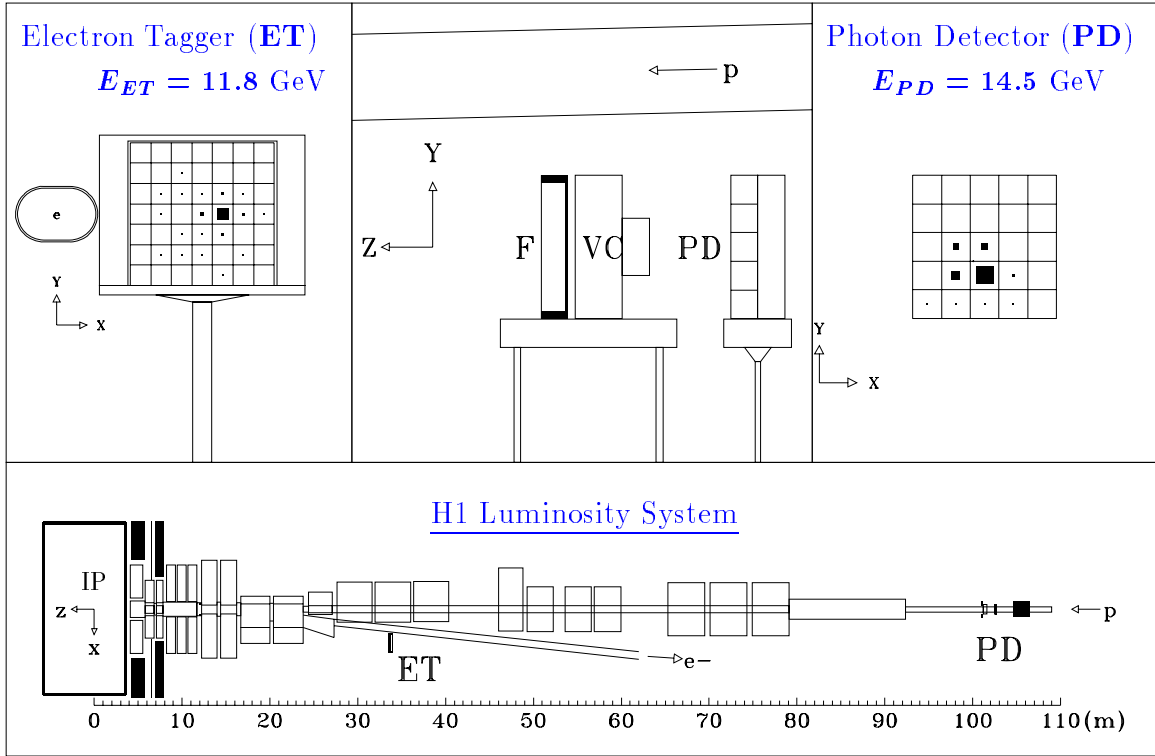


**Figure 1.5:** A Bethe-Heitler bremsstrahlung event measured with the luminosity system. The electron deposits  $E_e = 11.8$  GeV in the electron tagger E33 (upper left), while the photon energy  $E_\gamma = 14.5$  GeV is measured in the photon detector (PD, top right). The lower part shows a top view of the luminosity system. The middle part shows details of the photon detection system. F is a lead absorber and VC a water Cherenkov veto counter.

### 1.2.5 Luminosity System

The luminosity system, shown in figure 1.5, consists of the photon detector (PD) at  $z = -110$  m, and the electron taggers at  $z = -33$  m (ET33) and  $z = -44$  m (ET44). These are crystal Cherenkov counters. A further electron tagger has been installed but was not fully functioning in 1997. The major tasks of the luminosity system are:

1. Online and offline luminosity measurement by detecting the photon and the scattered electron from the well known Bethe-Heitler-Process ( $ep \rightarrow ep\gamma$ ). In the offline reconstruction, which uses only the photon measurement, a precision of better than 2% can be achieved.
2. Energy measurement for electrons scattered at very small angles, tagging of photoproduction events with  $Q^2 \lesssim 0.01$  GeV<sup>2</sup>.

The present analysis uses ET44 to tag the electrons in photoproduction events. ET33 will only be used to cross check the reconstruction of the kinematic variable  $y$ . Further issues related to the luminosity system and the associated triggers will be discussed in section 4.2.1.

### 1.2.6 Trigger System

High luminosities at HERA are achieved by multi bunch operation with 174 bunches per beam resulting in an extremely high interaction rate. Bunches cross each other every 96 ns. The expected rate of interesting physics events is significantly smaller and can be compared to the rate of background events. Background events are mainly caused by beam gas and beam wall interactions and cosmic radiation. It is the task of a trigger system with three active levels to distinguish physics events from background:

- The first trigger level, L1, is a pipelined system which buffers drift times in the tracking chambers, detector read out times and cable delays. Each detector component will indicate a possibly interesting event by activating a *trigger element*. Logical combinations from 192 trigger elements of different detector components form 128 so called *subtriggers*. Events will be discarded if all subtriggers decide negatively. To decrease the rate of some L1 subtriggers a prescaling technique is applied. Subtriggers which are prescaled by a variable factor  $d$  will accept only every  $d$ 'th event. The trigger decision before prescaling is called *raw* and afterwards *actual*. L1 reduces the initial event rate of  $\sim 100$  kHz by a factor of  $\sim 100$ .
- The detector response can be evaluated in more detail on level 2. L2 uses either topological correlations of subdetector signals (L2TT) or the result of neural nets (L2NN) to verify the decision of selected high rate L1 subtriggers. L2 typically reduces the event rate by another factor of 20 to  $\sim 50$  Hz.
- L4 is the last trigger level being operated online. It consists of  $\sim 30$  PowerPC processors. A preliminary event reconstruction using the full detector information is performed. The aim is again to verify L1 subtriggers. L4 involves high level analysis cuts (e.g. applying a cosmic rejection). The event rate will be reduced by a factor of  $\sim 5$  to  $\sim 10$  Hz.

Events passing all trigger levels will be written to tape in a proprietary data format (POT, production output tapes). After a full reconstruction by a dedicated computing farm (L5) the events are finally assigned to several physics classes. Class 24 (see appendix D) containing events with two muon candidates will be relevant for the present analysis. Data analyses are then based on a subset of the POT data, the so called DST format (data summary tape).

In the following paragraphs the principle of operation of the most important L1 trigger elements will be sketched, as far as they are relevant for the present analysis.

#### Muon System Trigger

In the instrumented iron wire signals of five selected streamer tube layers are used for triggering purposes (layers 3, 4, 5, 8 and 12 where the innermost layer is layer 0). Coincidences of two or more trigger layers per module form several trigger elements (see table C.2). In the barrel region at least two of the four innermost trigger layers are required for a trigger element to fire. In the backward endcap and forward outer endcap three and in the forward inner endcap four out of five trigger layers are required.

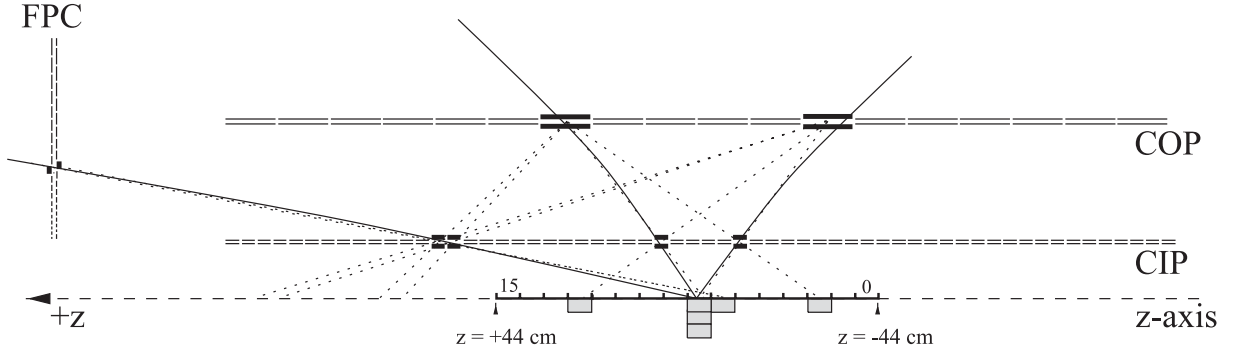


**Figure 1.6:** Principle of operation of the z-Vertex Trigger. The side view shows an event with three tracks originating from genuine particles (solid lines). The dotted lines represent all possible combinations of CIP, COP and FPC hits. The z-Vertex histogram shows a maximum at the  $z$  position of the primary event vertex.

### DCRPh Trigger

The aim of the DCRPh trigger is to find tracks in the central drift chambers. The digitized hits from 10 selected CJC wire layers (out of 56) are compared with 10,000 predefined masks. Trigger elements for low/high  $p_t$  tracks, negative/positive charged tracks, low and high track multiplicity have been defined (see table C.3).

### z-Vertex Trigger

The z-Vertex histogram performs a fast determination of the  $z$  position of the primary event vertex. All combinations of CIP and COP hits (and hits from the first forward proportional chamber) are connected to form rays. Intersections with the  $z$  axis are counted in the so called z-Vertex histogram. This can best be understood when looking at figure 1.6. A variety of trigger elements are derived from the z-Vertex histogram (see table C.4).

### Spacal IET Trigger

The Spacal IET trigger (inclusive electron trigger) is designed to detect clusters in the electromagnetic part of the calorimeter within the short decision time ( $2.3 \mu\text{s}$ ) of trigger level L1. The electromagnetic Spacal has been divided in overlapping *sliding windows* of  $4 \times 4$  cells each. The summed energy content of each sliding window can then be compared to predefined energy thresholds. The principle is illustrated in figure 1.7. The relevant trigger elements and energy thresholds are listed in table C.4.

## 1.2.7 Software

Two major software packages employed at H1 are the detector simulation (H1SIM, [3]) and the event reconstruction (H1REC). Input for H1SIM is the data generated by Monte Carlo simulation software packages, i.e. the four vectors of particles with lifetimes typically longer than 8 ns. The simulation is performed in three steps:

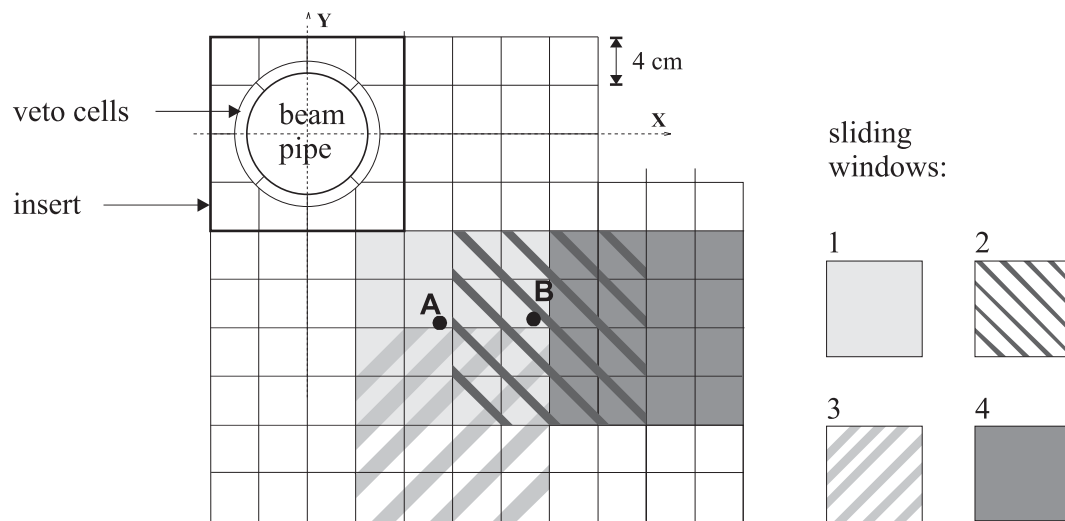


**Figure 1.7:** Principle of operation of the Spacal IET trigger. The total energy of a cluster around point A (B) will be collected in sliding window 1 (2). The trigger fires if at least one sliding window exceeds a predefined energy threshold.

1. The path of each particle through the detector material is simulated. This is done using the GEANT software package and includes the movement in the magnetic field, energy loss, secondary particle generation and shower development.
2. Simulation of each subdetector's low level response.
3. Simulation of the trigger response.

The output of H1SIM is then fed into H1REC, the same software package which is used for the reconstruction of real data events. Main steps in the event reconstruction are the track reconstruction in tracking devices, linking of inner and outer (muon system) tracks and cluster finding in the calorimeters.



## Chapter 2

# Theoretical Considerations

In this chapter the basic properties of  $J/\psi$  mesons and the kinematics of their production in  $ep$  interactions will be described. An overview of the most important models for the production process will be given.

### 2.1 The Charmonium System

The  $J/\psi$  meson is a bound  $c\bar{c}$  state with the quantum numbers  $J^{PC} = 1^{--}$  and mass 3.097 GeV. Its stability can be explained by simple potential models analogous to the hydrogen atom except that the constituents are held together by gluons of the strong interaction rather than photons of the electromagnetic interaction. Similar to the hydrogen atom many radiative transitions between an entire family of bound charmonium states are observed (see figure 2.1). A particular property of the  $J/\psi$  meson is its small decay width  $\Gamma \sim 87$  keV. The prominent decay channel into two  $D$  mesons is forbidden because of energy conservation and decays which involve one or two gluons are forbidden due to color and  $C$ -parity conservation.

The  $J/\psi$  meson was discovered in 1974 by two groups almost simultaneously. A sudden rise in the cross section of  $e^+e^-$  collisions at the SPEAR machine in Stanford (SLAC) was observed by Augustin et al. [4]. An enhancement in the  $e^+e^-$  invariant mass spectrum in  $p\text{Be} \rightarrow e^+e^- + X$  reactions at the Brookhaven National Laboratory was reported by Aubert et al. [5]. The discovery was awarded with the Nobel prize in physics for Samuel C.C. Ting from BNL and Burton Richter from SLAC.

### 2.2 Kinematics of $ep$ Scattering and $J/\psi$ Meson Production

The HERA coordinate system is shown in figure 2.2 a). The  $z$ -axis points in the *forward* direction of the protons. A generic Feynman diagram for  $ep$  interactions is shown in figure 2.2 b). The interaction is dominantly mediated by a photon rather than a  $W^\pm$  or  $Z^0$ .  $k$  and  $p$  are the four vectors of the initial electron and proton. The squared center of mass energy of the collision is (the masses are neglected here and in the following)

$$s = (k + p)^2 \simeq 4E_e E_p = (300 \text{ GeV})^2, \quad (2.1)$$

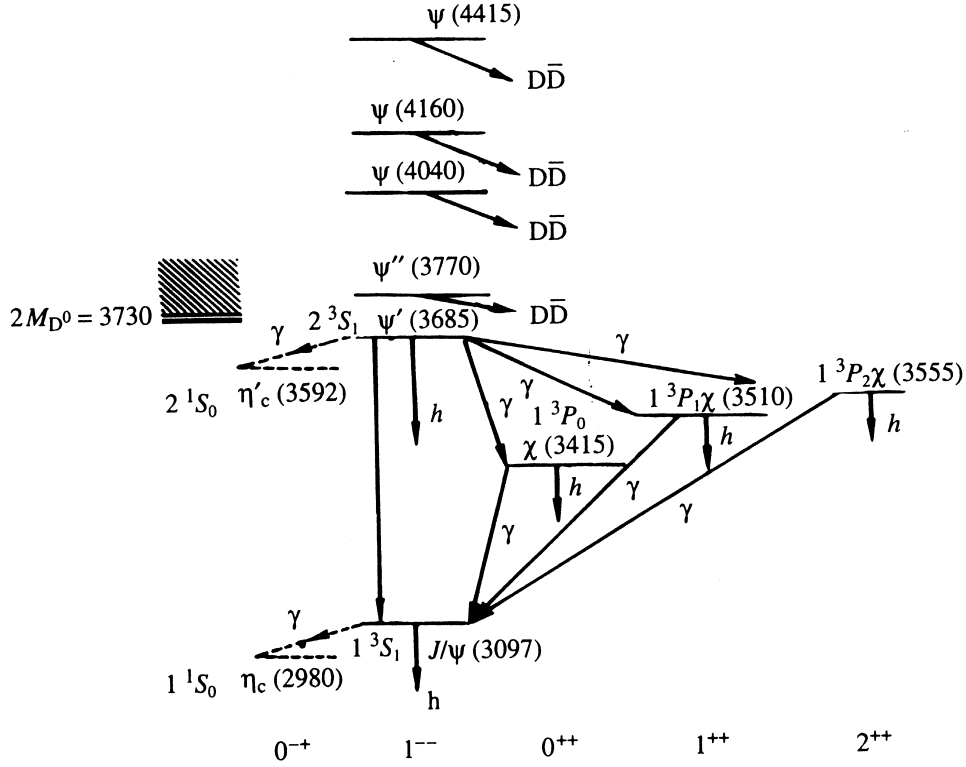


**Figure 2.1:** Level diagram of the system of charmonium bound states (from [6]).

where  $E_e = 27.5$  GeV and  $E_p = 820$  GeV are the energies of the incident electron and proton. Let  $k'$  be the four vector of the scattered electron. Then the four momentum of the exchanged photon is

$$q = k - k'. \quad (2.2)$$

The *virtuality* of the photon is

$$Q^2 = -q^2 \simeq 4E_e E'_e \sin^2(\theta_e/2), \quad (2.3)$$

where  $E'_e$  is the energy of the scattered electron. In the case of low virtualities ( $Q^2 \lesssim 1$  GeV<sup>2</sup>, photoproduction) the electron will be scattered at small polar angles  $\theta_e$  and escapes through the beam pipe. In the case of high virtualities ( $Q^2 \gtrsim 1$  GeV<sup>2</sup>, deep inelastic scattering, DIS) the electron will be scattered at larger polar angles and is detected in the backward detector region. The Lorentz invariant scaling variable  $y$  is defined by

$$y = \frac{q \cdot p}{k \cdot p} \simeq \frac{E_e - E'_e}{E_e}. \quad (2.4)$$

In the laboratory frame it is the fractional energy loss of the scattered electron (neglecting the masses and assuming that  $\vec{q} \parallel \vec{p}$ ). The squared center of mass energy of the photon proton system is

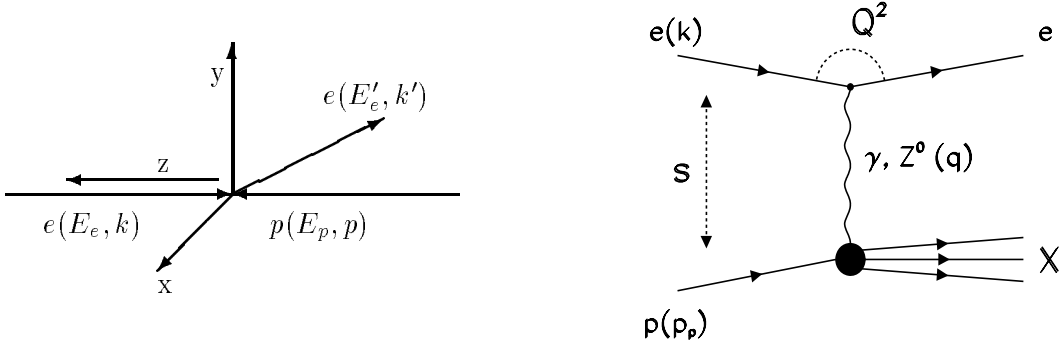


**Figure 2.2:** a) The HERA coordinate system. The  $z$ -axis points in the direction of the protons. b) A generic Feynman diagram for  $ep$ -scattering.  $X$  designates any hadronic final state. The variables are explained in the text.

$$W_{\gamma p}^2 = (p + q)^2 \simeq y \cdot s. \quad (2.5)$$

The last part is valid in photoproduction. An important kinematic variable in  $J/\psi$  meson photoproduction is the Lorentz invariant *inelasticity*  $z$ :

$$z = \frac{p_{J/\psi} \cdot p}{q \cdot p}, \quad (2.6)$$

where  $p_{J/\psi}$  is the  $J/\psi$  meson's four momentum. In the proton rest frame the inelasticity is the fraction of the photon's energy which is transferred to the  $J/\psi$  meson. Events with  $z = 1$  are called *elastic* or *quasielastic* for  $z \gtrsim 0.9$  compared to *inelastic* events at low values of  $z$ .

## 2.3 Models for $J/\psi$ Meson Production

The non diffractive production (see section 2.4.5) of a  $J/\psi$  meson can be described by a two stage process. In the first step, which is calculable by the means of perturbative QCD, a free quark-antiquark pair is produced. The second step is the formation of a bound  $J/\psi$  state. Before data on  $J/\psi$  production from  $p\bar{p}$  collisions at the Tevatron became available a satisfactory description of  $J/\psi$  meson production was given by the *color singlet model* (CSM). In the CSM it is assumed that only  $c\bar{c}$  pairs which are produced in a color singlet state contribute significantly to the cross section. Within the CSM the amplitude for  $J/\psi$  production is given by

$$d\sigma(J/\psi + X) = d\hat{\sigma}(c\bar{c}(\underline{1}, {}^3S_1) + X) \cdot |R_{J/\psi}(0)|^2. \quad (2.7)$$

The spectroscopic notation  ${}^{2S+1}L_J$  is used for the angular momentum state of the  $c\bar{c}$  pair, where  $S$ ,  $L$ , and  $J$  are the quantum numbers associated with the total spin, the orbital angular momentum, and the total angular momentum, respectively.  $\underline{1}$  designates a color singlet state.  $R_{J/\psi}(0)$  is the value of the meson's radial wave function at the origin. The latter value can be determined from the leptonic decay width of the  $J/\psi$  meson:

$$\Gamma(J/\psi \rightarrow l^+l^-) \simeq \frac{4\alpha^2}{9m_c^2} \cdot |R_{J/\psi}(0)|^2. \quad (2.8)$$

The CSM has large predictive power but it suffers from various uncertainties. No theorem guarantees the validity of the above factorization formula and it is not clear whether higher order radiative corrections would respect this factorization [9]. Relativistic effects which may be of importance in the  $c\bar{c}$  system [7] are neglected in the CSM. Furthermore the assumption that a color octet state cannot lead to a bound  $J/\psi$  state must be wrong at some level since a color octet  $c\bar{c}$  pair can make a non perturbative transition to a color singlet state by the emission of a soft gluon. For  $P$  wave states it can be shown that the CSM cross section is infrared divergent. Predictions in the CSM have a large normalization uncertainty due to the choice of the proton parton density function, the charm quark mass and the value of  $\alpha_s$ .

A more rigorous approach is the *color octet model* (COM). In the COM  $c\bar{c}$  pairs can be produced in color singlet as well as color octet states. According to QCD only the final state  $J/\psi$  meson must be in a color singlet state. A general factorization formalism based on NRQCD (non relativistic QCD) was proposed by Bodwin, Braaten and Lepage [8]. NRQCD is an effective field theory which treats the heavy quarks in a non relativistic manner by a Schrödinger field theory with 2-component spinor fields. Gluons and light quarks are described by the ordinary relativistic QCD Lagrangian. NRQCD organizes calculations of heavy quarkonium observables into an expansion in powers of  $v$ , where  $v$  is the relative velocity of the quarks in the heavy quarkonium. The basic result is a factorization formula for the inclusive cross section for producing a quarkonium state  $H$  which holds in all orders of  $\alpha_s$ :

$$d\sigma(H + X) = \sum_n d\hat{\sigma}(c\bar{c}(n) + X) \langle \mathcal{O}_n^H \rangle. \quad (2.9)$$

$d\hat{\sigma}$  is the inclusive cross section for producing a  $c\bar{c}$  pair in a color and angular-momentum state labelled by  $n$  and having vanishing relative momentum.  $\langle \mathcal{O}_n^H \rangle$  is proportional to the probability for a pointlike  $c\bar{c}$  pair in the state  $n$  to form the bound state  $H$ . The factorization has been defined in such a way that the first factor can be calculated by a perturbation expansion in  $\alpha_s$ . The color singlet matrix elements  $\langle \mathcal{O}_{[\underline{1}, 2S+1} L_J] \rangle$  can again be related to the radial wave functions. For example for a color singlet  $c\bar{c}$  pair with  $n = [\underline{1}, {}^3S_1]$ :

$$\langle \mathcal{O}^{J/\psi}[\underline{1}, {}^3S_1] \rangle = \frac{9}{2\pi} \cdot |R_{J/\psi}(0)|^2 \quad (2.10)$$

In the most general case equation 2.9 involves infinitely many non perturbative factors. However, in the framework of NRQCD each matrix element scales with a defined power of  $v$ . To be more exact: The scaling of  $\langle \mathcal{O}^H[\underline{n}, 2S+1 L_J] \rangle$  is given by the number of electric dipole and magnetic dipole transitions that are required to go from the dominant fock state of the meson  $H$  to a state of the form  $|c\bar{c}[\underline{n}, 2S+1 L_J] + \text{gluons}\rangle$ . The matrix element scales as  $v^{3+2L}$ , multiplied by  $v^2$  for each electric dipole transition and  $v^4$  for each magnetic transition.

The relative importance of each term in equation 2.9 is given by the order in  $\alpha_s$  and  $v$ . The color octet matrix elements  $\langle \mathcal{O}_n^H \rangle$  cannot be calculated perturbatively and must be determined from measurements or numerically from lattice QCD. Results from the lattice are not yet available. Experimental data is available from  $p\bar{p}$  collisions at the Tevatron. The matrix elements which are extracted from the Tevatron data can be used in predictions for the  $J/\psi$  meson production cross

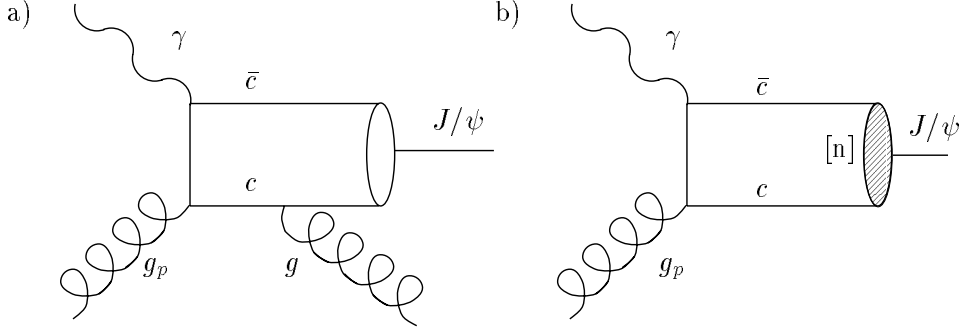


**Figure 2.3:** Feynman diagrams in leading order in  $\alpha_s$  for photon gluon fusion in a) the color singlet model and b) the color octet model.  $[n]$  labels the color state of the  $c\bar{c}$  pair.

section at HERA (see section 2.5). A more detailed review of models for quarkonia production can be found in [9] and [10].

## 2.4 Production Processes at HERA

The following subsections are dedicated to the details of the production processes at HERA. The typical kinematic distributions and detector signatures are discussed. For each process (except for fragmentation) the Monte Carlo prediction as a function of  $z$ ,  $W_{\gamma p}$  and  $p_{t,J/\psi}$  will be shown:

- The number of generated events without further cuts.
- The remaining number of events after requiring that both decay muons can be detected in the central detector region ( $20^\circ < \theta_\mu < 160^\circ$  and  $p_\mu > 800$  MeV).
- The remaining number of events if the upper polar angle cut is decreased to  $\theta_\mu < 140^\circ$ . This cut is motivated by the fact that it eliminates background events at low  $z$  very effectively (see chapter 4).
- The number of events when requiring that one muon can be detected in the Forward Muon Detector ( $6^\circ < \theta_\mu < 17^\circ$  and  $p_\mu > 6$  GeV, the other muon must be detected in the central detector region, see above).

### 2.4.1 Photon Gluon Fusion

The Feynman diagram for photon gluon fusion in leading order in  $\alpha_s$  is shown in figure 2.3 for a) the color singlet model and b) the color octet model. A gluon from the proton and the photon from the electron fuse via a virtual  $c$  quark line. This process is sometimes referred to as *direct* production. In the color singlet model the emission of a hard gluon is required to achieve a color singlet final state. In the color octet model the transition to a color singlet final state is accomplished by radiation of soft gluons. At HERA, photon gluon fusion is the dominant process in the kinematic range  $0.3 < z < 0.9$ . Previous HERA analyses [11, 12] showed that  $J/\psi$  meson production in this restricted kinematic range is compatible with the predictions of the color singlet model within experimental and theoretical uncertainties.

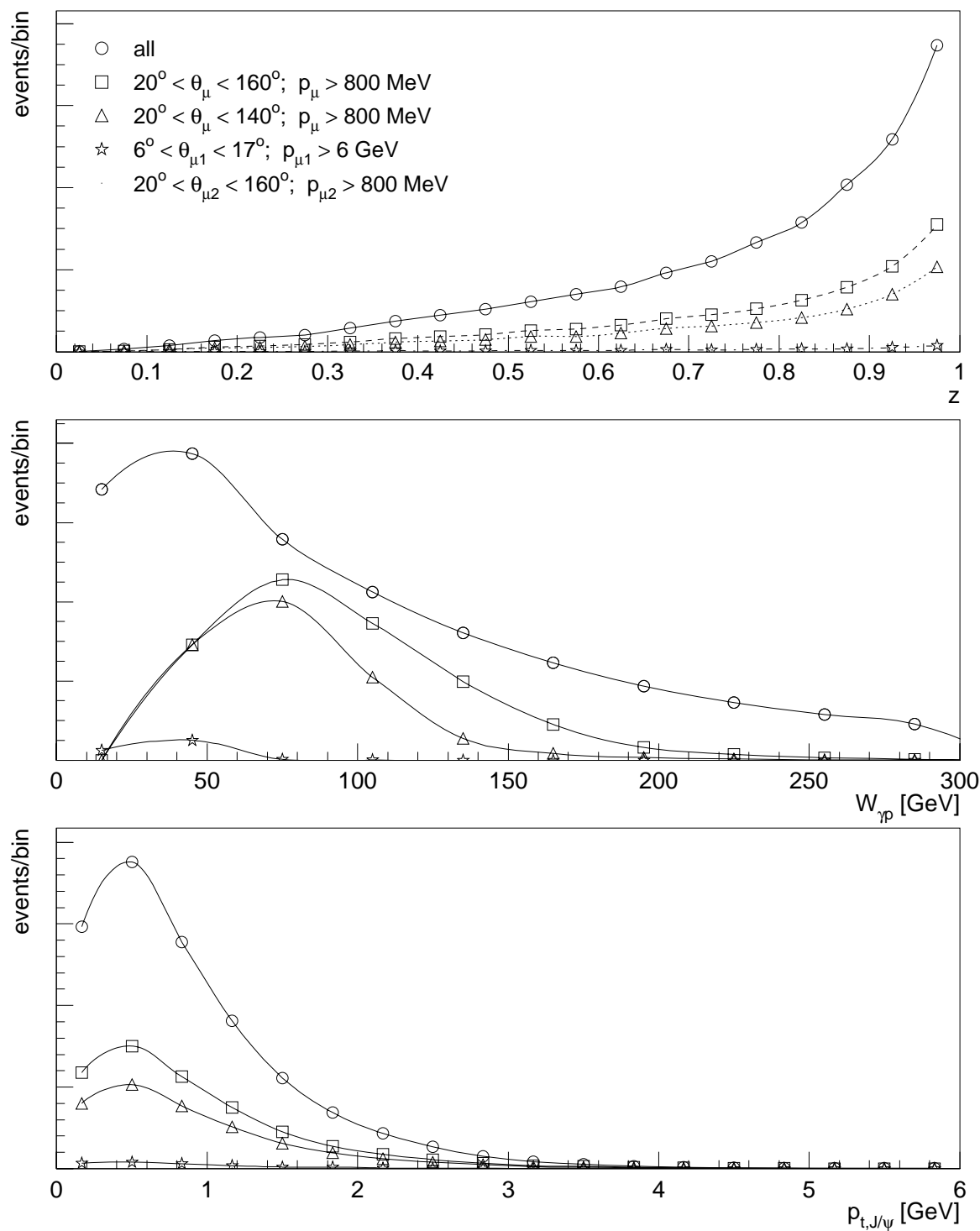


**Figure 2.4:** Number of **photon gluon fusion** events generated with EPJPSI (CSM) as a function of  $z$ ,  $W_{\gamma p}$  and  $p_{t, J/\psi}$  (circles). The squares show the remaining events after requiring that the two decay muons can be detected in the central detector region. The triangles show the number of events remaining if the upper polar angle cut for the decay muons is decreased by  $20^\circ$  to  $140^\circ$ . The stars show the number of events with one muon being detected in the forward muon detector.

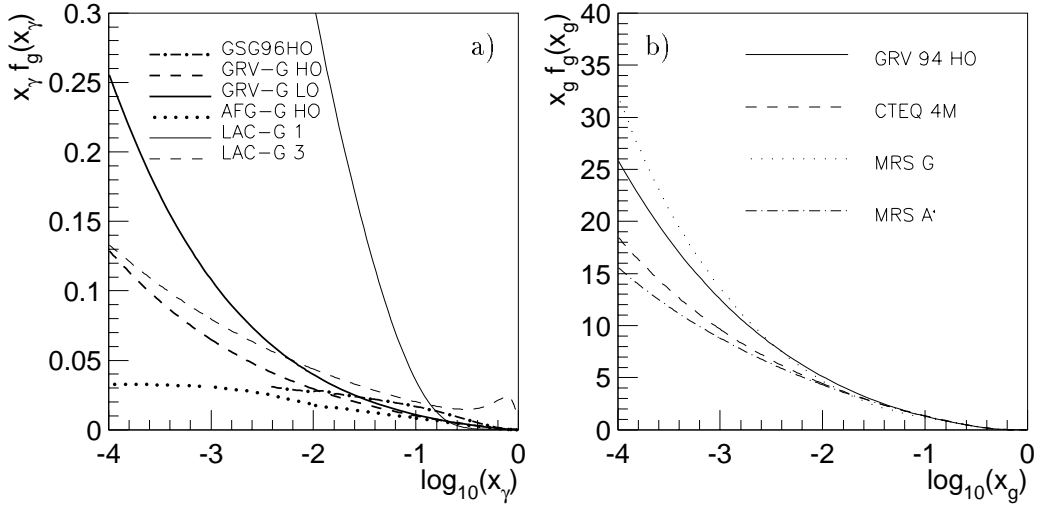


**Figure 2.5:** Recent parameterizations of the gluon density in a) the photon and b) the proton.  $x_\gamma$  is the momentum fraction of the parton inside the photon.  $x_g$  is the momentum fraction of the parton inside the proton.

Photon gluon fusion events in the color singlet model can be simulated with the Monte Carlo generator EPJPSI<sup>1</sup> [13]. Figure 2.4 shows the number of generated events as a function of  $z$ ,  $W_{\gamma p}$  and  $p_{t,J/\psi}$ . The acceptance as a function of  $W_{\gamma p}$  depends strongly on the geometrical cuts for the decay muons. Requiring two central muons the maximum is at  $\sim 80$  GeV. With one muon detected in the FMD the maximum is at  $\sim 50$  GeV. Decreasing the upper polar angle cut is not desirable for photon gluon fusion processes.

### 2.4.2 Resolved Photon Processes

A quasi-real photon ( $Q^2 \rightarrow 0$  GeV<sup>2</sup>) can behave like a hadron and interact via its partonic contents with the proton. The longitudinal momentum distributions of the hadronic contents of the photon (i.e. gluons, light and heavy sea quarks) are described by photon parton density functions (PDF). Recent parameterizations of photon and proton PDFs are shown in figure 2.5.  $ep$  cross sections can be written as a sum of direct and resolved contributions:

$$\sigma_{ep} = \sigma_{ep}[\text{direct}] + \sigma_{ep}[\text{resolved}]. \quad (2.11)$$

The separation of these two contributions must be handled with care since some terms of the direct processes may already be included in the photon PDF [14].

The Feynman diagram for  $J/\psi$  meson production in resolved photon processes in leading order in  $\alpha_s$  is shown in figure 2.6 for the color singlet and the color octet model. A parton from the photon and a parton from the proton interact via a virtual quark line. The process depends on the momentum distribution of the partons inside the photon as well as the proton. According to recent photon and proton PDF parameterizations the dominant process is the interaction of two gluons. Resolved photon events have a second hadronic system besides the proton remnant: the so called *photon remnant*. Long range strong color forces produce hadrons in the electron

<sup>1</sup>The default settings used for Monte Carlo generation with EPJPSI are listed in appendix E

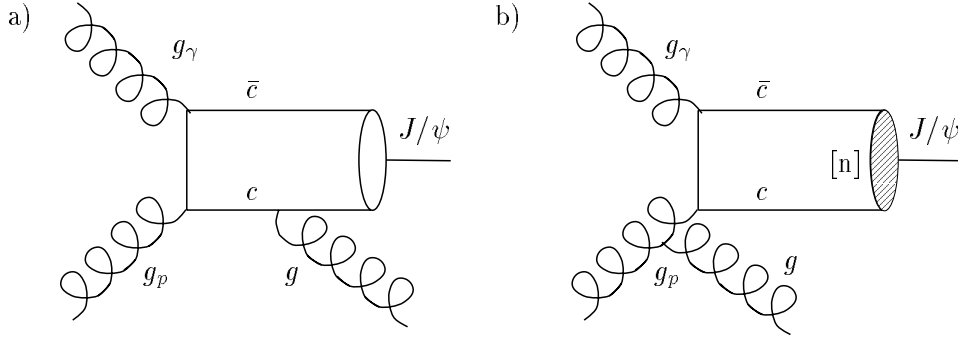


**Figure 2.6:** Feynman diagrams in leading order in  $\alpha_s$  for resolved photon processes. The graph for color singlet production and  $^3S_1$  octet states is shown in a). The graph for color octet  $^1S_0$  and  $^3P_J$  states is shown in b).  $[n]$  labels the color state of the  $c\bar{c}$  pair.

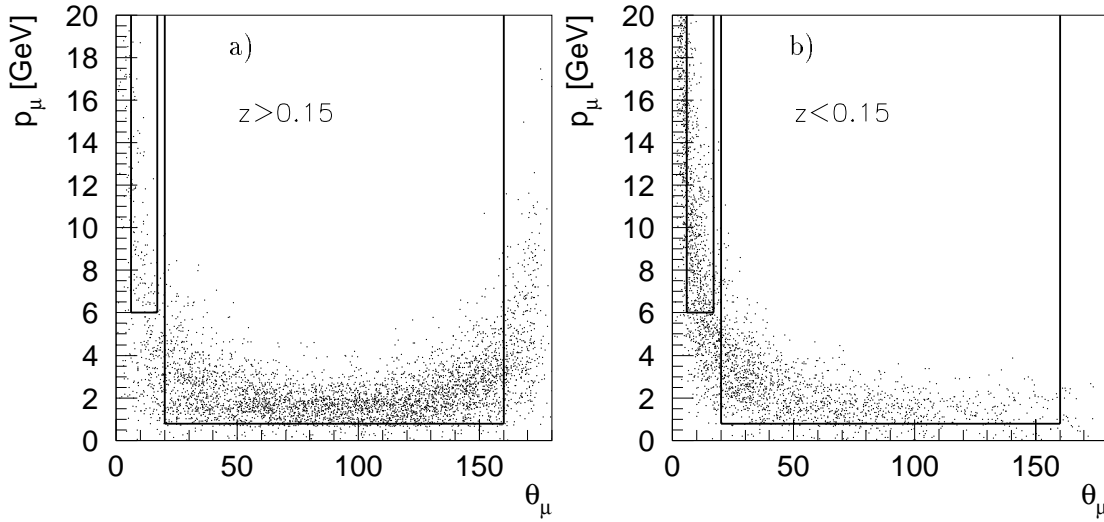


**Figure 2.7:** Polar angle and momentum distribution of the decay leptons in resolved photon processes generated with EPJPSI: a) for  $z > 0.15$  and b) for  $z < 0.15$ . The central detector acceptance region and the acceptance region of the forward muon detector are shown with lines.

direction from the remnants of the photon. Resolved photon processes are found at small values of  $z$  due to the fact that only a small fraction  $x_\gamma$  of the photon's four momentum is utilized in the production of the  $J/\psi$  meson. The decay leptons from  $J/\psi$  mesons at small values of  $z$  will dominantly be found at small polar angles. Table 2.1 shows the percentage of detectable  $J/\psi$  mesons from resolved processes when applying different polar angle cuts on the decay leptons which are motivated by the detector acceptance regions. The values for  $J/\psi$  mesons from photon gluon fusion are given for comparison. The muons' polar angle and momentum distribution is shown graphically in figure 2.7, where the central detector acceptance region and the FMD acceptance region are shown with lines.

In resolved processes one expects significant contributions from  $c\bar{c}$  pairs produced in color octet states [15]. The exact size depends strongly on the value of the color octet matrix elements.

Furthermore in resolved processes  $\chi_c$  mesons can be produced, which is forbidden in the direct production mechanism in the color singlet model at leading order.  $\chi_c$  mesons decay radiatively into  $J/\psi$  mesons with the branching ratios  $B(\chi_{c0} \rightarrow J/\psi\gamma) = 6.6 \cdot 10^{-3}$ ,  $B(\chi_{c1} \rightarrow J/\psi\gamma) =$

cuts on decay muons	resolved events	photon gluon fusion events
none	100 % (59.9%→100%)	100% (%31.0→100%)
both muons:		
$20^\circ < \theta_\mu < 160^\circ$	33.7% (39.8%)	41.6% (44.6%)
$20^\circ < \theta_\mu < 140^\circ$	28.0% (33.3%)	28.2% (30.7%)
$6^\circ < \theta_\mu < 17^\circ$	4.4% (4.8%)	2.9% (3.2%)
$20^\circ < \theta_\mu < 160^\circ, p_\mu > 800 \text{ MeV}$	31.7% (36.6%)	40.7% (42.0%)
$20^\circ < \theta_\mu < 140^\circ, p_\mu > 800 \text{ MeV}$	26.5% (30.8%)	27.8% (29.3%)
$6^\circ < \theta_\mu < 17^\circ, p_\mu > 6 \text{ GeV}$	3.0% (3.0%)	2.0% (2.1%)
1st muon $20^\circ < \theta_{\mu_1} < 160^\circ$ and 2nd muon:		
$6^\circ < \theta_{\mu_2} < 17^\circ$	13.0% (15.0%)	10.7% (11.1%)
1st muon $20^\circ < \theta_{\mu_1} < 160^\circ, p_{\mu_1} > 800 \text{ MeV}$ and 2nd muon:		
$6^\circ < \theta_{\mu_2} < 17^\circ, p_{\mu_2} > 6 \text{ GeV}$	5.7% (6.4%)	5.3% (5.6%)
$E_{clu,spa} > 2 \text{ GeV}$		
none	32.7% (34.5%)	2.1% (3.3%)

**Table 2.1:** Influence of different polar angle and momentum cuts for the decay leptons from  $J/\psi$  mesons produced in resolved photon and photon gluon fusion processes generated with the Monte Carlo generator EPJPSI. The cuts are motivated by the detector acceptance regions. The numbers in parenthesis give the percentage when selecting events with  $p_{t,J/\psi} > 1 \text{ GeV}$  only (the number of events which remain after applying the cut are again taken as 100%). The values of the last row show the percentage of events which have a cluster with  $E > 2 \text{ GeV}$  in the backward calorimeter. These events are capable of firing the IET trigger (see section 1.2.6).

27.3%, and  $B(\chi_{c2} \rightarrow J/\psi\gamma) = 13.5\%$  [16] (see figure 2.1). The dominant contribution is expected to come from  $c\bar{c}$  pairs which are produced in color singlet states [17].

Resolved photon events in the color singlet model can be simulated with the Monte Carlo generator EPJPSI. Figure 2.8 shows the number of generated events as a function of  $z$ ,  $W_{\gamma p}$  and  $p_{t,J/\psi}$ . Note that for resolved processes very few events are lost when decreasing the upper polar angle cut for the decay muons by  $20^\circ$ . Especially in the lowest  $z$  bin the loss is almost negligible.

Figure 2.9 shows the influence of geometrical and analysis cuts on the number of generated resolved photon Monte Carlo events in terms of efficiencies. The total selection efficiency has been split up into

- Geometry: Two muons with  $20^\circ < \theta < 140^\circ$  and  $p > 0.8 \text{ GeV}$  required (on generator level).
- Analysis: Both muon tracks have to be reconstructed, one muon has to be detected in the instrumented iron, and  $90 < W_{\gamma p} < 300 \text{ GeV}$ .
- Total: The product of the above efficiencies.

The geometrical efficiency decreases strongly at low  $z$  since the fraction of events with two decay leptons in the central detector region decreases (compare to figure 2.7). The  $W_{\gamma p}$  region of maximum acceptance is  $90 < W_{\gamma p} < 300 \text{ GeV}$ . The efficiency rises with  $p_{t,J/\psi}$  because the

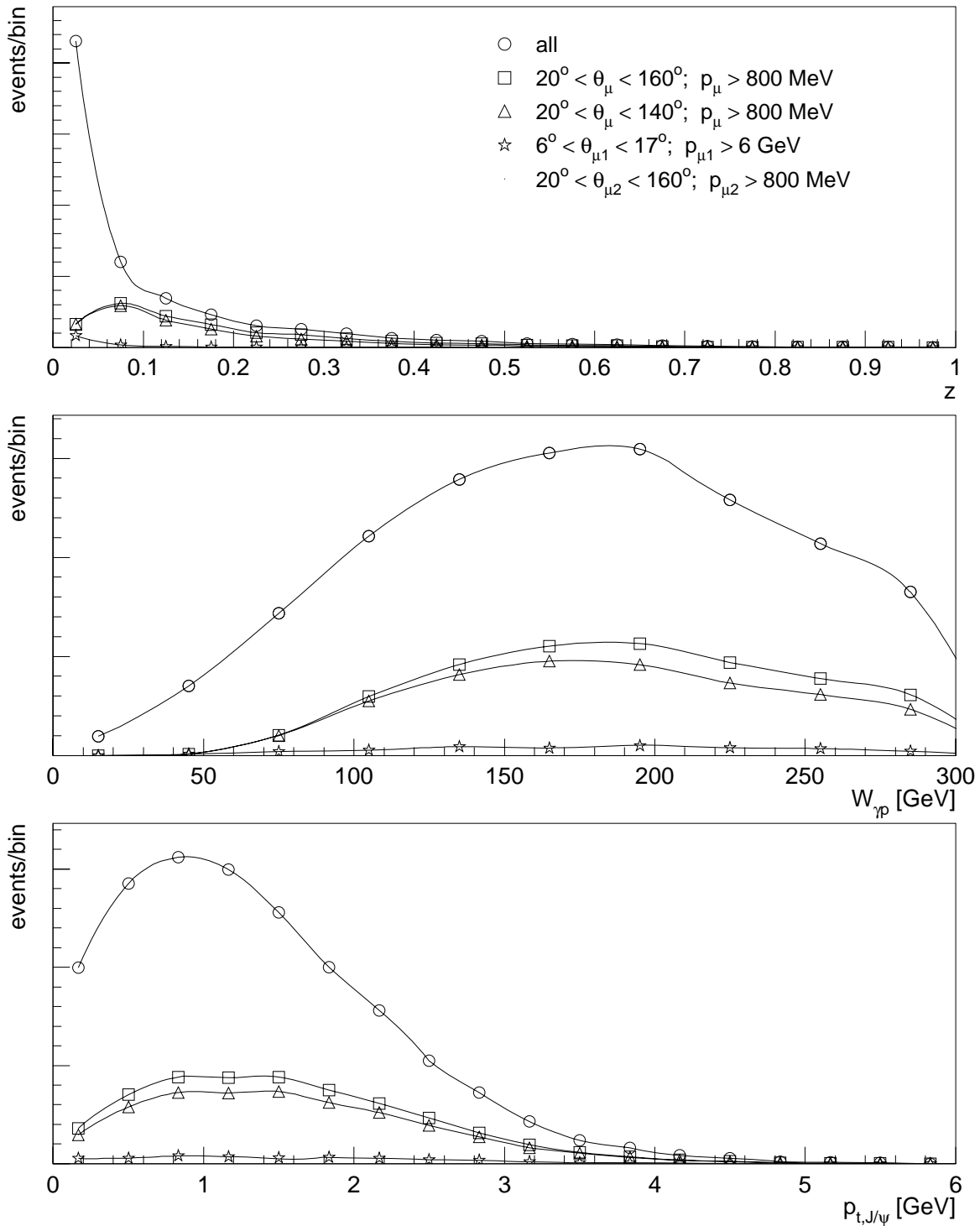


**Figure 2.8:** Number of resolved photon events generated with EPJPSI (CSM) as a function of  $z$ ,  $W_{\gamma p}$  and  $p_{t, J/\psi}$  (circles). The squares show the remaining events after requiring that the two decay muons can be detected in the central detector region. The triangles show the number of events remaining if the upper polar angle cut for the decay muons is decreased by  $20^\circ$  to  $140^\circ$ . The stars show the number of events with one muon being detected in the forward muon detector.

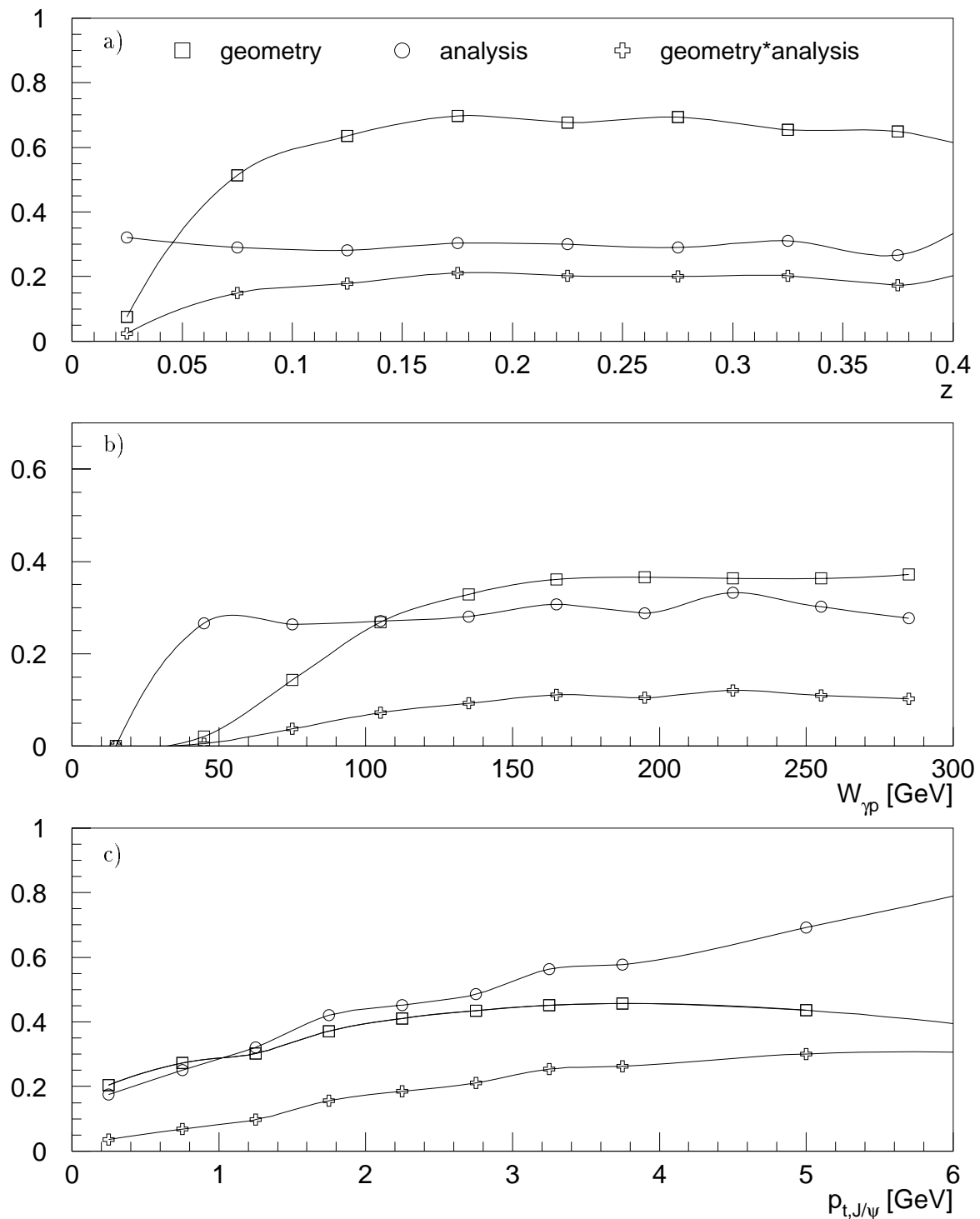


**Figure 2.9:** Selection efficiency as a function of a)  $z$ , b)  $W_{\gamma p}$  and c)  $p_{t, J/\psi}$  as determined from **resolved photon** Monte Carlo simulation. Geometry (squares):  $20^\circ < \theta < 160^\circ$  and  $p > 800$  MeV for both muons. Analysis (circles):  $90 < W_{\gamma p} < 300$  GeV and at least one muon detected in the instrumented iron. Total (plus signs): The product of the previous two efficiencies.

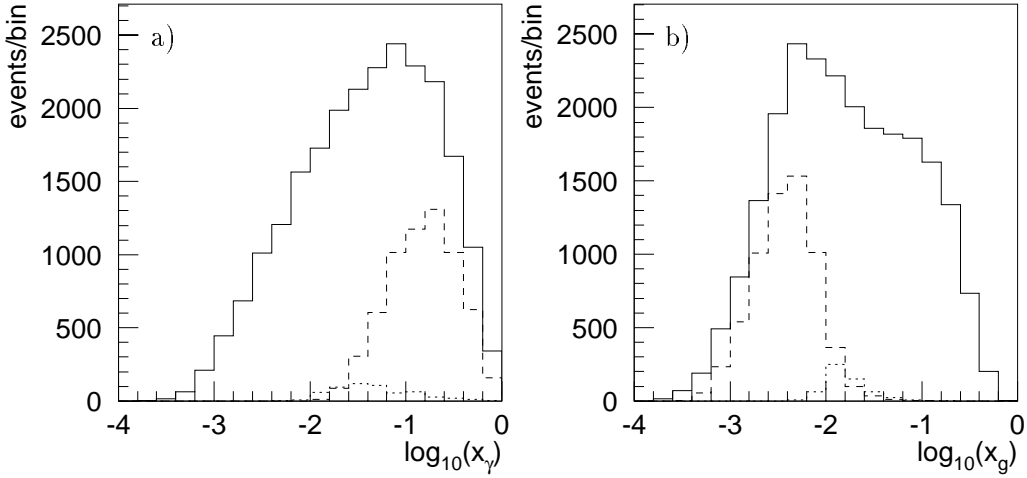


**Figure 2.10:**  $x_\gamma$  (left) and  $x_g$  (right) distributions for resolved photon events. The solid lines show the number of all generated events, the dashed lines show the remaining events when requiring that both decay leptons can be detected in the central detector region. The dotted lines show the number of events with one muon being detected in the forward muon detector and the other muon in the central detector region.

decay leptons from high  $p_t$   $J/\psi$  mesons have comparably large transverse momenta and are often found in the central detector region.

Figure 2.10 shows the  $x_\gamma$  and  $x_g$  distributions of resolved photon events. After detector acceptance cuts the process is sensitive to the parameterization of the PDFs in the range  $0.01 \lesssim x_\gamma \lesssim 1$  and  $0.001 \lesssim x_g \lesssim 0.01$ .

### 2.4.3 $B$ Meson Decay

The NLO QCD prediction for the production cross section of  $b$  quarks in  $\gamma p$  interactions is about two orders smaller than for charm production [18]:

$$\sigma(\gamma p \rightarrow b\bar{b} + X) \simeq 50 \text{ nb.} \quad (2.12)$$

The theoretical uncertainty is about a factor  $\sim 2$ . A recent H1 measurement of the semi leptonic  $B$  meson decay [19] obtained a value which is roughly a factor  $\sim 3$  larger than the quoted value. Measurements at higher center of mass energies at the Tevatron also show deviations towards a larger cross section.

If a  $B$  meson is produced it decays with a branching ratio of  $1.14 \pm 0.06\%$  [16] into  $J/\psi + X$ .  $J/\psi$  mesons from  $B$  meson decays can be simulated with the Monte Carlo generator EPJPSI. Assuming the NLO QCD  $b$  cross section the total number of decays  $B \rightarrow J/\psi + X$  which can be detected with the H1 detector in 1997<sup>2</sup> is  $\sim 10$ . A characteristic feature of the  $B$  meson is its comparably long lifetime ( $c\tau \simeq 500\mu\text{m}$ ). With the help of the newly installed CST it will be possible to spatially separate the primary event vertex from the  $B$  decay vertex.

<sup>2</sup>where  $J/\psi$  decays into 2 muons and the data is selected as described in chapter 4

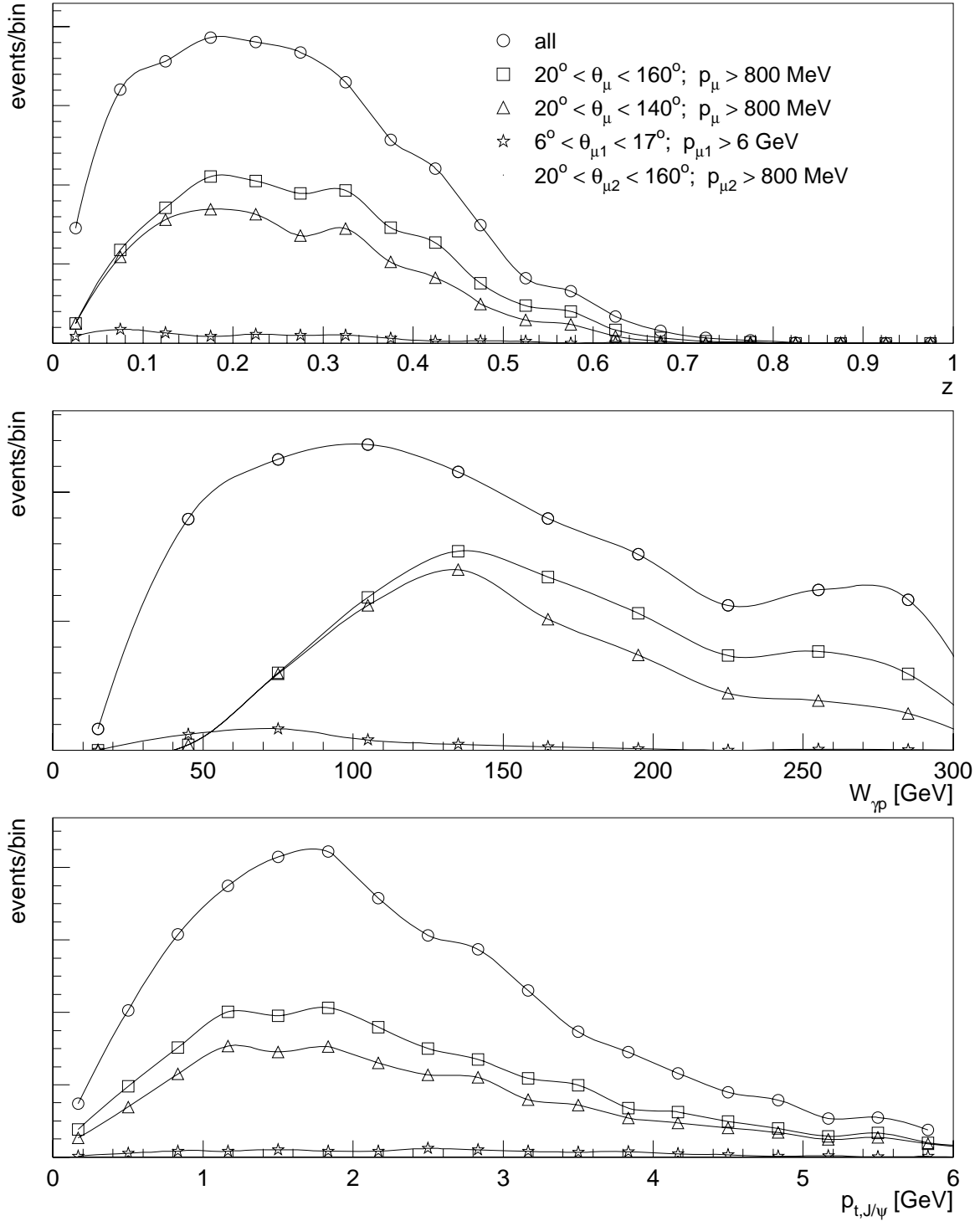


**Figure 2.11:** Number of  $B \rightarrow J/\psi + X$  decays generated with EPJPSI as a function of  $z$ ,  $W_{\gamma p}$  and  $p_{t,J/\psi}$  (circles). The squares show the remaining events after requiring that the two decay muons can be detected in the central detector region. The triangles show the number of events remaining if the upper polar angle cut for the decay muons is decreased by  $20^\circ$  to  $140^\circ$ . The stars show the number of events with one muon being detected in the forward muon detector.

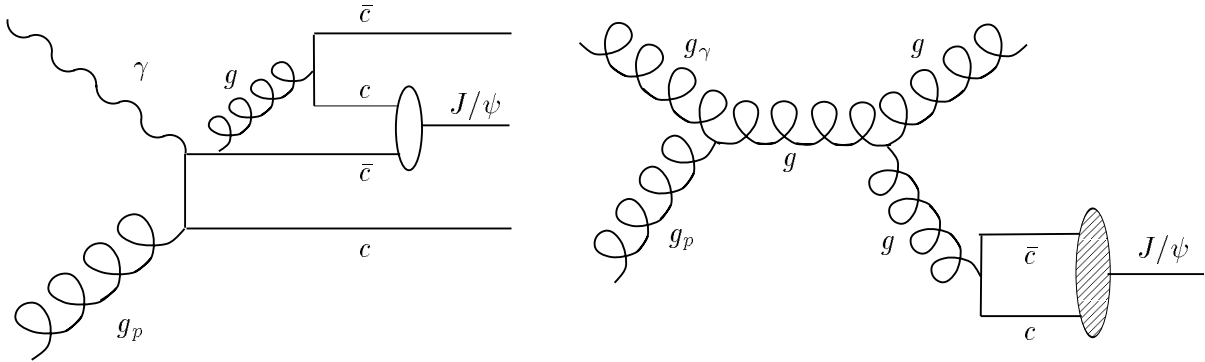


**Figure 2.12:** Feynman diagrams in leading order of  $\alpha_s$  for  $J/\psi$  meson production in fragmentation: color singlet model (left) and color octet model (right).

Figure 2.11 shows the number of generated events as a function of  $z$ ,  $W_{\gamma p}$  and  $p_{t,J/\psi}$ . Note that  $J/\psi$  mesons from  $B$  decays show a maximum at  $z \sim 0.25$ . The  $p_{t,J/\psi}$  distribution has a maximum at  $\sim 1.75$  and drops off more slowly than for  $J/\psi$  mesons from photon gluon fusion processes. As for resolved photon processes it is not desirable to restrict a  $B \rightarrow J/\psi + X$  analysis to the kinematic range  $40 \lesssim W_{\gamma p} \lesssim 180$  GeV as was done in previous analyses which were aiming at photon gluon fusion processes.

#### 2.4.4 Fragmentation

Fragmentation in the color octet model plays an important role at  $p\bar{p}$  colliders. Though at present one expects only small contributions at HERA, the basic principle of fragmentation will be explained here. Figure 2.12 shows the Feynman diagram in leading order of  $\alpha_s$  for  $J/\psi$  meson production in fragmentation in the color singlet and color octet models. Fragmentation is the formation of a hadron within a jet produced by a parton with large transverse momentum. The fragmentation cross section for the production of a high  $p_t$  hadron  $H$  in hadron hadron collisions is given by [20]

$$d\sigma(AB \rightarrow H(p_t) + X) = \sum_{ijk} \int_0^1 dx_1 f_{j/A}(x_1) \int_0^1 dx_2 f_{k/B}(x_2) \times \int_0^1 dx d\hat{\sigma}(jk \rightarrow i(p_t/x) + X) D_{i \rightarrow H}(x), \quad (2.13)$$

where  $f_{j/A,B}$  are the parton distributions of hadron  $A$  and  $B$ , and  $x$  is the longitudinal momentum fraction of the hadron  $H$  relative to parton  $i$ .  $D_{i \rightarrow H}$  are the fragmentation functions which represent the probability of parton  $i$  to fragment into the hadron  $H$  (+ $X$ ). The formula implicitly contains three arbitrary momentum scales: the factorization scale  $\mu_F$ , the fragmentation scale  $\mu_{frag}$  and the renormalization scale  $\mu_R$ .

In the NRQCD framework the fragmentation functions for charmonium have the form

$$D_{i \rightarrow H}(x, \mu_F) = \sum_n d_{i \rightarrow n}(x, \mu_F) \langle \mathcal{O}_n^H \rangle, \quad (2.14)$$

where  $d_{i \rightarrow n}(x, \mu)$  is the probability for the parton  $i$  to form a jet with a  $c\bar{c}$  pair in state  $n$  carrying the longitudinal momentum fraction  $x$ .  $\langle \mathcal{O}_n^H \rangle$  is proportional to the probability for a pointlike

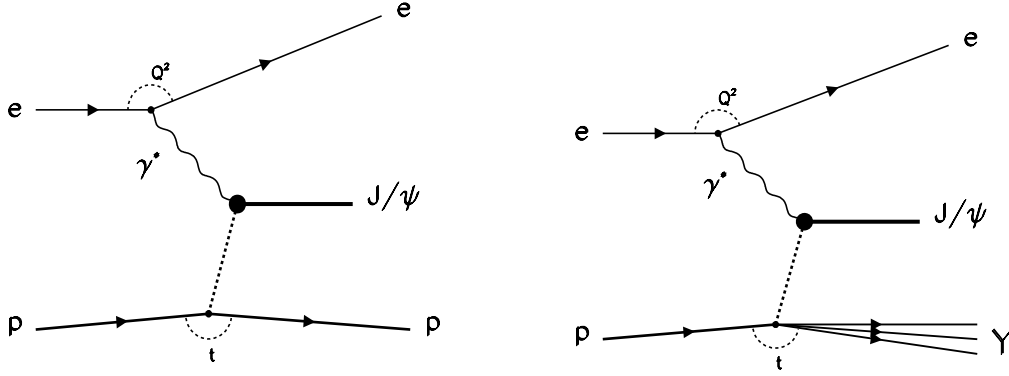


**Figure 2.13:** Feynman diagrams for diffractive processes: elastic (left) and proton dissociative (right).

$c\bar{c}$  pair to form a charmonium state  $n$ .  $d_{i \rightarrow n}(x, \mu_F)$  can be calculated as perturbation expansion in  $\alpha_s(\mu_F)$ .

### 2.4.5 Diffraction

$J/\psi$  mesons can also be produced in diffractive interactions. Experimentally diffractive events are characterized by a large *rapidity gap* between the hadronic final state (i.e. the  $J/\psi$  meson) and the proton remnant system. In this picture the interaction is mediated by the exchange of a colorless *pomeron*. The pomeron is part of the *Regge* theory. The Regge theory was developed to describe diffractive processes on a phenomenological basis and was motivated by the physics of optical diffraction. Figure 2.13 shows a Feynman graph of diffractive  $J/\psi$  production, where  $t$  is the four momentum exchange at the proton vertex. The process can be understood in such a way that the photon fluctuates in a  $J/\psi$  meson (this is described in the vector meson dominance model [22]) which successively interacts with the proton by the exchange of a pomeron. Diffractive events are dominantly found at large  $z \gtrsim 0.9$  and low transverse  $J/\psi$  momenta. One distinguishes between elastic diffraction, where the proton stays intact, and proton dissociation, where the proton breaks up. The border between diffraction and perturbative QCD is not always clear and may change in future. It is likely that the two models have an overlapping domain of applicability. An introduction to *soft* physics can be found in [23]. A cut  $p_{t,J/\psi} > 1$  GeV was proposed by theorists to remove diffractive contributions.

Diffractive events can be simulated with the Monte Carlo generator DIFFVM<sup>3</sup>. Figure 2.14 shows the number of generated proton dissociative events as a function of  $z$ ,  $W_{\gamma p}$  and  $p_{t,J/\psi}$ .

### 2.4.6 Background Processes

Pions and other hadrons can be misidentified as muons (punch through). It is also possible that real muons from other processes contribute as background. The most important background processes are:

<sup>3</sup>The default settings used for Monte Carlo generation with DIFFVM are listed in appendix E

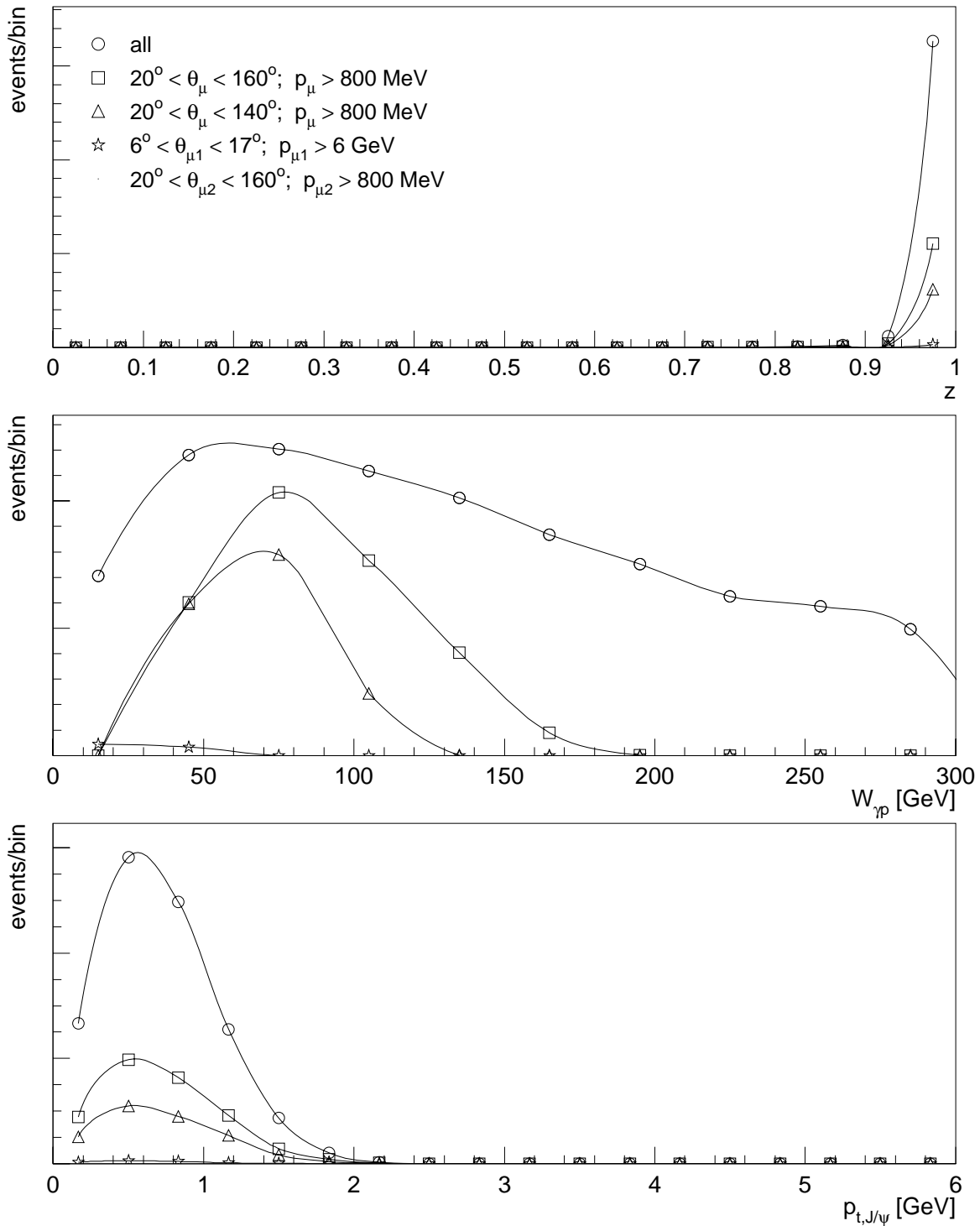


**Figure 2.14:** Number of diffractive proton dissociative events generated with DIFFVM as a function of  $z$ ,  $W_{\gamma p}$  and  $p_{t, J/\psi}$  (circles). The squares show the remaining events after requiring that the two decay muons can be detected in the central detector region. The triangles show the number of events remaining if the upper polar angle cut for the decay muons is decreased by  $20^\circ$  to  $140^\circ$ . The stars show the number of events with one muon being detected in the forward muon detector.

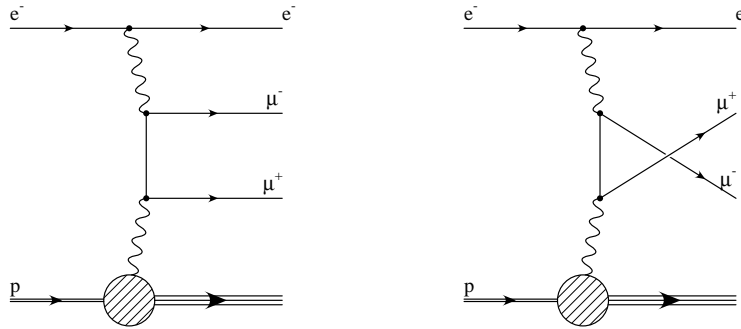


**Figure 2.15:** Feynman diagrams for muon pair production via two photon exchange.

- Hadrons containing lighter quarks (u,d,s) or charmed mesons produced via photon gluon fusion decay into one or more muons. The branching ratios are comparably small but the production cross section for lighter quarks is many orders of magnitude larger than the one for heavier quarks resulting in a non negligible contribution.
- $B$  mesons are produced in pairs. Each meson can then decay into a  $J/\psi$  meson (branching ratio  $\sim 1\%$ ) or more likely via a semi leptonic decay into one muon and a neutrino ( $\sim 10\%$ ). Recent H1 studies [19] indicate a  $b$  cross section which is significantly larger than predicted by NLO QCD calculations. Contributions from  $B$  mesons can be quantified in future with the help of the silicon micro-vertex detector.
- A  $\Psi(2S)$  decays with a branching ratio of 57% [16] into a  $J/\psi$ . Since these events cannot be separated experimentally from events with direct  $J/\psi$  mesons the contributions from  $\Psi(2S)$  are usually included in theoretical predictions. One expects approximately 15% of the  $J/\psi$  signal to originate from decaying  $\Psi(2S)$  mesons [30].
- Electromagnetic lepton pair production via two photon interactions. See figure 2.15.

## 2.5 The Extraction of Color Octet Matrix Elements

The color octet matrix elements (COME) of equation 2.9 can in principle be extracted within the NRQCD formalism from the data of different experiments ( $p\bar{p}$ ,  $ep$ ,  $e^+e^-$ , fixed target). The COME which are relevant for HERA  $J/\psi$  meson production have first been extracted by Cho and Leibovich in [47] from prompt<sup>4</sup>  $J/\psi$  production in  $p\bar{p}$  collisions at the Tevatron. In a recent publication Cano-Coloma and Sanchis-Lozano studied the influence of higher-order QCD effects induced by initial-state radiation in a Monte Carlo framework [24]. Significantly smaller values for the COME were obtained by this analysis. Kramer and Kniehl performed a fit to the latest Tevatron data [17] incorporating this information. HERA predictions which use the new, smaller COME are called higher order predictions in the following. Sridhar, Martin and Stirling [25] take another approach. They argue that the intrinsic transverse momentum,  $k_t$ , of the partons inside the proton must not be neglected in Tevatron and above all in HERA calculations. Adding initial state gluon radiation and intrinsic transverse momentum of the partons are essentially different ways of accounting for some higher order  $\alpha_s$  terms which are considered important.

<sup>4</sup> $J/\psi$  mesons are called *prompt* if they come from the primary vertex within the resolution of micro-vertex detectors.  $J/\psi$  mesons from the decay of a  $B$  meson for example are not prompt.

Prompt  $J/\psi$  production in  $p\bar{p}$  collisions is sensitive to  $\langle \mathcal{O}[\underline{8},^3 S_1] \rangle$  and a linear combination of  $\langle \mathcal{O}[\underline{8},^1 S_0] \rangle$  and  $\langle \mathcal{O}[\underline{8},^3 P_0] \rangle$ . This induces some uncertainty in the color-octet contributions at HERA. Predictions are sometimes shown for two scenarios: a) assuming  $\langle \mathcal{O}[\underline{8},^1 S_0] \rangle = 0$  and b)  $\langle \mathcal{O}[\underline{8},^3 P_0] \rangle = 0$ . The results which were obtained by several authors are summarized in table 2.2.

state	value (LO) [GeV <sup>3</sup> ]	value (HO) [GeV <sup>3</sup> ]	scaling
Kniehl and Kramer [17]			
$\langle \mathcal{O}[\underline{1},^3 S_1] \rangle$	$(7.63 \pm 0.54) \cdot 10^{-1}$	$(1.3 \pm 0.09)$	$[m_c^3 v^3]$
$\langle \mathcal{O}[\underline{8},^3 S_1] \rangle$	$(3.94 \pm 0.63) \cdot 10^{-3}$	$(2.73 \pm 0.45) \cdot 10^{-3}$	$[m_c^3 v^7]$
$\langle \mathcal{O}[\underline{8},^1 S_0] \rangle + \frac{r}{m_c^2} \langle \mathcal{O}[\underline{8},^3 P_0] \rangle$	$(65.2 \pm 6.7) \cdot 10^{-3}$	$(5.72 \pm 1.84) \cdot 10^{-3}$	$[m_c^3 v^7]$
$r$	3.47	3.54	
Beneke, Krämer, Vanttinen [41]			
$\langle \mathcal{O}[\underline{1},^3 S_1] \rangle$	$11.6 \cdot 10^{-1}$		$[m_c^3 v^3]$
$\langle \mathcal{O}[\underline{8},^3 S_1] \rangle$	$10.6 \cdot 10^{-3}$		$[m_c^3 v^7]$
Scenario I:			
$\langle \mathcal{O}[\underline{8},^1 S_0] \rangle$	$30 \cdot 10^{-3}$		$[m_c^3 v^7]$
$\langle \mathcal{O}[\underline{8},^3 P_0] \rangle \cdot 3/m_c^2$	0.0		
Scenario II:			
$\langle \mathcal{O}[\underline{8},^1 S_0] \rangle$	0.0		$[m_c^3 v^7]$
$\langle \mathcal{O}[\underline{8},^3 P_0] \rangle \cdot 3/m_c^2$	$30 \cdot 10^{-3}$		
Cano-Coloma, Sanchis-Lozano ([24],CTEQ2L)			
$\langle \mathcal{O}[\underline{8},^3 S_1] \rangle$		$(3.3 \pm 0.5) \cdot 10^{-3}$	$[m_c^3 v^7]$
$\langle \mathcal{O}[\underline{8},^1 S_0] \rangle + \langle \mathcal{O}[\underline{8},^3 P_0] \rangle \cdot 3/m_c^2$		$(14.4 \pm 2.1) \cdot 10^{-3}$	$[m_c^3 v^7]$
Sridhar, Martin, Stirling [25]			
	$\langle k_t \rangle = 0$ GeV	$\langle k_t \rangle = 1$ GeV	
$\langle \mathcal{O}[\underline{8},^3 S_1] \rangle$	$(12.6 \pm 3.3) \cdot 10^{-3}$	$(15.0 \pm 2.9) \cdot 10^{-3}$	$[m_c^3 v^7]$
$\langle \mathcal{O}[\underline{8},^1 S_0] \rangle + \langle \mathcal{O}[\underline{8},^3 P_0] \rangle \cdot 3/m_c^2$	$(94.2 \pm 17.4) \cdot 10^{-3}$	$(70.5 \pm 11.7) \cdot 10^{-3}$	$[m_c^3 v^7]$
Cho, Leibovich [26]			
$\langle \mathcal{O}[\underline{8},^3 S_1] \rangle$	$(6.6 \pm 2.1) \cdot 10^{-3}$		$[m_c^3 v^7]$
$\langle \mathcal{O}[\underline{8},^1 S_0] \rangle + \langle \mathcal{O}[\underline{8},^3 P_0] \rangle \cdot 3/m_c^2$	$(66 \pm 15) \cdot 10^{-3}$		$[m_c^3 v^7]$

**Table 2.2:** Values of the color octet matrix elements used in recent publications.

## Chapter 3

# Event Reconstruction

In this chapter the reconstruction of kinematical variables and the selection of photoproduction events will be described. Issues concerning the forward region of the H1 detector will be discussed at the end of this chapter.

### 3.1 Reconstruction of Kinematical Variables

The exact procedure for the reconstruction of the scaling variable  $y$  is described separately in section 3.1.1. As soon as the variable  $y$  has been reconstructed further relevant kinematical variables can be derived as follows:

The energy in the  $\gamma p$  system is

$$W_{\gamma p}^2 \simeq y \cdot s \text{ (in photoproduction)}. \quad (3.1)$$

The inelasticity  $z$  of the  $J/\psi$  meson is given by

$$z = \frac{\sum_{i=\{\mu_1, \mu_2\}} E_i - p_{z,i}}{2E_e \cdot y}, \quad (3.2)$$

where the momentum of the muons is measured in the tracking chambers, and  $E_i = \sqrt{p_i^2 + m_\mu^2}$ . Figure 3.1 shows a comparison of the reconstructed  $z$  and  $W_{\gamma p}$  values with their generated values (for a resolved photon Monte Carlo). Figure 3.2 shows the bin purities in each  $z$  and  $W_{\gamma p}$  bin as determined from a mixed Monte Carlo simulation (see section 4.5). The bin purity is the fraction of events in each bin which was reconstructed in the correct bin. The  $W_{\gamma p}$  bins used in the present analysis have been chosen to be rather wide to ensure a high bin purity ( $\sim 90\%$ ). The purity in the most interesting low and high  $z$  bins is better than 90%.

The  $J/\psi$  meson's rapidity is

$$\hat{y}_{J/\psi} = \frac{1}{2} \cdot \ln \frac{E_{J/\psi} + p_{z,J/\psi}}{E_{J/\psi} - p_{z,J/\psi}}, \quad (3.3)$$

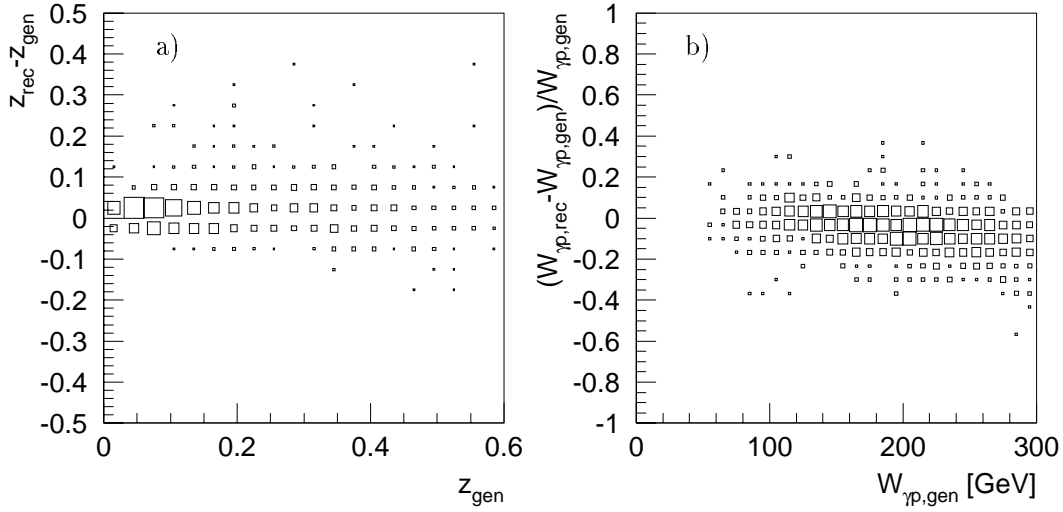


**Figure 3.1:** Comparisons of the reconstructed value of  $z$  (left) and  $W_{\gamma p}$  (right) to their generated values for a resolved photon Monte Carlo simulation.

where  $E_{J/\psi} = \sqrt{p_{J/\psi}^2 + m_{J/\psi}^2}$ . The meson's pseudorapidity is defined by

$$\eta_{J/\psi} = -\ln \tan \frac{\theta_{J/\psi}}{2}. \quad (3.4)$$

### 3.1.1 Reconstruction of $y$

At HERA the kinematical variable  $y$  can either be reconstructed via the measured variables of the scattered electron (*electron method*) or the hadronic final state (*Jacquet Blondel method*). In deep inelastic scattering the measurement is thus overconstrained. The redundancy in measured variables can be used in favor of a smaller error (*sigma method*). In photoproduction the electron will escape in the beam pipe and one relies completely on the hadronic final state. An overview of available methods is given here, focusing on the *Jacquet Blondel* method as the relevant method for this analysis.

1. The *electron method* uses the energy and polar angle of the scattered electron:

$$y_e = 1 - \frac{E'_e}{E_e} \cdot \sin^2 \frac{\theta_e}{2}. \quad (3.5)$$

At high  $y$  this method is superior to all other methods. However it is sensitive to initial state radiation which must be taken into account in Monte Carlo simulations. If the electron was detected in one of the electron taggers ( $\sin^2 \frac{\theta_e}{2} \sim 1$ ) one obtains

$$y_e = 1 - \frac{E'_e}{E_e}. \quad (3.6)$$

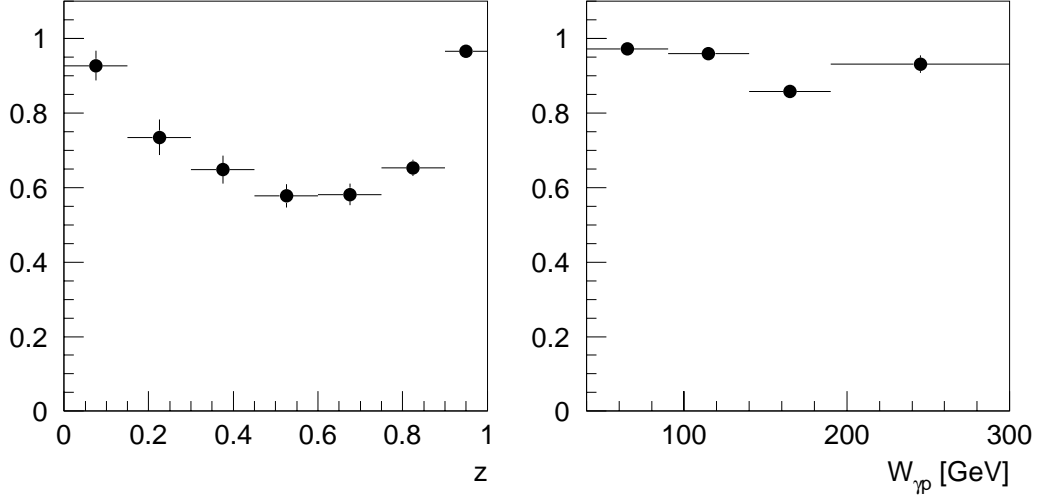


**Figure 3.2:** Bin purities for  $z$  bins (left) and  $W_{\gamma p}$  bins (right) as determined from the mixed Monte Carlo simulation which is derived in chapter 4.

2. The *double angle method* uses only the polar angles of the electron and the hadronic final state. It is independent of the energy calibration of the detector and initial state radiation.

$$y_{DA} = \frac{\sin \theta_e \cdot (1 - \cos \theta_h)}{\sin \theta_h + \sin \theta_e - \sin(\theta_e + \theta_h)}, \quad (3.7)$$

where  $\theta_h$  is the polar angle of the hadronic final state.

3. The  $\Sigma$  *method* makes use of the redundancy of the measured variables in favor of a smaller error:

$$y_{\Sigma} = \frac{\sum_{had,final,state} (E_i - p_{z,i})}{\sum_{all\ particles} (E_i - p_{z,i})} \quad (3.8)$$

4. Finally in the case of the *Jacquet Blondel method* a straight forward calculation gives:

$$y_{jb} = \frac{\sum_{had,fin.state} E_i - p_{z,i}}{2 \cdot E_e} \quad (3.9)$$

The sums in the numerator of equations 3.8 and 3.9 include all particles of the final state except the incident particles. Each particle's energy and the  $z$  component of the momentum can be approximately determined from the calorimetric energy deposition and the momentum as measured by the tracking chambers. The following recipe will be applied to reduce measurement errors: For charged particles the momentum and energy as measured by the tracking chambers will be used (assuming a pion rest mass when calculating the energy). The remaining contributions to the sum are determined from the energies of the calorimeter cells. To avoid double counting each track will be extrapolated from the tracking chambers to a point in front of the calorimeter surface. All calorimeter cells within a cone starting from this point and opening in the direction of flight will be excluded from the sum. Best results are obtained using opening angles of  $2 \cdot 7^\circ$  in  $\theta$  and  $2 \cdot 14^\circ$  in  $\phi$ . Note that the most relevant terms in the above sum come from particles

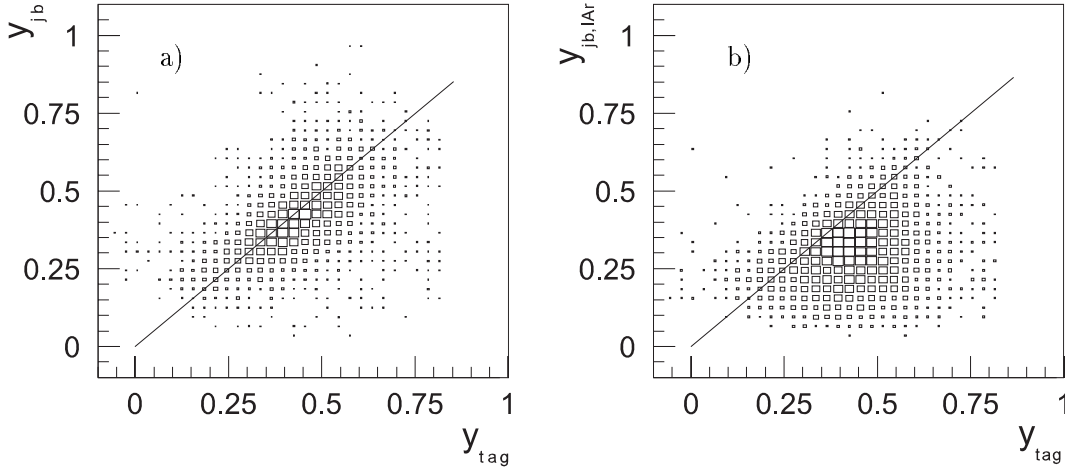


**Figure 3.3:**  $y_{jb}$  compared to the electron method  $y_{tag}$ . a) including the Spacal and b) using only the liquid argon calorimeter.

directed towards the backward region of the detector. In previous photoproduction analyses the backward region, namely the Spacal, has not been included for the reconstruction of  $y$  [11, 12]. This is acceptable for the  $J/\psi$  production process which is dominant for  $0.3 < z < 0.9$  (photon gluon fusion) — one does not expect any energy depositions in the backward calorimeter. For this analysis, which is aiming at other production processes as well it is mandatory to include the Spacal. Figure 3.3 compares  $y_{jb}$  with  $y_e$  for *tagged* data events.  $y_e$  has been reconstructed using the energy of the scattered electron as measured by the e-Tagger at  $-33$  m. In a) the Spacal was included, in b) only the liquid argon calorimeter was used.

Including the Spacal has to be done with care since contributions from the scattered electron have to be identified as such and must not be included in the above sum. The identification of the electron will be described in detail in section 3.2. The scattered electron often deposits most of its energy in the innermost hadronic cells or the electromagnetic veto cells (see figure 1.7). As a result these cells will be excluded from the summation. The same applies to the Spacal's backward plug cells which show a poor energy calibration and are probably dominated by background. For all hadronic Spacal cells a correction factor of 1.5 on the final energy scale has been applied (see [27]).

### 3.1.2 Reconstruction of $x_\gamma$

In resolved photon processes only a fraction  $x_\gamma$  of the photon's four momentum is used in the interaction with a parton from the proton which in turn carries only the momentum fraction  $x_g$  of the proton. Four momentum conservation, when neglecting additional gluons which are radiated before the  $J/\psi$  meson is formed, yields

$$x_\gamma q + x_g p = p_{J/\psi}. \quad (3.10)$$

Multiplying equation 3.10 by  $p$  or  $p_{J/\psi}$  and combining the two resulting equations leads to

$$x_\gamma = z \cdot \frac{1 - (m_{J/\psi} m_p / 2 E_p E_e y)^2}{1 - (m_p e^{\hat{y}_{J/\psi}} / E_p)^2 / 2} \quad (3.11)$$

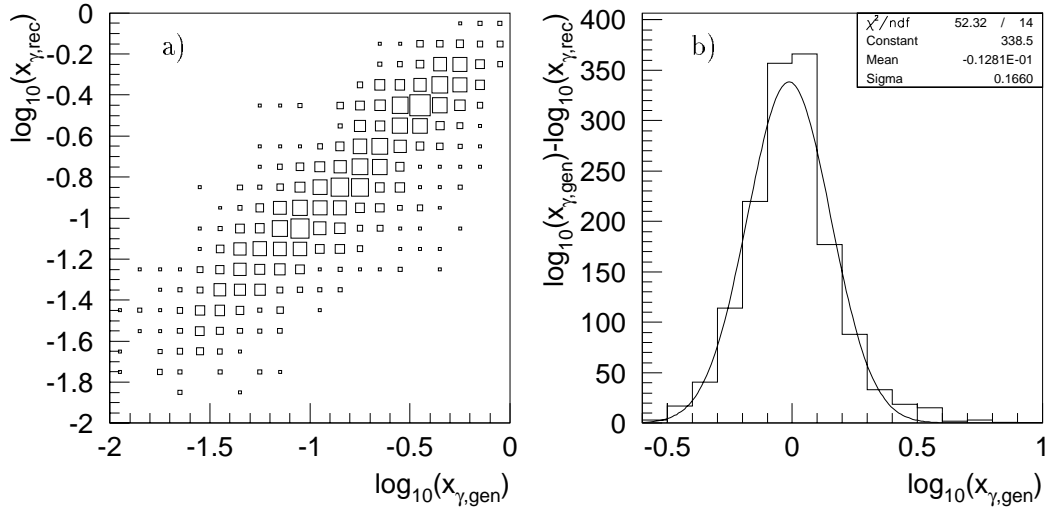


**Figure 3.4:** Comparison of the reconstructed value of  $x_\gamma$  with its generated value for a resolved photon Monte Carlo simulation.

The assumption that a real photon is emitted in the direction of the electron was made ( $q \simeq (E_\gamma, 0, 0, -E_\gamma)$ ,  $E_\gamma \simeq yE_e$  neglecting the electron mass). The reconstructed value is compared to the generated value in figure 3.4.

## 3.2 Identification of the Scattered Electron

Each event will be assigned to one of four **electron classes** with the aim to distinguish photoproduction from deep inelastic scattering events. The definition of each class is as follows (the numbers in parentheses show the relative size of each class based on all events passing the preselection cuts):

- No electron, photoproduction candidate (**class 0**, 80%)  
No cluster with  $E > 8$  GeV has been registered in any calorimeter. The veto layer energy and the summed energy of the innermost hadronic cells is less than 1.0 GeV each.
- Good electron in Spacal, DIS candidate (**class 1**, 16%)  
The Spacal contains a cluster with the following properties:
  1.  $E > 8$  GeV
  2. Energy weighted cluster radius  $r_{clu} < 3.4$  cm
  3. Distance to next BDC track  $d_{BDC} < 3.4$  cm
  4. Energy in the veto layer  $E_{veto} < 1$  GeV
  5. Hadronic energy behind electromagnetic cluster  $E_{had} < 0.5$  GeV
  6.  $\max(x, y) > 8.7$  cm, where x and y are the cluster center coordinates

For these events the electron or sigma method is applicable. The electron's energy and polar angle measurement is good and the misidentification probability should be negligible.

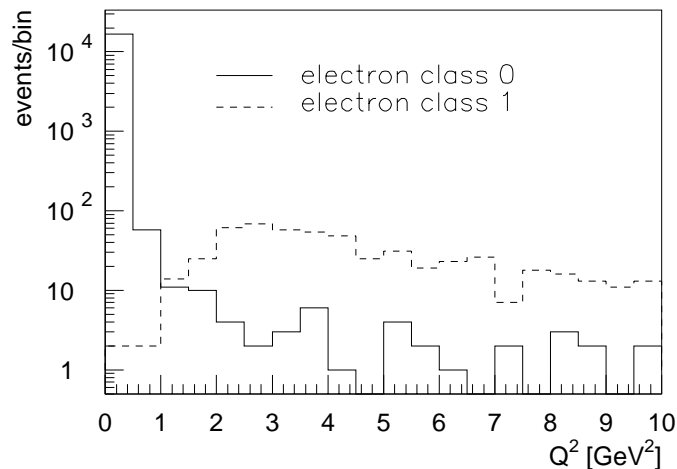


**Figure 3.5:** Generated  $Q^2$  distribution of a boson gluon fusion Monte Carlo for events which after reconstruction have been classified as photoproduction (electron class 0, solid line) and DIS events (electron class 1, dashed line).

- Poor electron, DIS candidate (**class 2**, 1%)  
A Spacal cluster fulfills only the first three conditions of class 1. It is still very likely that the cluster was caused by an electron, but energy and polar angle reconstruction may be poor.
- LAr electron, DIS candidate (**class 3**, 0.5%)  
A LAr cluster fulfills the first two conditions of class 1.
- Maybe electron (**class 4**, 2.5%)  
A cluster with  $E > 8$  GeV has been registered which does not belong to any other class. Events with more than 1.0 GeV summed energy in the Spacal veto layers or more than 1.0 GeV in the innermost hadronic Spacal cells are also assigned to this class.

Figure 3.5 shows the distribution of the generated  $Q^2$  value for events which have been assigned to electron class 1 (DIS candidates, dashed line) and class 0 (photoproduction candidates, solid line). A good separation of photoproduction and DIS events can be achieved (note the logarithmic scale). The number of events which cannot easily be classified as photoproduction or DIS (other classes, not shown) is negligible.

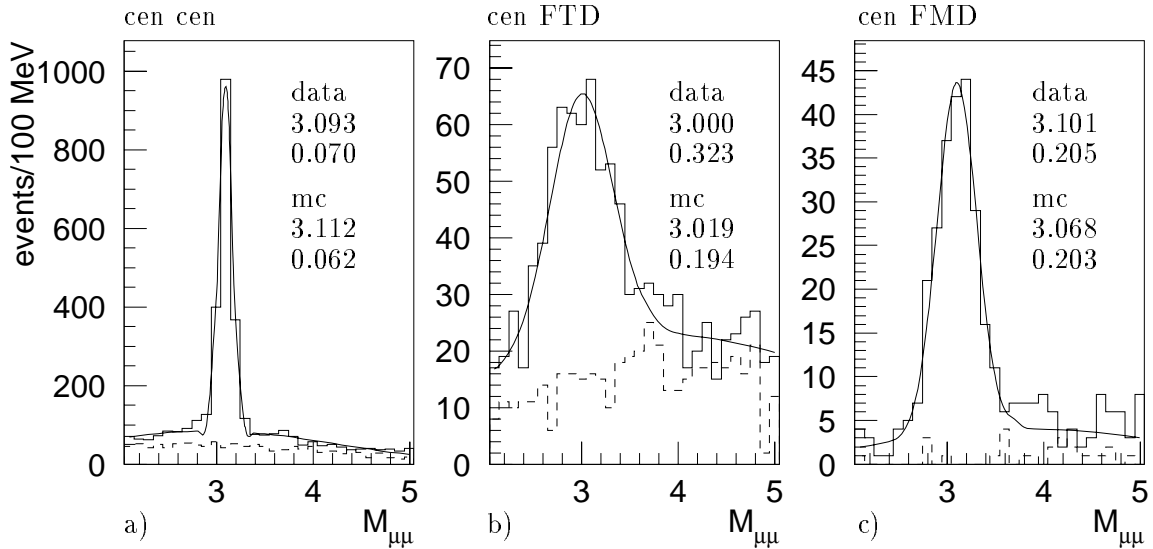


**Figure 3.6:** Invariant mass resolution for an inclusive  $J/\psi$  data set ( $z > 0.3$ ) with a) two central muons b) one central and one forward muon (momentum as measured by FTD) and c) one central and one forward muon (momentum as measured by FMD). The numbers represent the signal position and width for data (top) and Monte Carlo simulation (bottom, the Monte Carlo invariant mass signal is not shown). The dashed histograms show the spectrum of muon pairs with equal charge.

### 3.3 The Forward Region of the H1 Detector

Some investigations with the aim of including the forward region ( $\theta < 20^\circ$ ) in inelastic  $J/\psi$  analyses have been undertaken. Relaxing the polar angle cut for decay leptons below  $20^\circ$  would be especially interesting for the analysis of  $J/\psi$  mesons produced in a) resolved photon events or b) boson gluon fusion events at low  $W_{\gamma p}$ . In these processes the decay leptons are expected to be detected dominantly in the forward region (see chapter 2). Note that in the final analysis the decay muons are required to be in the central region due to the reasons which are summarized here and which are described in more detail in the following subsections:

- In regions of large background the poor momentum resolution of the forward tracking detector (resulting in a poor invariant mass resolution) does not allow to distinguish efficiently between background and signal events.
- The invariant mass signal of events with one muon measured in FTD is shifted towards lower invariant mass values.
- It is not clear whether the reconstruction efficiency of the forward muon detector is modelled adequately in the Monte Carlo simulation.

In addition it should be noted that varying the polar angle cut below  $20^\circ$  does not lead to consistent results in data and Monte Carlo simulation. According to resolved photon Monte Carlo, for example, one would expect the number of events with one muon below  $20^\circ$  to be roughly equal to the number of events with two central muons. Data however do not show any significant signal (for  $z < 0.15$ ) when requiring one forward muon.

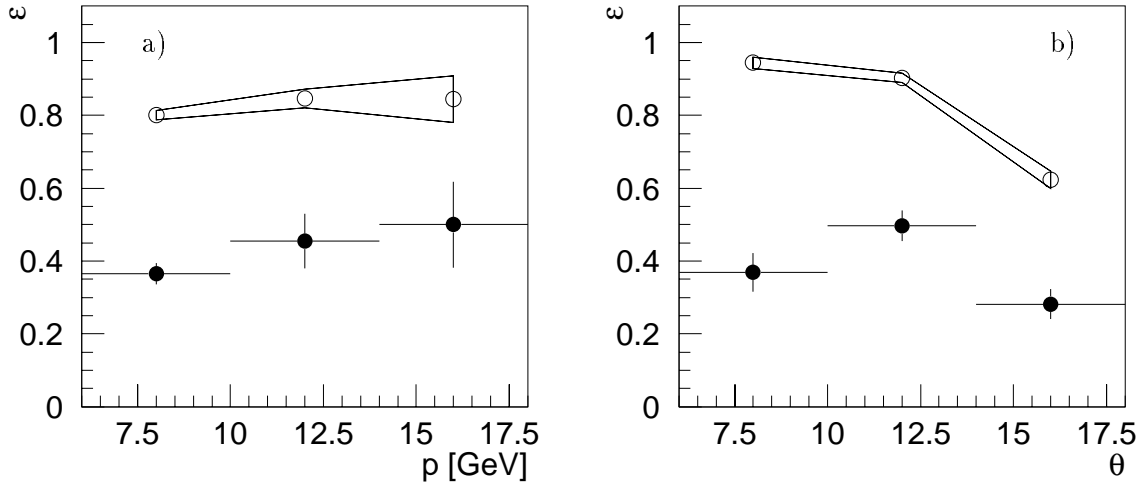


**Figure 3.7:** Reconstruction efficiency of the forward muon detector in data (full points) and Monte Carlo (open points) as a function of *a*) the muon's momentum  $p$  (integrated over  $6^\circ < \theta < 18^\circ$ ) and *b*) its polar angle  $\theta$  (for  $p > 6$  GeV). The statistical error of the Monte Carlo efficiency is shown as an error band.

### 3.3.1 Invariant Mass Resolution of the FTD and FMD

Figure 3.6 shows the invariant mass spectrum for an inclusive sample ( $z > 0.3$ ) with *a*) two central muons, *b*) one central and one forward muon using the momentum as measured by FTD and *c*) one central and one forward muon using the momentum as measured by FMD. The numbers in each histogram represent the Gaussian position and width of the fitted data signal (top) and the corresponding Monte Carlo expectations (bottom). The Monte Carlo signal is not shown. The signal with one track measured in the FTD is wider in data than in Monte Carlo simulation. Otherwise good to fair agreement of data and Monte Carlo is observed. For events with one forward muon measured in the FTD a shift towards lower invariant mass values is observed in data as well as in Monte Carlo simulation.

### 3.3.2 Reconstruction Efficiency of the Forward Muon Detector

The reconstruction efficiency of the forward muon detector can be estimated by selecting data events with exactly one muon detected in the forward iron endcap. The selected events must not have been triggered exclusively by a subtrigger of the forward muon detector. Roughly speaking the efficiency is the number of events which contain a reconstructed track in the forward muon detector (track quality 1 or 2 and requiring a link to a drift chamber track) divided by the total number of selected events. The results will be sensitive to the number of fake muons (hadrons behaving like a muon) in the selected data set. Hadrons tend to shower before they reach the FMD and thus the efficiency will be lowered. To reduce this effect, two methods have been applied: *a*) selecting two muon events and cutting on the invariant mass around the  $J/\psi$  mass and *b*) tighten the muon identification cuts (increase the number of hit forward endcap layers from 6 to 10 and require the muon to be identified in the calorimeter as well).

The results from both methods are compatible within statistics: The total efficiency (integrated over  $\theta$  and  $p$ ) was determined to be a factor  $\sim 2$  too high in Monte Carlo simulation. This value has to be seen as an upper bound since it is not entirely clear how large background

---

contributions are. Figure 3.7 shows the results from method b) as function of the muon's polar angle and momentum in data (full points) and Monte Carlo (open points). The influence of the required link between FMD and inner track needs further study. The observed large difference of data and Monte Carlo simulation might be caused by the FTD reconstruction and linking procedure. Furthermore the efficiency determination suffers from the momentum measurement in the FTD which is used for the data selection ( $p_{FTD} > 6$  GeV).



## Chapter 4

# Data Selection and Monte Carlo Simulation

In this chapter the selection of events with two muon candidates is described including the run selection, track selection, muon identification, analysis cuts and the selection of subtriggers. Data will be compared to Monte Carlo simulation in various kinematical ranges. Emphasis is put on the determination of trigger efficiencies from Monte Carlo simulation.

A schematic event display of a typical elastic and inelastic  $J/\psi$  meson event can be seen in figures 4.1 and 4.2. Table 4.1 summarizes all cuts which will be applied in the final data selection and which will be discussed in the following text.

cut	see section
<b>lepton identification:</b>	
at least one muon identified in the iron	4.1.2
$Q_c \geq 2$ for calorimeter muons	4.1.2
$p_\mu > 800$ MeV for both muons	4.1.3
$20^\circ < \theta_\mu < 160^\circ$ for both muons	4.1.3
$20^\circ < \theta_\mu < 140^\circ$ for both muons if $z < 0.15$	4.1.3
<b>photoproduction:</b>	
electron class 0	3.2
<b>kinematic range:</b>	
$p_{t,J/\psi} > 1$ GeV	5.2
$40 < W_{\gamma p} < 300$ GeV	5.2
<b>triggers:</b>	
S15/S19/S22/S56/S87	4.2

**Table 4.1:** Summary of the cuts which are used in the final data selection.

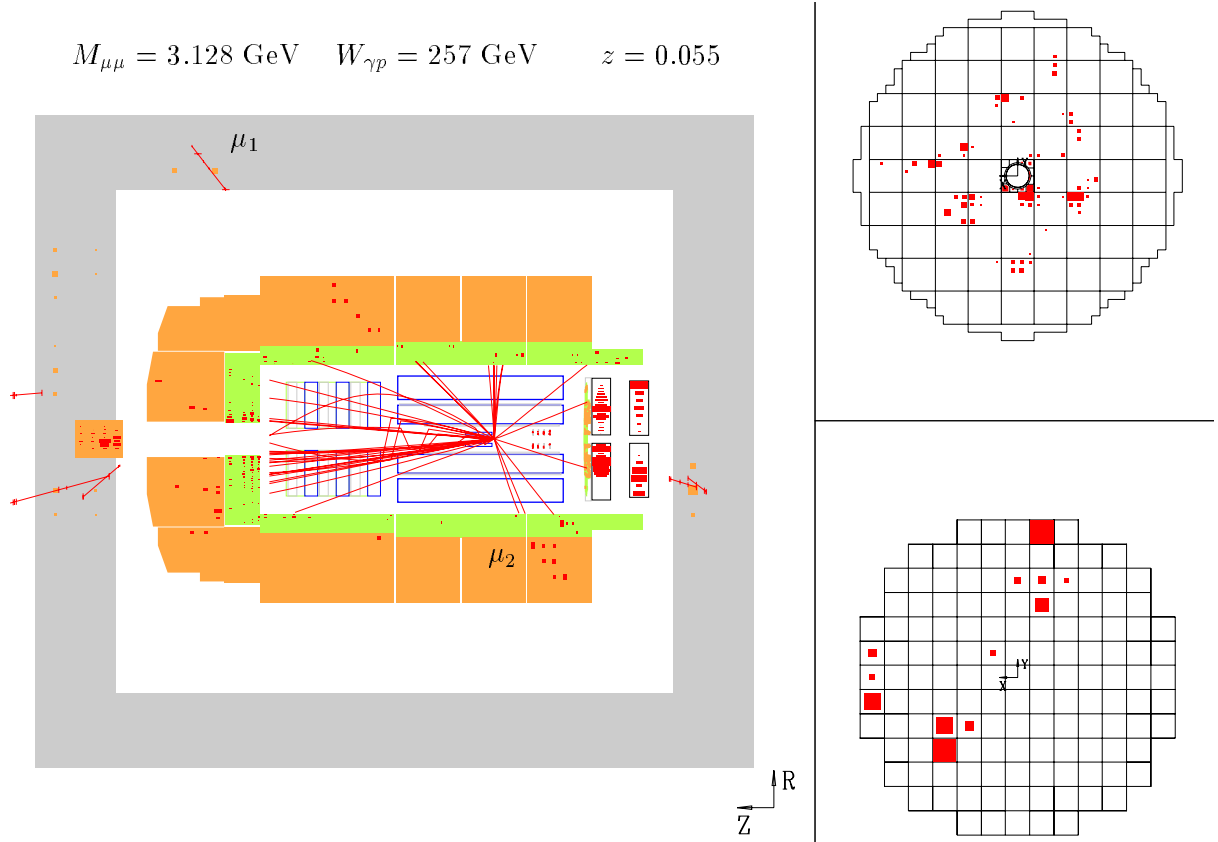


**Figure 4.1:** Schematic display of a candidate event for  $J/\psi$  meson production in a resolved photon process. A side view of the H1 detector is shown at the left and a radial view on the backward calorimeter at the right. One muon was identified in the instrumented iron, the other muon in the calorimeter. A wide spread energy deposition (most likely produced from the remnants of the photon) can be seen in the electromagnetic (top) and hadronic Spacal (bottom).

## 4.1 Preselection

The present analysis is based on  $ep$  data from the 1997 data taking period. All events are from class 24 (*two leptons*). The classification efficiency as determined from Monte Carlo simulation is  $\sim 100\%$ . All final analysis cuts are at least as tight as the ones used by the event classification. Events which contain beam halo muons (identified by the beam halo finder of the H1 Phan software package,  $\sim 100$  events) have been discarded. Only events from electron class 0 (see 3.2) have been selected to reject deep inelastic scattering events. Furthermore it was required that all relevant detector components were supplied with high voltage. Dictated by changing trigger setups the data has been divided into two different run ranges (see table 4.2).

Number	run range	$\int$ luminosity [ $pb^{-1}$ ]	subtriggers (*)
1.	179855 - 193432	8.605	S56 S19 S22 S87
2.	193433 - 200407	9.645	S56 S19 S22 S15 S87

**Table 4.2:** Run ranges. (\*) For a complete description of the trigger selection see section 4.2.

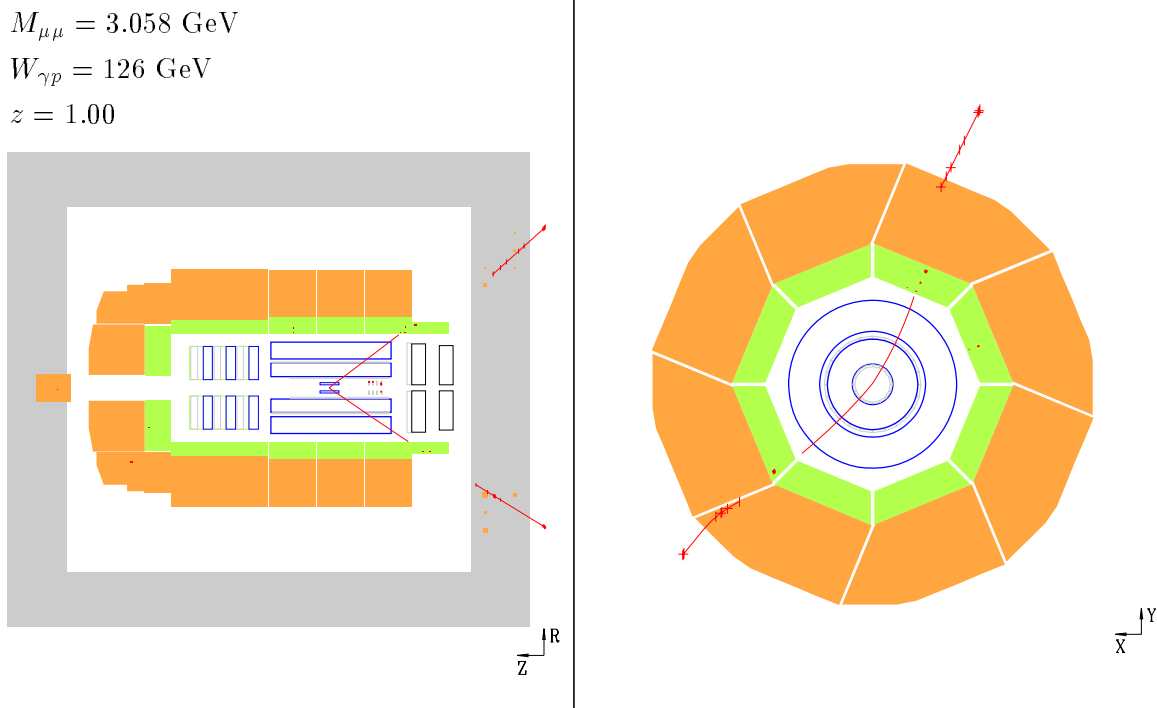


**Figure 4.2:** Schematic display of a candidate event for elastic  $J/\psi$  meson production. A side view of the H1 detector is shown at the left and a radial view of the central drift chambers and the LAr calorimeter at the right. Both muons were identified in the instrumented iron and no other particles were registered.

#### 4.1.1 Track Selection

The standard Lee West package from the heavy flavour working group has been used to resolve track ambiguities and to reject badly measured or unphysical tracks. Track ambiguities are due to the following reasons:

- Tracks are measured in the central or in the forward tracking chambers as described in chapter 1. Particles in the polar angle range  $10^\circ \lesssim \theta \lesssim 30^\circ$  will pass through both chambers. The resulting track segments are initially kept as up to three separate track hypotheses (forward, central, combined).
- Another source of ambiguities originates in the vertex fit, i.e. if one track can be fitted to more than one vertex within the resolution of the tracking chambers. In fact this is the case for more than one third of the (muon) tracks. In future it might be advisable to include more precise information from the CST to improve the vertex fit.

A list of track cuts can be found in appendix A. For a detailed documentation of the software package see [28].

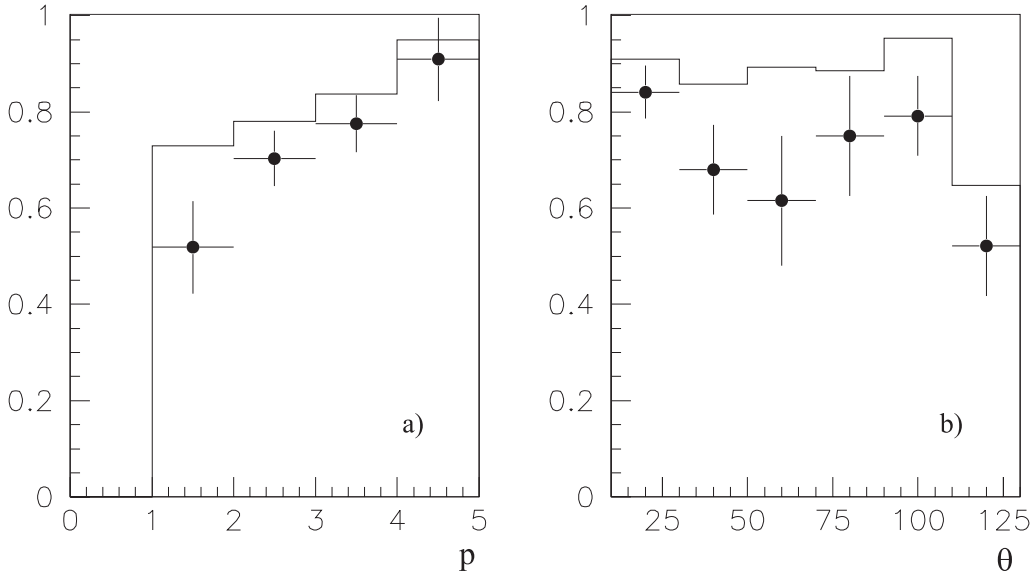


**Figure 4.3:** Lepton identification efficiency ( $Q_c \geq 2$ ) in data (full points) and Monte Carlo (histograms). a) as a function of  $p$  (integrated over  $10^\circ < \theta < 135^\circ$ ) and b) as a function of  $\theta$  (integrated over  $p > 2$  GeV).

### 4.1.2 Muon Identification

The decay leptons of the  $J/\psi$  can be identified by their typical signatures in the liquid argon calorimeter and the muon systems. An electron tends to deposit its energy only in the electromagnetic part of the calorimeter while a muon ( $p \gtrsim 800$  MeV) penetrates both parts of the calorimeter. In addition muons with sufficient momentum will be detected in the muon system. The identification of muons is thus more simple than it is for electrons. Secondly an efficient trigger for decay electrons was not available. These are the reasons for the exclusive use of the decay channel  $J/\Psi \rightarrow \mu^+ \mu^-$  in this analysis.

Three muon calorimeter quality classes  $Q_c = 1(\text{poor}), 2(\text{fair}), 3(\text{good})$  are defined. Typical (mis-)identification probabilities for muons are about 80% (5%). For a detailed description of the lepton identification at H1 see [29]. Again the standard Lee West package is used for the selection of muon candidates. For details refer to appendix B. Note that the default layer cut in the backward iron endcap (3 layers) has been increased to 6 layers.

In the final selection further cuts will be applied:

- At least one muon has to be identified in the muon system. The other muon must either be identified in the muon system or have calorimeter quality  $Q_c \geq 2$ .
- Each muon's momentum must be greater than 0.8 GeV
- Both muons must be contained in the polar angle region  $20^\circ < \theta < 160^\circ$ . The lowest  $z$  bin is treated differently:  $20^\circ < \theta < 140^\circ$  is required for both muons.

These cuts will be discussed in the following section.

Since the lepton identification efficiency will be related to the cross section as determined in chapter 5, one has to check the correct description of this quantity in Monte Carlo simulations.

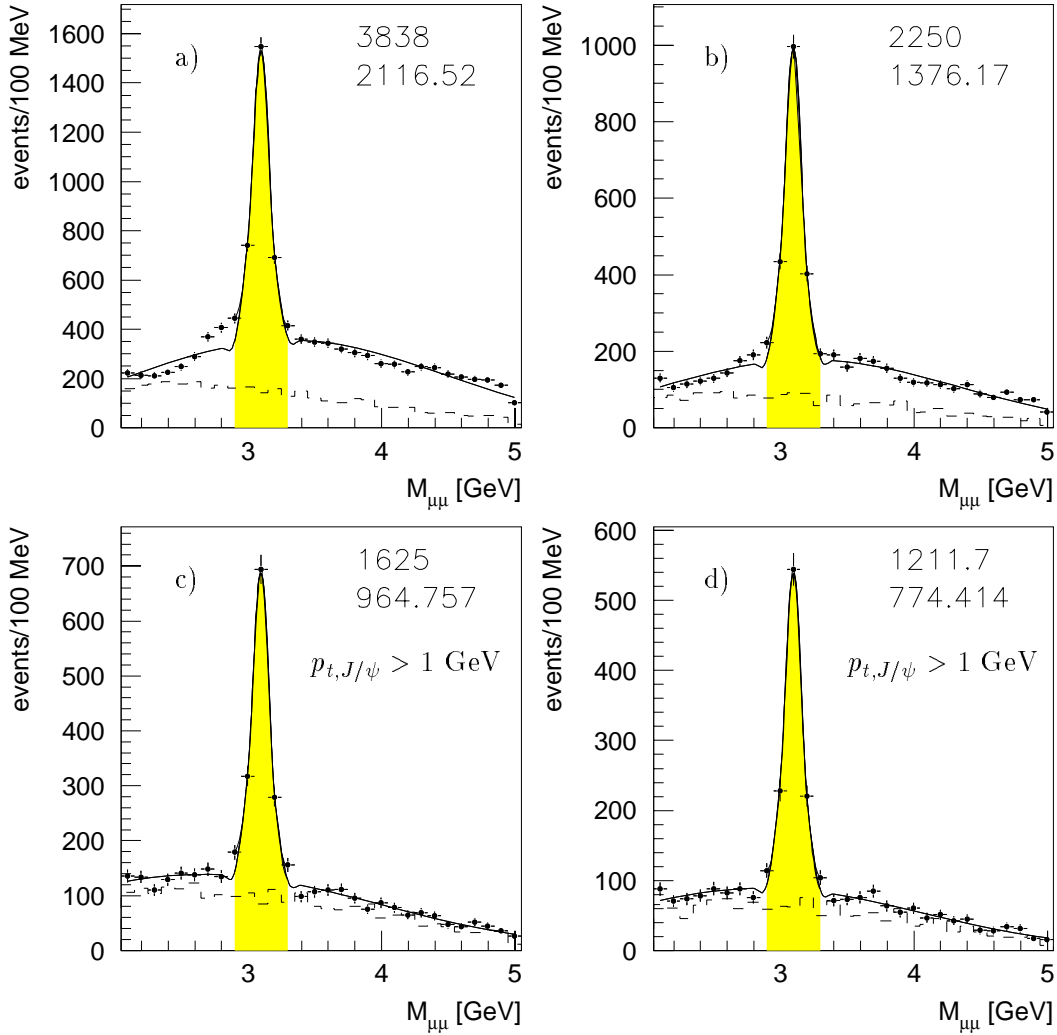


**Figure 4.4:** Invariant mass spectrum for photoproduction events a) before and b) after trigger selection. The spectrum after applying the cut  $p_{t,J/\psi} > 1$  GeV before and after trigger selection is shown in c) and d). The dashed lines show the spectrum of equally charged muon pairs. The numbers in the corner of each histogram represent the number of events in the  $J/\psi$  mass range (shaded) before and after background subtraction (see 5.1.1).

The identification efficiency in the calorimeter can be checked by looking at the calorimeter quality of muons which have been identified in the instrumented iron. A diffractive  $J/\psi \rightarrow \mu\mu$  sample with negligible background contributions is used for this check. As in many previous analyses it has been found that the muon identification efficiency in Monte Carlo is too high. Figure 4.3 shows the efficiency for muons of calorimeter class  $Q_c \geq 2$  as a function of momentum and polar angle. For simplicity a correction factor of 0.85 independent of  $\theta$  or  $p$  will be applied in all Monte Carlo simulations.

### 4.1.3 $J/\psi$ Candidates Selection

This analysis focuses on events in which  $J/\psi$  mesons are produced inelastically. In these events only a fraction of the scattered electron's energy loss is transferred to the  $J/\psi$  meson. This will typically result in low energy muon tracks and the remaining energy will often bring forth

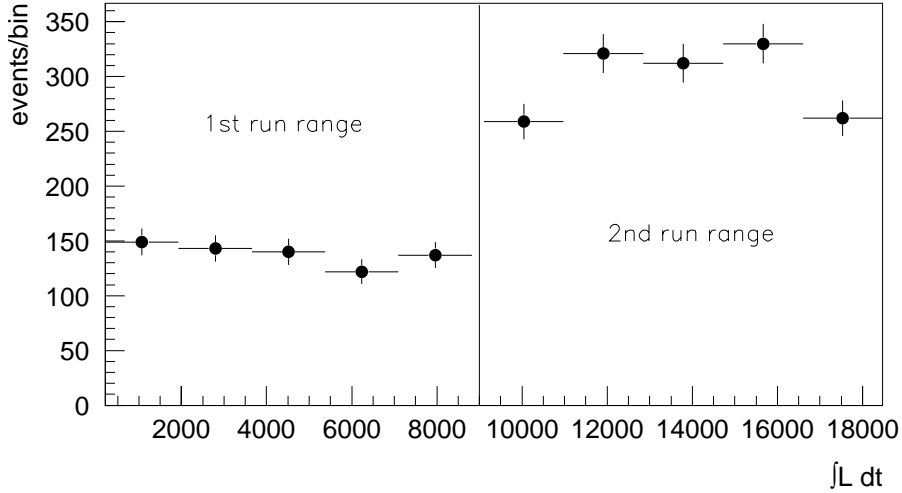


**Figure 4.5:** Number of  $J/\psi$  candidates per integrated luminosity. The increase starting with the beginning of the second run range is caused by a changing trigger selection.

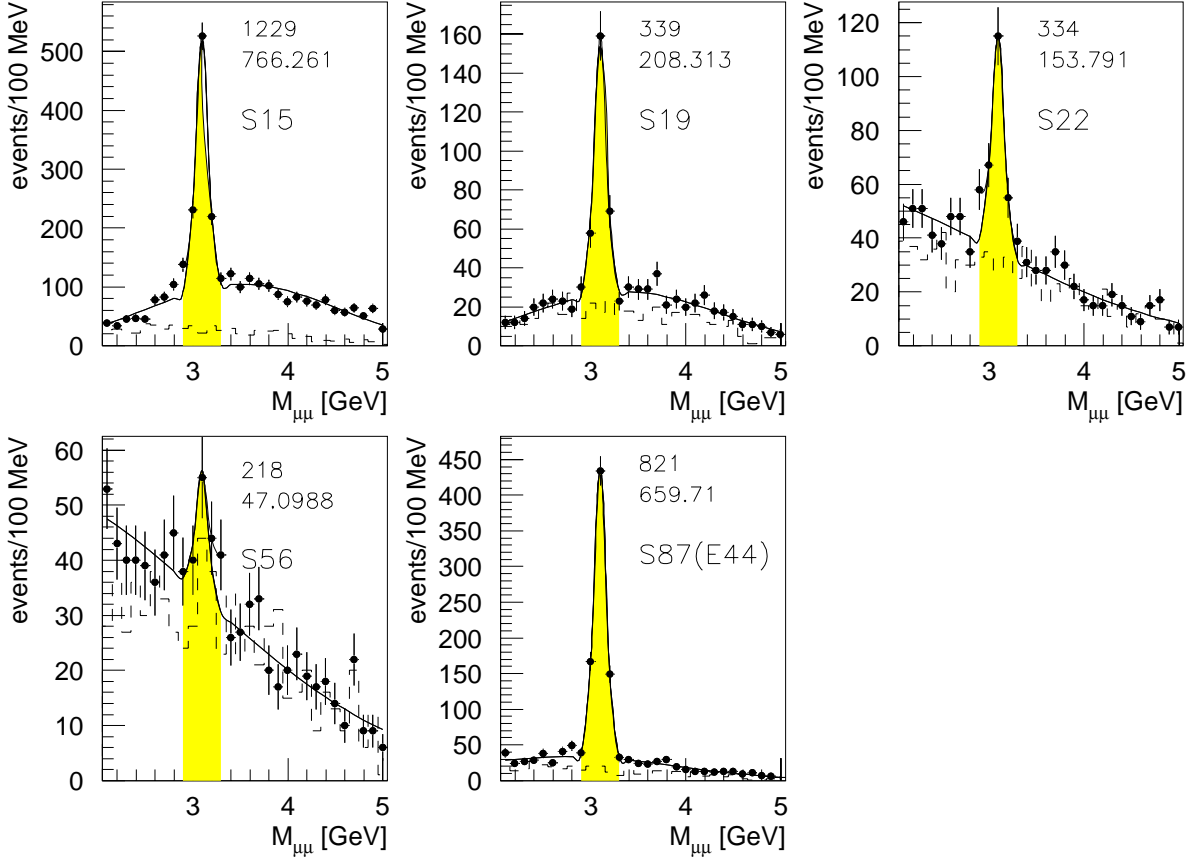
additional particles. Due to the non zero misidentification probability (for particles other than muons being misidentified as such) the number of background events is expected to be large. It is therefore the task to find further cuts on the muon variables which result in a low misidentification probability on the one hand and keep a good selection efficiency on the other hand. A cut on the transverse momentum of the muons (e.g.  $p_{t,\mu} > 1.4$  GeV) will suppress background at low invariant masses efficiently but it also distorts the background spectrum and may produce a fake signal around the  $J/\psi$  mass. A proper background subtraction becomes impossible in this case. Another strategy was adopted instead: In the lowest  $z$  bin  $\theta < 140^\circ$  (compared to  $\theta < 160^\circ$ ) is required for both muons. According to Monte Carlo simulation only  $\lesssim 5\%$  of the signal events are discarded when applying this cut. Background contributions in data are reduced by  $\gtrsim 50\%$ .

Figure 4.4 shows the invariant mass spectrum of all selected photoproduction events (electron class 0) before and after triggers are required. The dashed invariant mass spectrum of equally charged muon pairs is shown as a background estimate. Note that the background contributions are comparably large. In contrast to previous analyses [12] events with activity in the Spacal are only discarded if the scattered electron caused this activity (i.e. events with activity from the photon remnant are not discarded).

Finally the remaining events with an invariant mass  $\pm 250$  MeV around the  $J/\psi$  mass are taken as  $J/\psi$  candidates. The background subtraction is described in section 5.1.1. Figure 4.5 shows the number of selected  $J/\psi$  candidates per  $1.72 \text{ pb}^{-1}$  (2nd run range: per  $1.93 \text{ pb}^{-1}$ ) integrated luminosity. The number of events per integrated luminosity bin is stable within statistics. The increase starting with the beginning of the second run range is caused by the changing trigger selection.

## 4.2 Selection of Subtriggers

Unlike DIS events, which are triggered very efficiently by the energy deposit of the scattered electron in the backward calorimeter, photoproduction events will only be recorded whenever a potential muon was detected in the muon system (or if the electron was registered in one



**Figure 4.6:** Invariant mass spectrum for the relevant subtriggers: S15, S19, S22, S56 and S87. The numbers in the corner of each histogram represent the number of events in the  $J/\psi$  mass range (shaded) before and after background subtraction (see 5.1.1). Table 4.1 lists all cuts.

of the electron taggers). All triggers used in this analysis contain at least one muon trigger element. See table C.2 for a list of all relevant muon trigger elements and table C.1 for available subtriggers. It was the aim to select a stable, efficient and preferably small set of subtriggers.

In general it would be desirable to choose at least two independent subtriggers, i.e. subtriggers which do not contain a common trigger element. Then trigger efficiencies could be determined directly from the data. For example one could choose a Spacial trigger for the scattered electron (S0–S4) and compare these DIS events with events which were triggered by a muon subtrigger. However, due to limited statistics this method does not seem to be a practical solution. In this analysis the subtrigger efficiencies will be determined from Monte Carlo simulation instead. The efficiency of each trigger element will be compared in data and Monte Carlo whenever possible (see next section). Monte Carlo will be corrected if necessary.

Figure 4.6 shows the invariant mass spectra of all relevant subtriggers. The following combination of subtriggers has been chosen for the further analysis: S19, S22, S87(E44). In the second run range S19 and S22 are replaced by S15. The number of events which were triggered by S19 and S22 but not by S15 is negligible. The lowest  $z$  bin will be treated differently: S19 and S22 will be used in both run ranges since the total efficiency of S15 (L1 and L2) is less than the combined efficiency of S19 and S22. In addition S56 will be used. S56 is efficient only for

Subtriggers	$N$	$N_w$	Subtriggers	$N$	$N_w$
S15	232	270.2	S15, S19, S22	21	24.3
S19	249	310.0	S15, S19, S56	30	30.1
S22	187	232.4	S15, S19, S87	88	88.2
S56	66	66.1	S15, S22, S56	43	43.2
S87	385	385.9	S15, S22, S87	89	89.2
S15, S19	273	316.1	S15, S56, S87	0	0.0
S15, S22	215	250.0	S19, S22, S56	2	2.0
S15, S56	5	5.0	S19, S22, S87	5	5.0
S15, S87	53	53.1	S19, S56, S87	9	9.0
S19, S22	5	6.2	S22, S56, S87	6	6.0
S19, S56	28	28.0	S15, S19, S22, S56	4	4.0
S19, S87	112	122.25	S15, S19, S22, S87	2	2.0
S22, S56	28	28.0	S15, S19, S56, S87	2	2.0
S22, S87	89	89.2	S15, S22, S56, S87	6	6.0
S56, S87	10	10.0	S19, S22, S56, S87	0	0.0

**Table 4.3:** Number of  $J/\psi$  candidate events in the  $J/\psi$  mass range ( $\pm 250$  MeV around the  $J/\psi$  mass) per combination of subtriggers. The number of events  $N_w$  after applying the prescale weight  $w$  (see section 4.3) is shown in the right column. All cuts are listed in table 4.1.

resolved photon events. In fact photoproduction events triggered by S56 show only a  $J/\psi$  signal in the lowest  $z$  bin. Each event can be accepted by more than one subtrigger. The *overlap* of subtriggers can be seen in table 4.3.

Figures 4.7 and 4.8 show the subtrigger efficiencies as determined from photon gluon fusion (circles) and resolved photon (squares) Monte Carlo simulation. The efficiencies are shown as a function of  $z$  (left column),  $W_{\gamma p}$  (middle column) and  $p_{t,J/\psi}$  (right column). The diagrams labeled with *all* show the total trigger efficiency according to the trigger selection which was described in the previous paragraph. Note that the trigger efficiencies depend on the physics process.

### 4.2.1 Trigger Element Efficiencies

Roughly speaking the efficiency of a trigger element is defined to be the number of events firing the examined trigger element divided by the total number of events used for the efficiency determination. In order to achieve a reasonable efficiency one uses a selection of events which are potentially able to fire the examined trigger element. These events must not be triggered exclusively by a subtrigger which contains the examined trigger element. In the following sections the most relevant trigger elements will be examined. Data and Monte Carlo simulation will be compared.

#### Iron Trigger Elements

The trigger elements of the instrumented iron are listed in table C.2. The efficiency determination was based on events which have been triggered by Spacal (S0, S1) and e-tagger (S82...S86) subtriggers that do not contain an iron trigger element. Events with exactly one iron track have

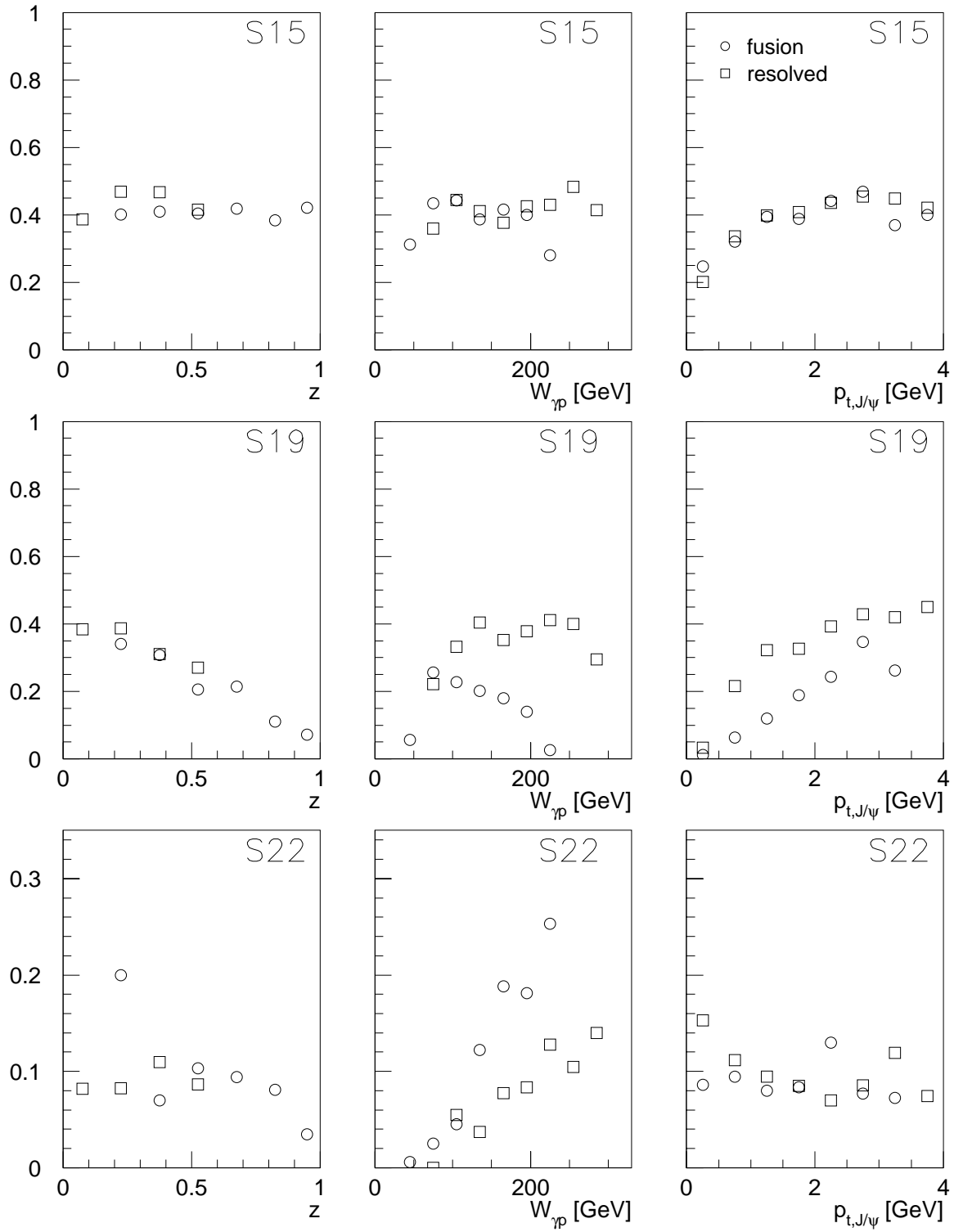


**Figure 4.7:** Subtrigger efficiencies as determined from photon gluon fusion (circles) and resolved photon (squares) Monte Carlo simulation as a function of  $z$  (left column),  $W_{\gamma p}$  (middle column) and  $p_{t, J/\psi}$  (right column). Part A (S15, S19, S22). Note the different scales in each row.

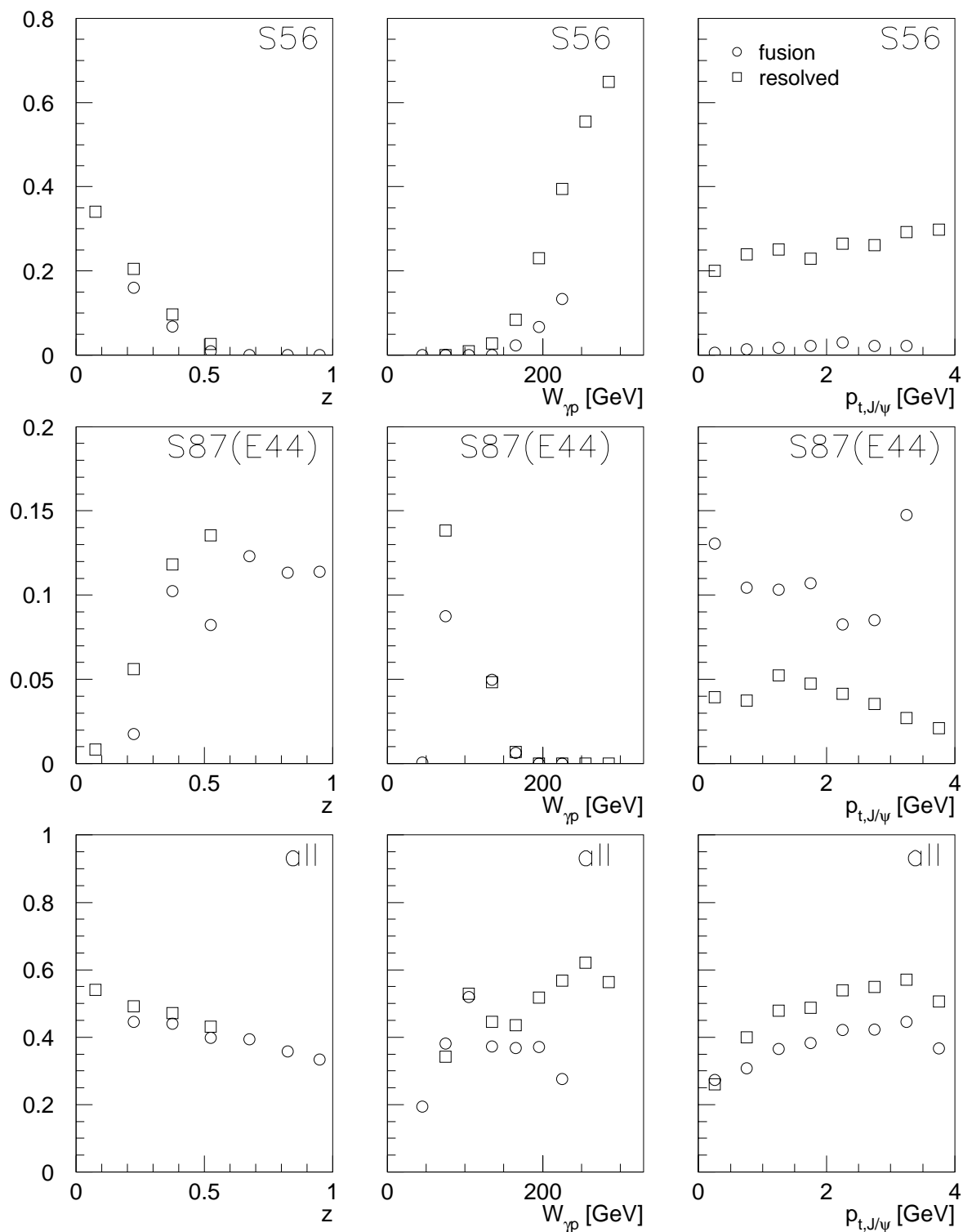


**Figure 4.8:** Subtrigger efficiencies as determined from photon gluon fusion (circles) and resolved photon (squares) Monte Carlo simulation as a function of  $z$  (left column),  $W_{\gamma p}$  (middle column) and  $p_{t,J/\psi}$  (right column). Part B (S56,S87,all). Note the different scales in each row.

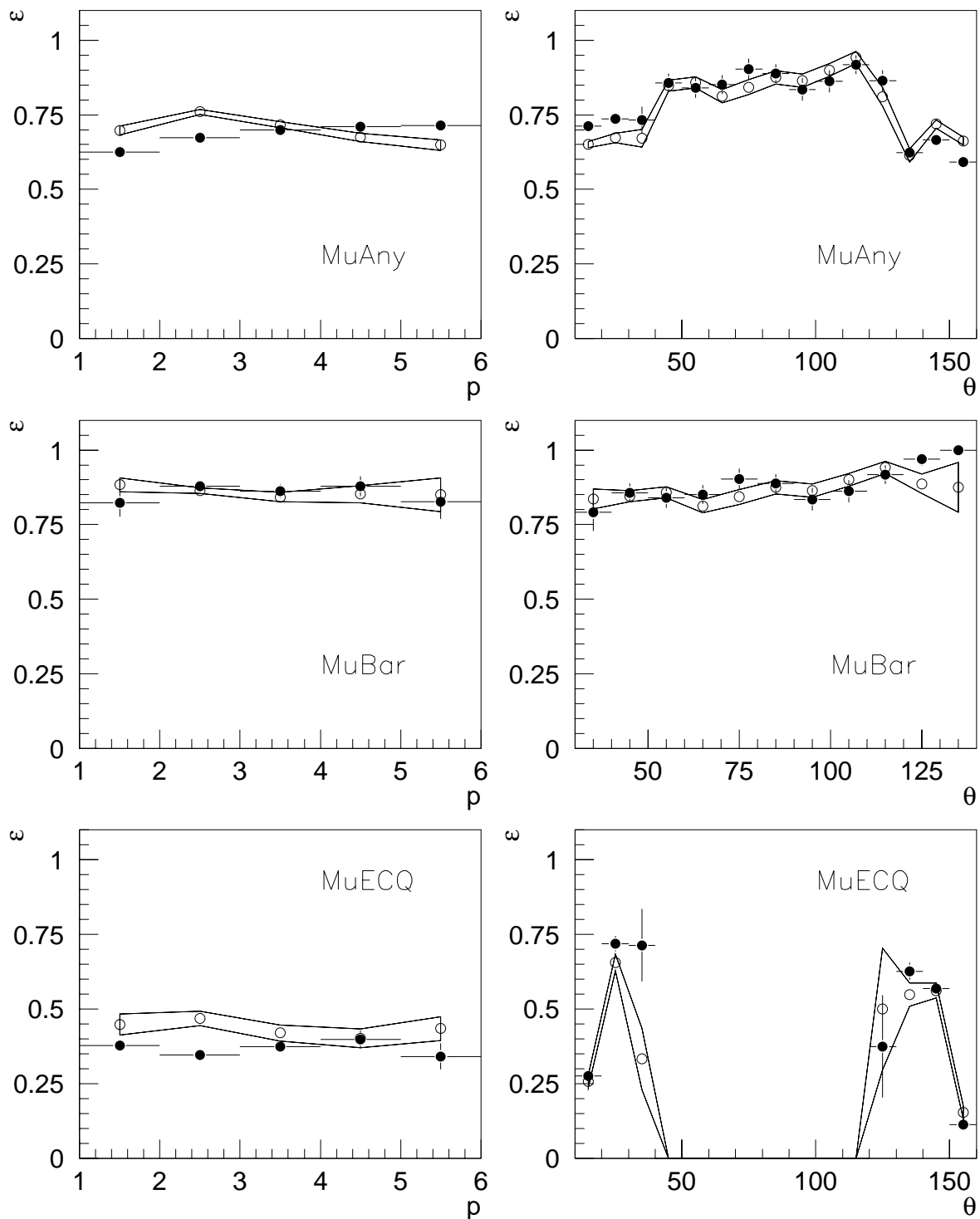


**Figure 4.9:** Efficiencies of the instrumented iron's trigger elements in data (full points) and Monte Carlo simulation (open points) as a function of the muon's momentum  $p$  and polar angle  $\theta$ . The statistical error of the Monte Carlo efficiency is shown as a band.

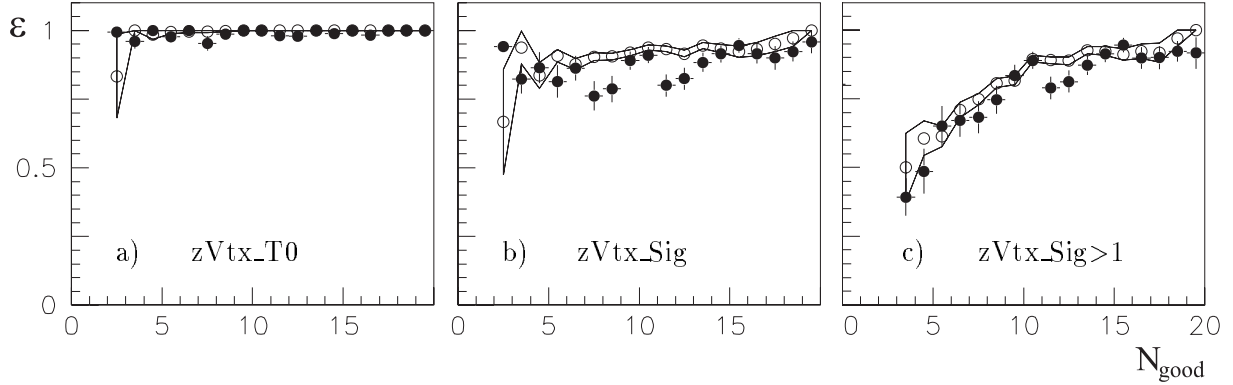


**Figure 4.10:** Efficiency of the  $z$  Vertex histogram trigger elements a)  $zVtx\_T0$  b)  $zVtx\_Sig$  and c)  $zVtx\_Sig>1$  as a function of the number of good tracks in data (full points) and Monte Carlo (open points) before correction. The statistical error of the Monte Carlo efficiency is shown as a band.

been selected. See figure 4.9 for a comparison of the efficiency as a function of the muon's polar angle and momentum in data and Monte Carlo simulation. A preliminary version of the iron trigger simulation has been used. One observes good agreement in data and Monte Carlo simulation.

### $z$ -Vertex histogram

The relevant trigger elements for the  $z$ -Vertex trigger are listed in table C.4. The efficiency determination was based on events which have been triggered by Spacal subtrigger S56. Subtrigger S56 does not contain a vertex histogram trigger element. The trigger element  $zVtx\_Sig>1$  ( $zVtx\_Sig$ ) has been determined to be 6% (9%) more efficient in Monte Carlo simulation than in data. The Monte Carlo will be corrected by the given factors accordingly. See figure 4.10 for a comparison of the efficiency as a function of the number of good tracks in data and Monte Carlo simulation. Note that the trigger element  $zVtx\_Sig^1$  has only been introduced in 1997.

### E-Taggers

The electron taggers are efficient for events with  $Q^2 < 0.01 \text{ GeV}^2$  only. Furthermore the acceptance is a function of  $y$ . Figure 4.11 shows the acceptance function of E33 and E44. The procedure for the determination of the acceptance function is described in [31]. Due to frequently changing beam conditions during the data taking period it is not possible to simulate the exact electron tagger response within the framework of the H1 detector simulation package. When comparing data with Monte Carlo simulation each event will obtain a  $y$  and run number dependent weight instead. This procedure is described in [32]. To reject background events from Bethe-Heitler processes it is furthermore required that  $E_{PD} < 1 \text{ GeV}$  and  $E_{33} > 2 \text{ GeV}$  ( $E_{44} > 6 \text{ GeV}$ ).

<sup>1</sup> $zVtx\_Sig$  is the CTL name. The new trigger element is also called  $sig\_Mu\_D$ .

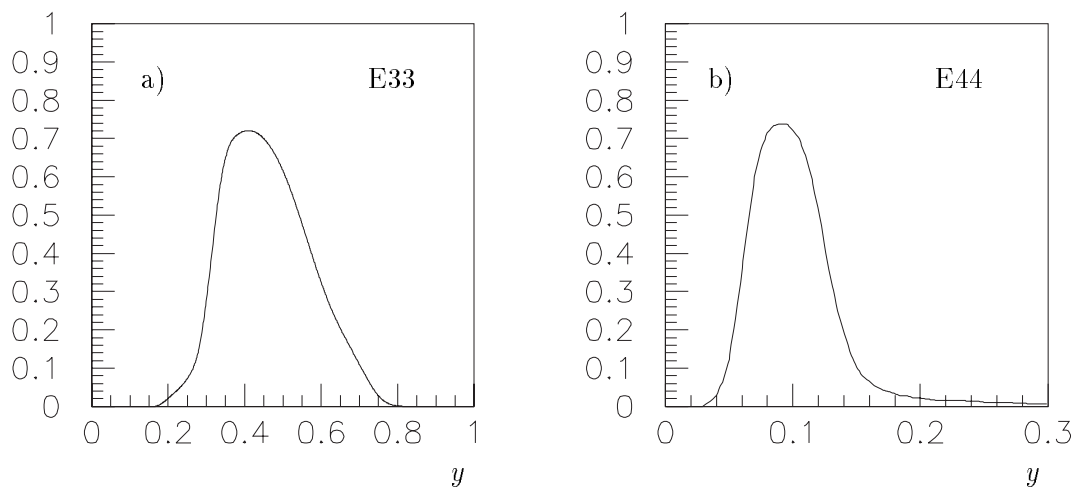


**Figure 4.11:** Acceptance function of the electron taggers during one run range. a) E33, b) E44.

#### 4.2.2 Neural Network Trigger for Muons

During the second run period (see table 4.2) a neural network L2 trigger verified L1 subtrigger S15. Without the second level verification S15 would have been heavily prescaled. The neural network uses tracking, iron and calorimeter information for its decision. For a detailed description see [33, 34]. The definition of S15 is very similar to S19 for the barrel region and S22 for the endcap region except that each condition is softer (see Appendix C.1). The L2 efficiency can therefore be estimated when using events which have been triggered by subtrigger S19 or S22. Roughly speaking the efficiency is the number of events which were triggered by S15 on both trigger levels divided by the number of events which were accepted by S19 or S22. The L2 neural network hardware can also be simulated by a software routine. Data and Monte Carlo are in good agreement. The L2 trigger efficiency was determined to be  $83.5 \pm 2\%$  in both cases. Figure 4.12 shows the trigger efficiency as a function of  $z$ . Data and Monte Carlo are in agreement within statistics. A mixed photon gluon fusion and resolved photon Monte Carlo has been used.

#### 4.2.3 L4 Efficiency

During the data taking period of 1997 additional cuts were applied on trigger level L4. For the muon subtriggers S15, S19, S22 and S56 the existence of a reconstructed muon track was required and for trigger S19 the muon track was required to be in the barrel part of the instrumented iron and a loose matching between iron tracks and central tracks was required. The matching algorithm applied on trigger level 4 is not identical to the linking algorithm used for the final event reconstruction [35]. The fourth trigger level is not simulated in Monte Carlo. However the efficiency can be determined from data by selecting events from Spacal and eTag subtriggers which do not contain a muon condition on L4. The L4 efficiency of all subtriggers used in the present analysis was determined to be close to 100%, except for S19 ( $\sim 83\%$ ). As a consequence the efficiency of subtrigger S19 will be corrected accordingly in Monte Carlo simulations. To keep trigger inefficiencies as small as possible the analysis cuts have been chosen rather hard: At least one linked muon was required for all triggers. For S19 (S22) the linked muon was required to be in the barrel (endcap) part of the instrumented iron.

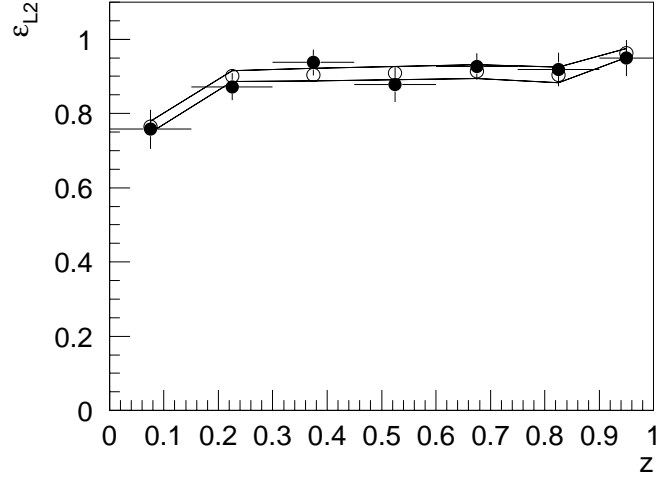


**Figure 4.12:** The L2 neural network efficiency in data (full points) and mixed Monte Carlo (open points). The statistical error of the Monte Carlo efficiency is shown as a band.

### 4.3 Prescaling

Some of the relevant muon subtriggers had been prescaled during the data taking period 1997. Table C.1 shows the average prescale factor of each subtrigger. The effect of prescaling has been reversed by assigning the weight  $w_j$  to each data event.

If one denotes by

$$r_{ij} = \begin{cases} 1 & : \text{ if raw subtrigger } i \text{ is set in event } j \\ 0 & : \text{ otherwise} \end{cases} \quad (4.1)$$

and  $d_{ik}$  is the prescaling factor of subtrigger  $i$  in run  $k$  with luminosity  $\mathcal{L}_k$  then

$$w_j = \frac{\sum_{k=1}^{N_{runs}} \mathcal{L}_k}{\sum_{k=1}^{N_{runs}} \mathcal{L}_k P_{jk}}, \text{ where} \quad (4.2)$$

$$P_{jk} = 1 - \prod_{i=1}^{N_{subtr}} \left( 1 - \frac{r_{ij}}{d_{ik}} \right) \quad (4.3)$$

$P_{jk}$  designates the probability that at least one of  $N_{subtr}$  subtriggers triggers the event  $j$  in run  $k$ . A detailed discussion of the described method can be found in [36]. The effect of prescaling can be seen in table 4.3. The effective weight for an event that is triggered by a given subtrigger (and maybe other subtriggers) is shown in table 4.4. The effect of prescaling is  $\sim 13\%$  for subtriggers S15, S19 and S22. It is negligible for the other subtriggers.

### 4.4 Comparing Data and Monte Carlo

In this section more Monte Carlo quantities will be compared to data. All cuts are listed in table 4.1. The histograms shown in the following subsections are organized in the following way:

Subtrigger	effective weight $w$
S15	1.130
S19	1.134
S22	1.128
S56	1.002
S87	1.002

**Table 4.4:** The effective weight  $w = N_w/N$  for events triggered by a given subtrigger.  $N$  ( $N_w$ ) is the unweighted (weighted) number of events triggered by a given subtrigger (and maybe others).

Full dots represent background corrected data distributions. Open dots represent distributions without background subtraction. The total invariant mass signals for different  $z$  ranges which will be compared to Monte Carlo simulation are shown in figure 4.13. Only events in the  $J/\psi$  mass range have been selected. Due to poor statistics it is not always possible to determine the background fraction by fitting background and signal as described in section 5.1.1. The background will be estimated as follows for this comparison: It is assumed that muon pairs with equal charge can describe the background. For the kinematic region  $p_{t,J/\psi} > 1$  GeV this assumption seems to be justifiable. The number of like-sign muon pairs outside the mass peak is approximately equal to the number of unlike-sign pairs (see figure 4.13). A corresponding distribution of muon pairs with *equal* charge in the  $J/\psi$  invariant mass range will be subtracted per bin in each histogram. Monte Carlo distributions are drawn as a line and are normalized to the number of background corrected data events. The following quantities are shown in each figure:

- a)  $\theta_{J/\psi}$ , polar angle of the  $J/\psi$
- b)  $y_{rap,J/\psi}$  rapidity of the  $J/\psi$
- c) squared transverse momentum  $p_{t,J/\psi}$  of the  $J/\psi$
- d) center of mass energy in the  $\gamma p$  rest frame  $W_{\gamma p}$
- e)  $J/\psi$  contribution  $y_{J/\psi}$  to the reconstruction of  $y_{jb}$
- f) number of additional tracks (besides the two muons)
- g) polar angle  $\theta_{hi}$  of the muon of highest momentum
- h) polar angle  $\theta_{lo}$  of the muon of lowest momentum
- i) difference  $\Delta\theta$  of polar angles of the muons
- j) difference  $\Delta\phi$  of azimuthal angles of the muons
- k) azimuthal angle  $\phi$  of the muons
- l) energy deposition  $E_{forward}$  for  $\theta < 20^\circ$  in the LAr calorimeter
- m) momentum  $p_{hi}$  of the muon of highest energy
- n) momentum  $p_{lo}$  of the muon of lowest energy

- o) pseudo rapidity distribution  $\eta_{spacal}$  of the Spacal cell energies
- p) total energy deposition in the electromagnetic Spacal  $E_{em,spa}$
- q) total energy deposition in the hadronic Spacal  $E_{had,spa}$
- r) electromagnetic Spacal topology  $s_{topo}$  (see below)

The *electromagnetic Spacal topology*  $s_{topo}$  shown in r) was designed to identify the photon remnant in the Spacal. The photon remnant typically shows widely spread energy depositions in the electromagnetic Spacal. In contrast, the energy deposition observed in photon gluon fusion or diffractive events is often concentrated in a few close by calorimeter cells.  $s_{topo}$  is calculated as follows:

$$s_{topo} = \sum_{i=1}^{N_{cells}} E_{cell} \cdot \sqrt{(x_{cell} - x_{cog})^2 + (y_{cell} - y_{cog})^2} \quad (4.4)$$

$$x_{cog} = \sum_{i=1}^{N_{cells}} \frac{E_{cell} \cdot x_{cell}}{E_{tot}} \quad (4.5)$$

$$y_{cog} = \sum_{i=1}^{N_{cells}} \frac{E_{cell} \cdot y_{cell}}{E_{tot}} \quad (4.6)$$

$$E_{tot} = \sum_{i=1}^{N_{cells}} E_{cell} \quad (4.7)$$

The sums extend over all electromagnetic Spacal cells. In other words  $s_{topo}$  is the energy weighted sum over the distances of all cells to the center of gravity (cog) of the energy deposition.

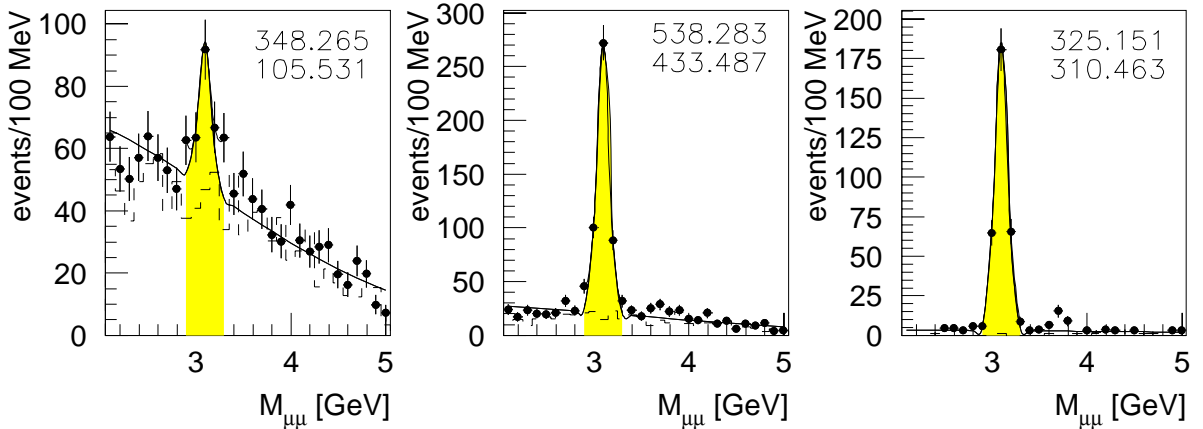


**Figure 4.13:** Invariant mass signal for a)  $z < 0.3$ , b)  $0.3 < z < 0.9$ , and c)  $0.9 < z < 1$ . The background spectrum of muon pairs with equal charge is shown as dashed lines. The numbers at the top of each histogram represent the number of events in the  $J/\psi$  mass range (shaded) before and after background subtraction (see section 5.1.1). All cuts are list in table 4.1.

## Resolved Photon Processes

Events with  $z < 0.3$  are compared to a resolved photon Monte Carlo in figures 4.14 and 4.15. Some histograms suffer from low statistics but are shown to complete the picture. Data and Monte Carlo simulation agree within statistics. The agreement of the distributions which are sensitive to the photon remnant in the backward detector region is good: pseudorapidity distribution of the Spacal cells in histogram *o*), the Spacal topology in histogram *r*) and the total energy in the electromagnetic and hadronic Spacal in histograms *p*) and *q*). The pseudorapidity distribution  $\eta_{spacal}$  and the Spacal topology  $s_{topo}$  show an excess at small values. This is typical for photon gluon fusion events (compare to the corresponding diagrams in figure 4.17) and indicates that this process still contributes at  $z < 0.3$ .

## Photon Gluon Fusion

Events with  $0.3 < z < 0.9$  are compared to a photon gluon fusion Monte Carlo in figure 4.16 and 4.17. Most distributions are described well by the Monte Carlo simulation. The selected data events have a slightly higher track multiplicity than expected by Monte Carlo simulation (histogram *f*). The  $p_{t,J/\psi}$  distribution (histogram *c*) is slightly flatter in data. The mismatch of the  $\Delta\phi$  distribution (histogram *j*) is closely related to the mismatch in the  $p_{t,J/\psi}$  distribution: A back to back topology of the decay muons in the  $r\phi$  plane corresponds to low transverse  $J/\psi$  momenta.

## Diffraction Processes

Events with  $z > 0.9$  are compared to proton dissociative diffractive Monte Carlo in figures 4.18 and 4.19. Again data and Monte Carlo show agreement in most distributions. As before the data events have a slightly higher track multiplicity than expected by Monte Carlo simulation (histogram *f*). The  $p_{t,J/\psi}$  (histogram *c*),  $\Delta\phi$  (histogram *j*) and  $E_{forward}$  (histogram *l*) data distributions show features which are typical for photon gluon fusion indicating that this process still contributes at  $z > 0.9$ . The  $p_{t,J/\psi}$  distribution is much steeper in Monte Carlo simulation than in data which is again related to the mismatch in  $\Delta\phi$ . Furthermore the distribution of the LAr energy in forward direction in histogram *l*) is steeper in data than in the proton dissociative Monte Carlo simulation.

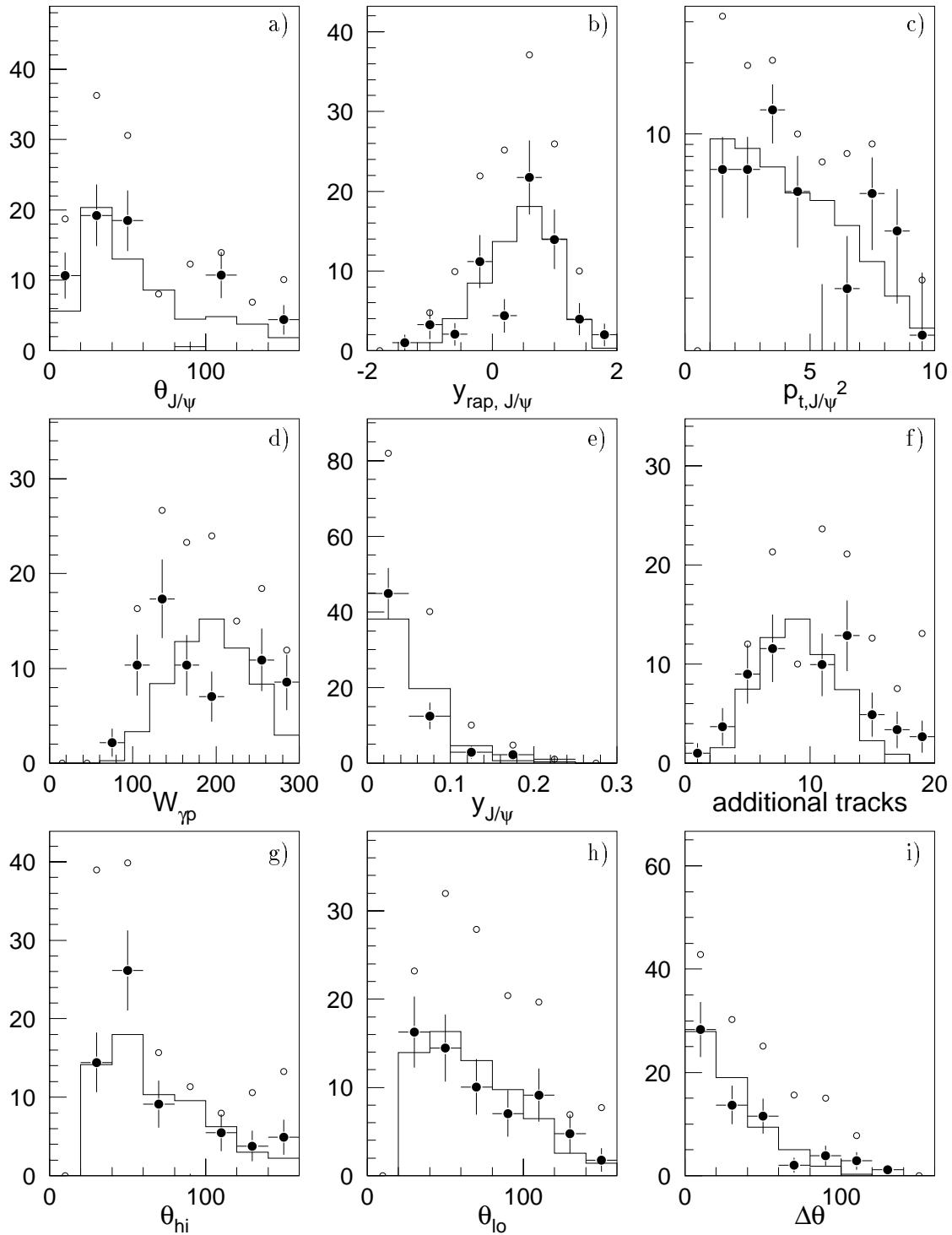


**Figure 4.14:** Comparison of data ( $z < 0.3$ ) and **resolved photon** Monte Carlo simulation. Part A. The histograms are described in section 4.4. Full (open) dots show background corrected (uncorrected) data. All cuts are listed in table 4.1.

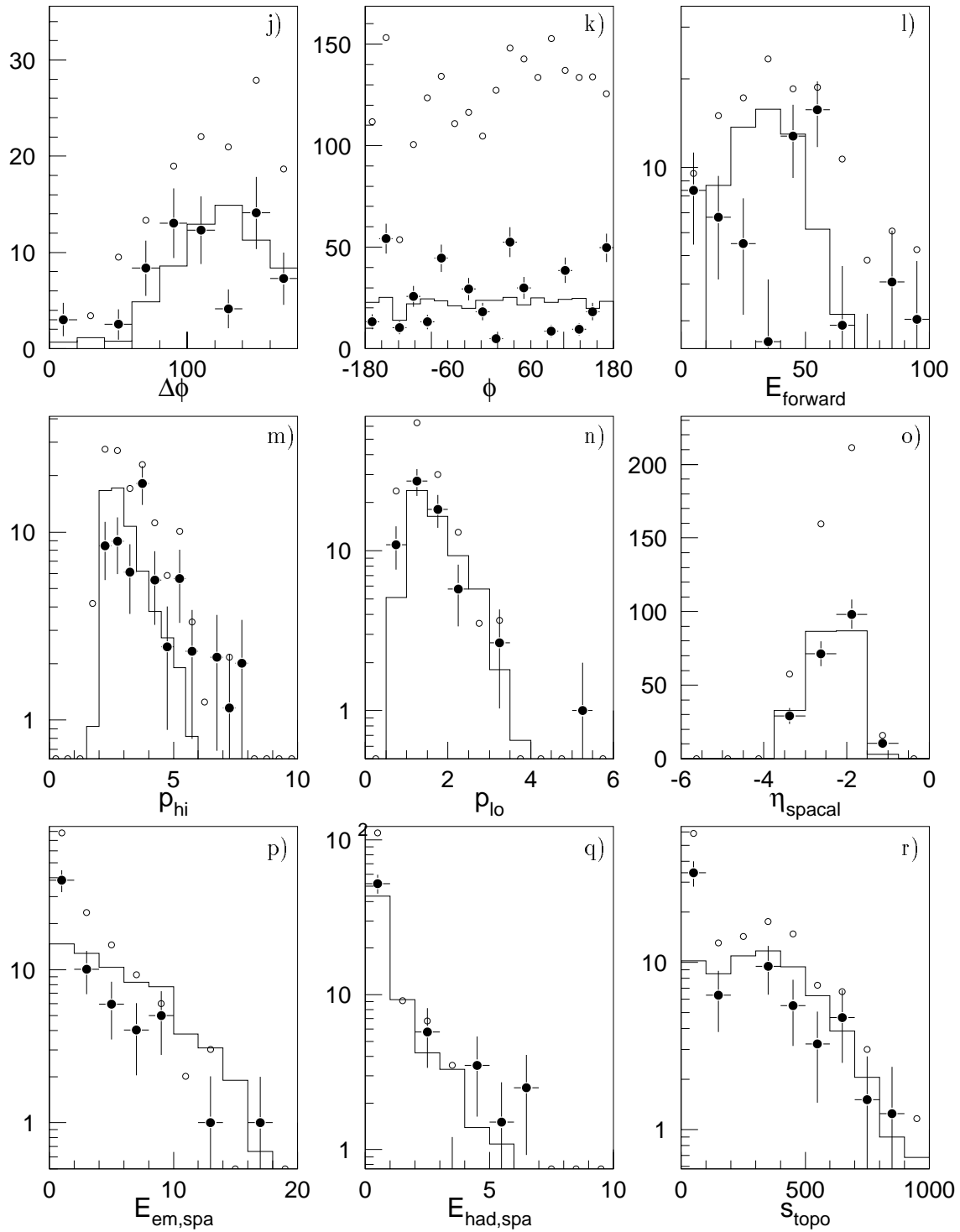


**Figure 4.15:** Comparison of data ( $z < 0.3$ ) and resolved photon Monte Carlo simulation. Part B. The histograms are described in section 4.4. Full (open) dots show background corrected (uncorrected) data. All cuts are listed in table 4.1.

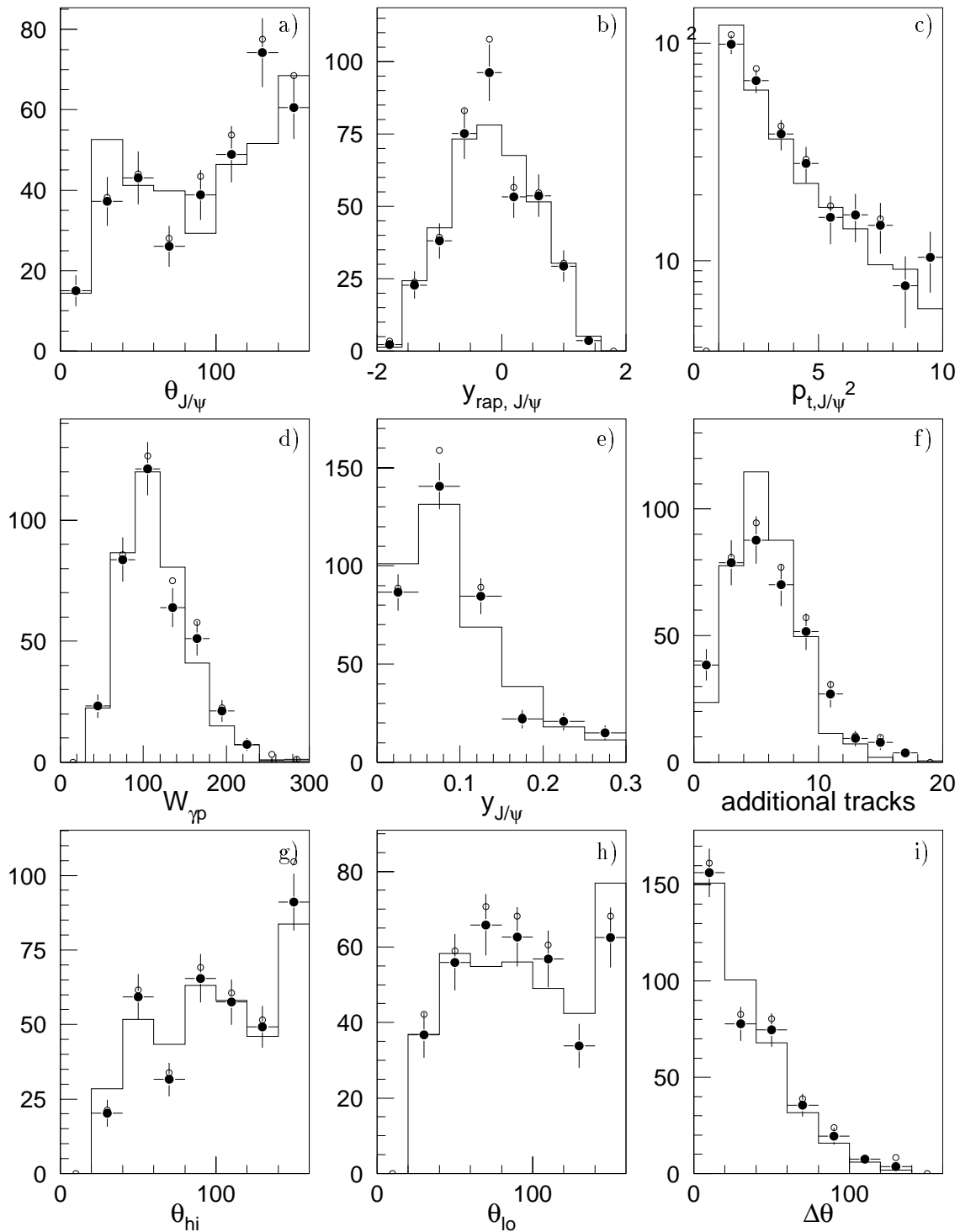


**Figure 4.16:** Comparison of data ( $0.3 < z < 0.9$ ) and **photon gluon fusion** Monte Carlo simulation. Part A. The histograms are described in section 4.4. Full (open) dots show background corrected (uncorrected) data. All cuts are listed in table 4.1.

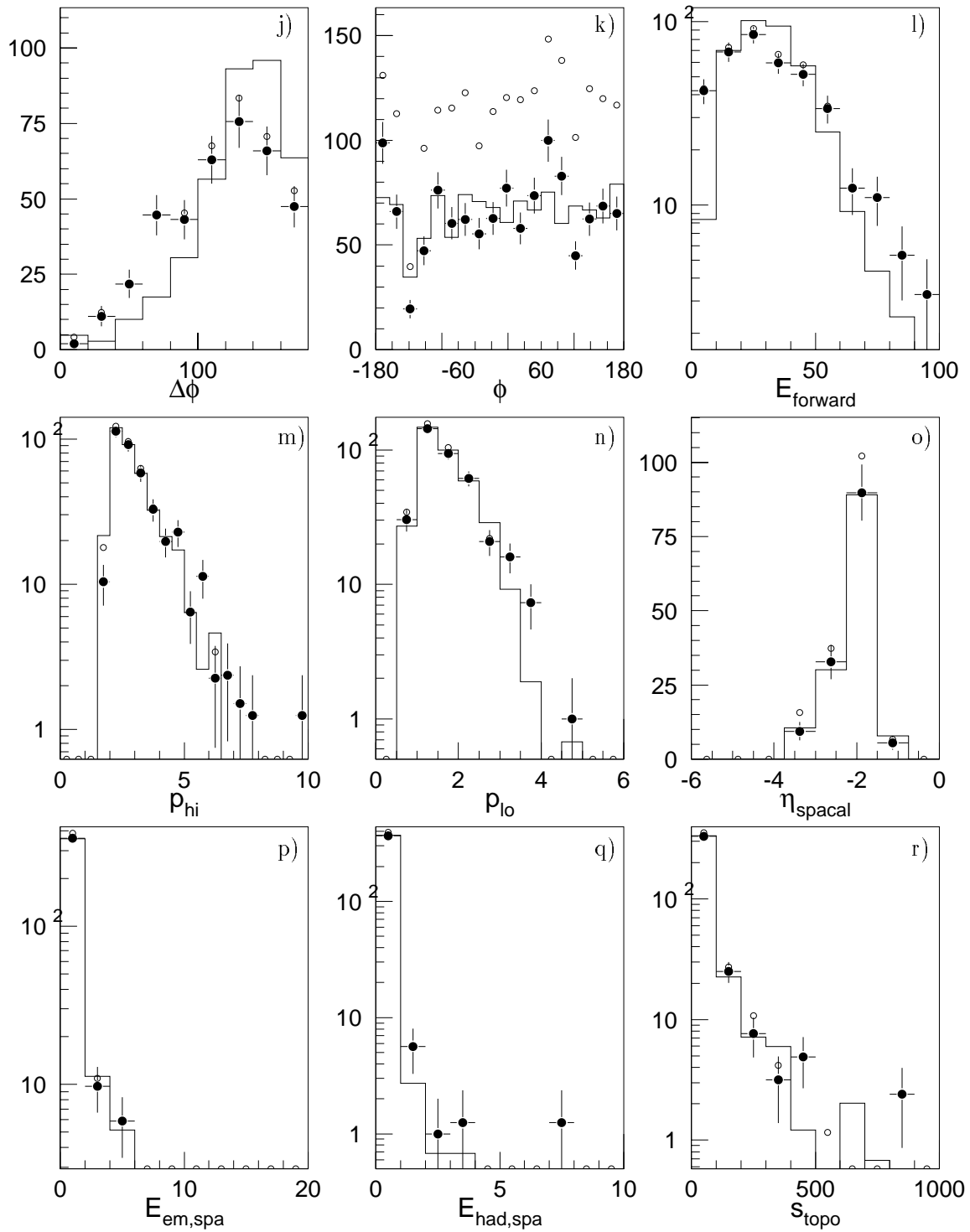


**Figure 4.17:** Comparison of data ( $0.3 < z < 0.9$ ) and **photon gluon fusion** Monte Carlo simulation. Part B. The histograms are described in section 4.4. Full (open) dots show background corrected (uncorrected) data. All cuts are listed in table 4.1.

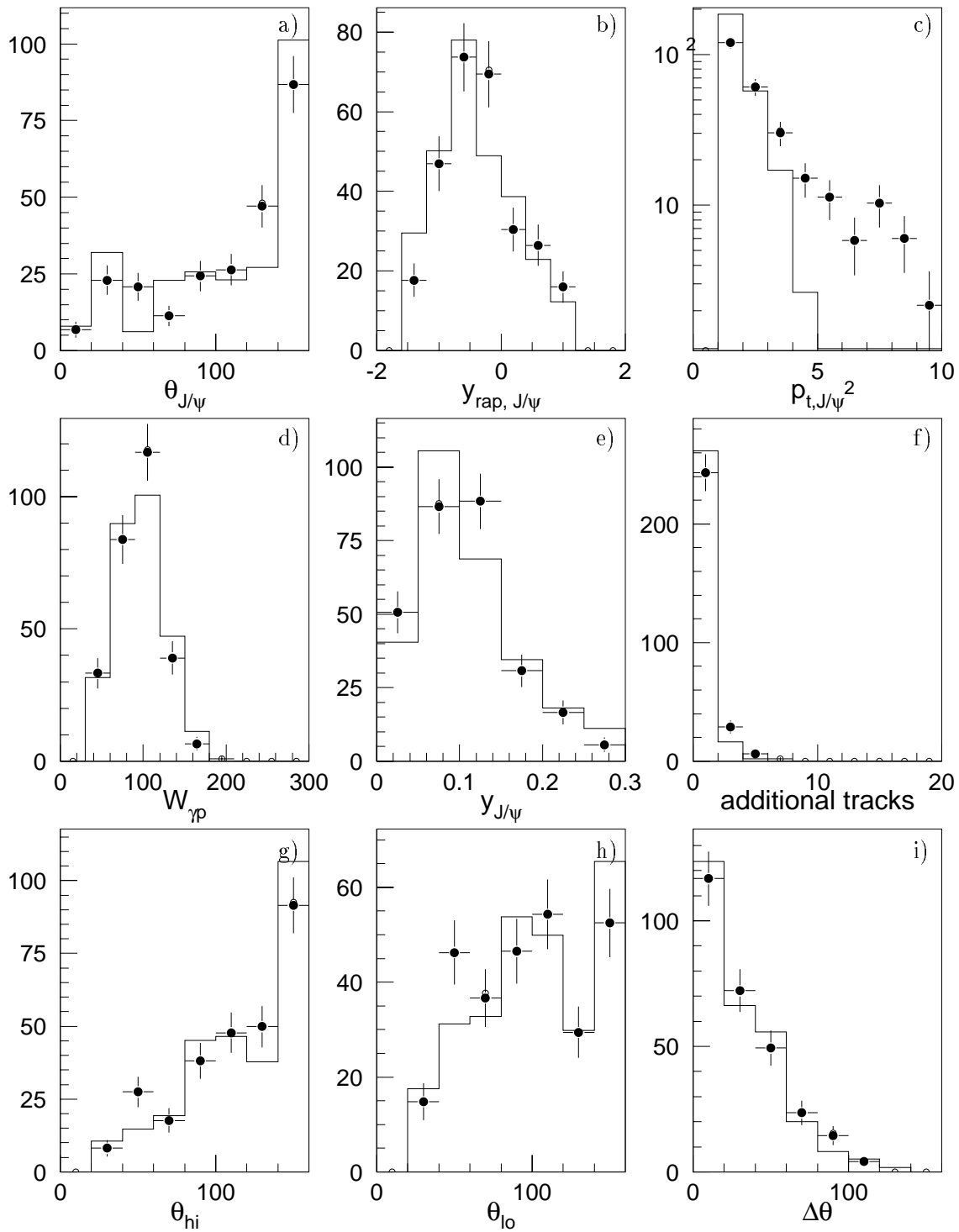


**Figure 4.18:** Comparison of data ( $z > 0.9$ ) and **diffractive proton dissociative** Monte Carlo simulation. Part A. The histograms are described in section 4.4. Full (open) dots show background corrected (uncorrected) data. All cuts are listed in table 4.1.

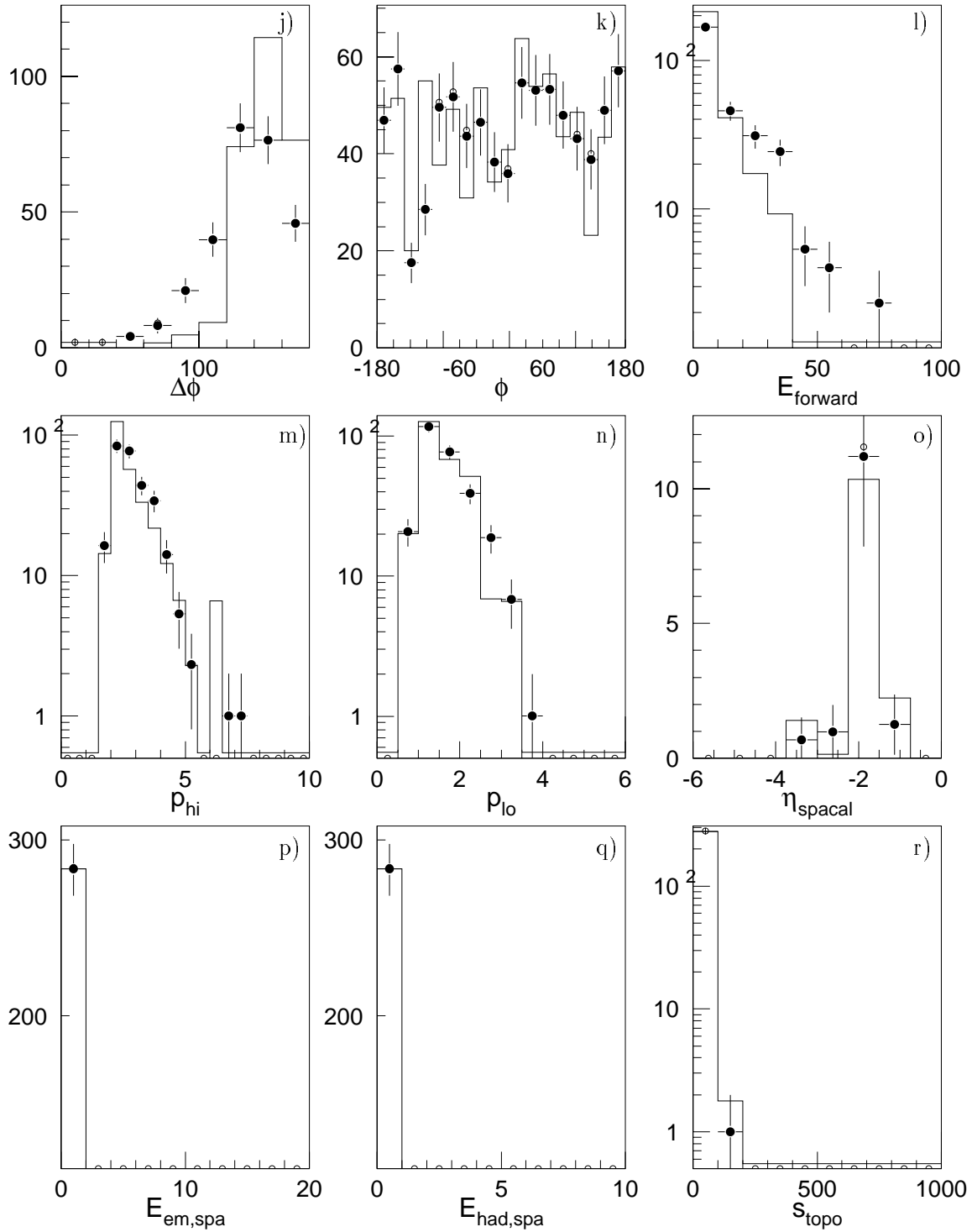


**Figure 4.19:** Comparison of data ( $z > 0.9$ ) and **diffractive proton dissociative** Monte Carlo simulation. Part B. The histograms are described in section 4.4. Full (open) dots show background corrected (uncorrected) data. All cuts are listed in table 4.1.

## 4.5 Mixing of Monte Carlo Simulations

Because of the lack of a Monte Carlo simulation which models all production processes it is the aim to find a mixed Monte Carlo data set which is able to describe the data in all kinematical regions. The variable which discriminates best between different production processes is the  $J/\psi$  meson's inelasticity  $z$ . At low  $z$  resolved photon processes dominate. At high  $z$  diffractive processes dominate. At intermediate  $z$  photon gluon fusion is the dominant process. Since good agreement of most Monte Carlo and data distributions is observed within statistical errors in all kinematic ranges the Monte Carlo simulations of different processes will be mixed: The photon gluon fusion Monte Carlo will be scaled in such a way that it describes data best in the intermediate  $z$  range. The lack of events at high  $z$  will then be filled with diffractive events. 40% of all diffractive Monte Carlo events are chosen to be proton dissociative<sup>2</sup> (see [37]). The lack of events at low  $z$  will be filled with resolved photon events. The ratio of the number of photon gluon fusion events to the number of resolved or diffractive events (after applying all cuts, see table 4.1) obtained in this way is:  $f_{resolved} = 16.0$  and  $f_{diffractive} = 0.85$ . The result of this procedure is shown in figure 4.20. As expected the  $z$  distribution is described well by the mixed Monte Carlo simulation. The  $W_{\gamma p}$  distribution agrees within statistics as well. The  $p_{t,J/\psi}$  distribution is flatter in data than in the mixed Monte Carlo simulation. More data distributions are compared to the mixed Monte Carlo simulation in figures 4.21 and 4.22 in the style of the previous section. The overall agreement is good. All efficiencies for the determination of cross sections will now be determined from this mixture of Monte Carlo simulations.

---

<sup>2</sup>After applying the cut  $p_{t,J/\psi} > 1$  GeV most of the elastic events are lost again.

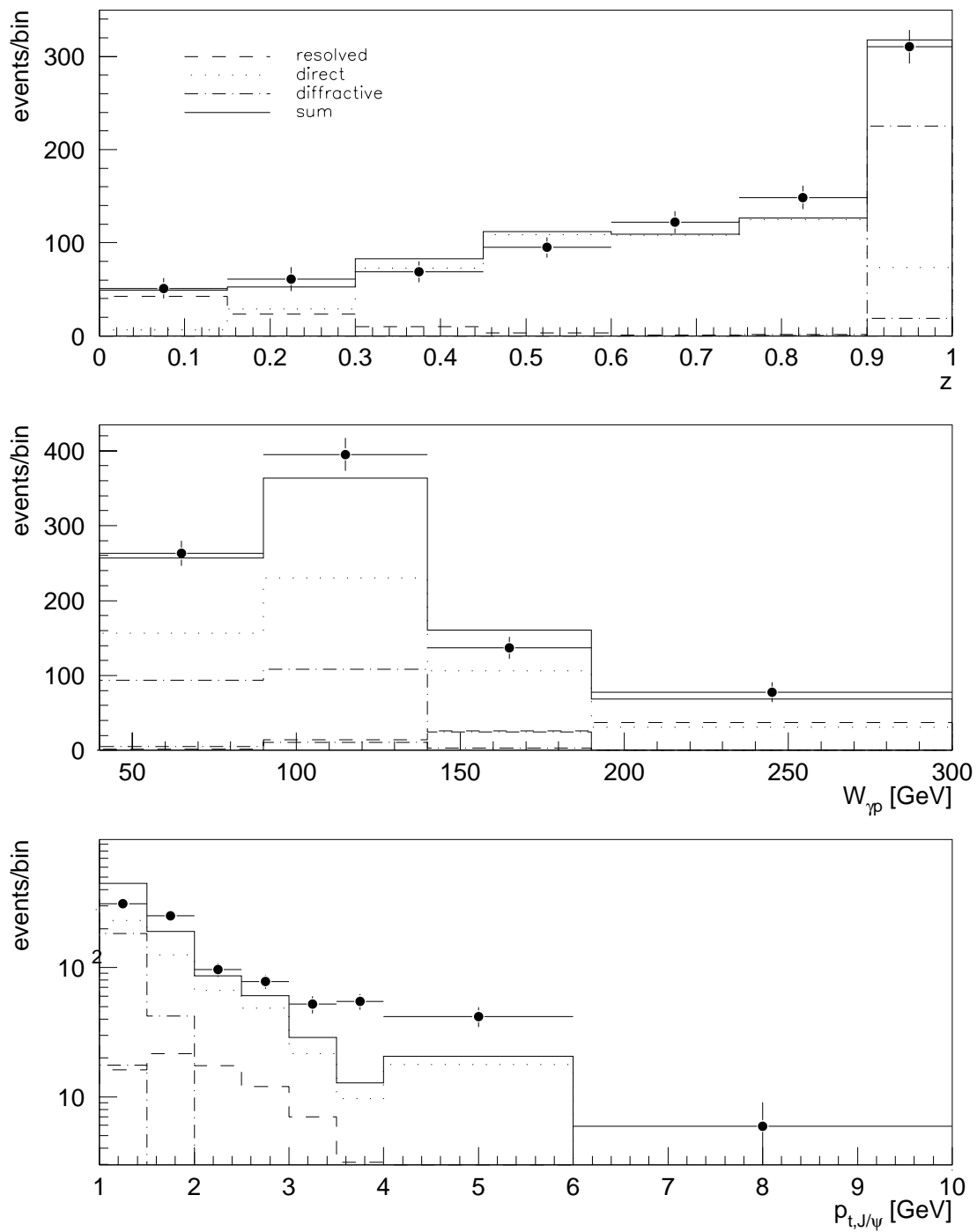


**Figure 4.20:** Expected number of events from photon gluon fusion (dotted line), resolved photon (dashed line), diffractive processes (dash dotted lines) and the sum of all processes (solid line) as a function of the reconstructed  $z$ ,  $W_{\gamma p}$  and  $p_{t,J/\psi}$  compared to background corrected data (full points). The Monte Carlo cross sections have been scaled in such a way that data is described best (see text). For the diffractive processes two lines corresponding to proton dissociative events (upper line) and elastic events (lower line) are shown.

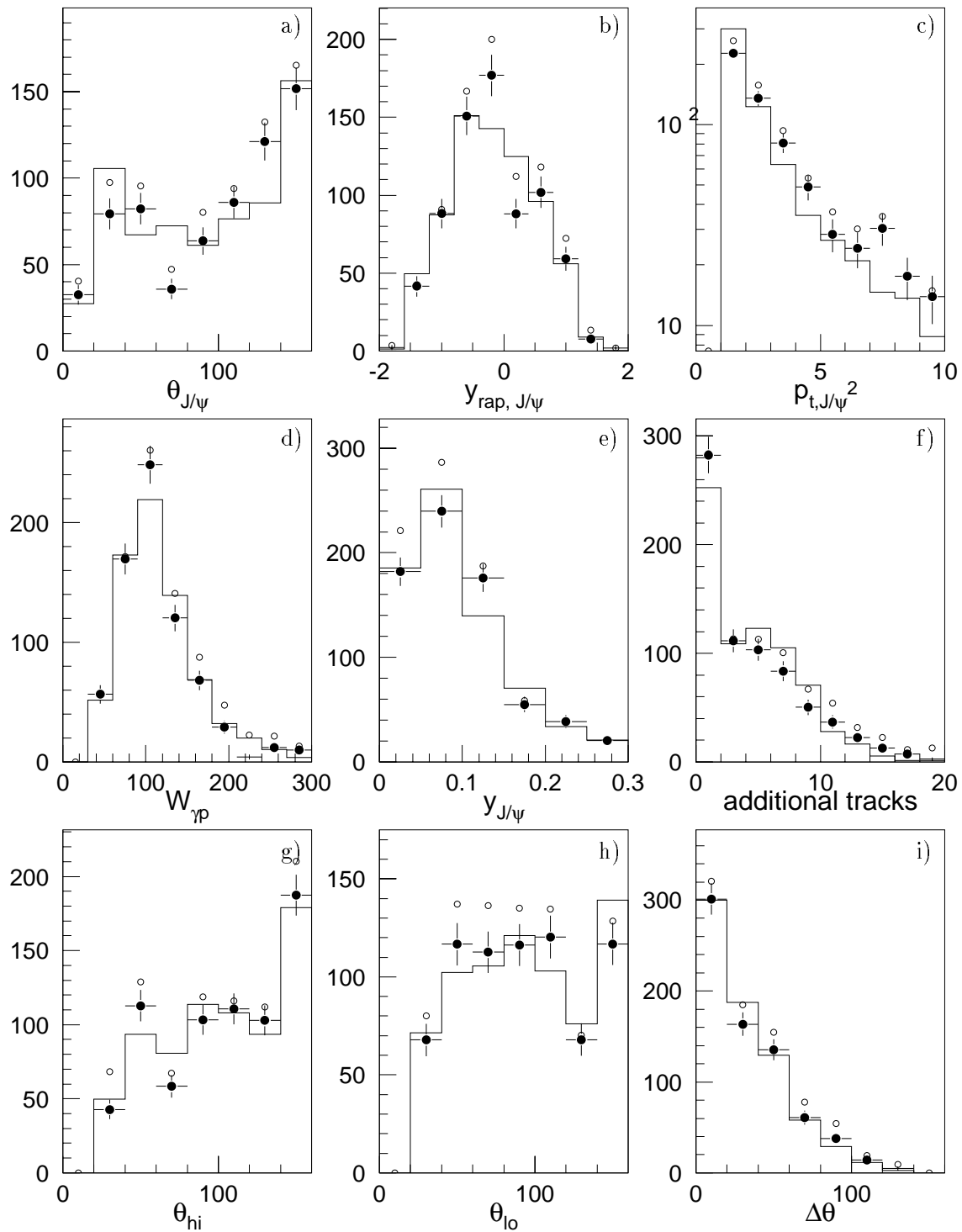


**Figure 4.21:** Comparison of data and mixed Monte Carlo simulation. Part A. The histograms are described in section 4.4. Full (open) dots show background corrected (uncorrected) data. All cuts are listed in table 4.1.

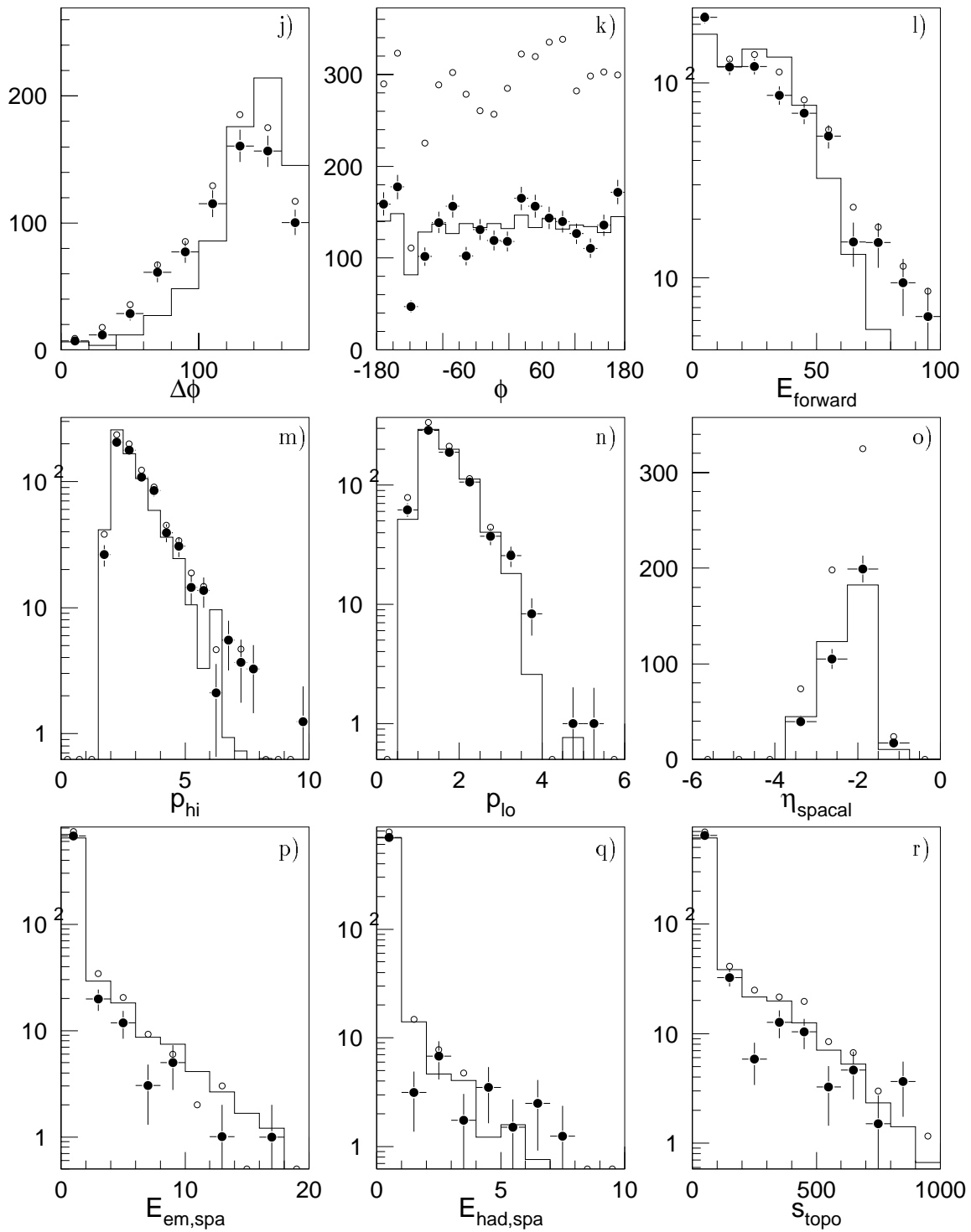


**Figure 4.22:** Comparison of data and **mixed Monte Carlo simulation**. Part B. The histograms are described in section 4.4. Full (open) dots show background corrected (uncorrected) data. All cuts are listed in table 4.1.



# Chapter 5

## Results

In this chapter the differential inclusive photoproduction cross sections will be presented. In the beginning the methods used to obtain the cross sections will be explained. The results will be discussed and compared to previous measurements and theoretical predictions.

### 5.1 Determination of Cross Sections

#### 5.1.1 Signal Fitting and Background Subtraction

The shape of the invariant mass signal is dominated by the resolution of the tracking chambers and can be fitted by a Gaussian. It has been observed that the background contributions can often be described by another Gaussian distribution  $c \cdot e^{-(M-M_0)^2/2\sigma_{bg}}$  ( $\sigma_{bg}$  large). In some kinematic regions a signal from the direct decay of the  $\psi(2S)$  meson into two muons is visible. In these regions another Gaussian at  $M_{\psi(2S)} = 3.69$  GeV (fixed width) will be included in the fit. The integrated area below the background fit function will then be subtracted from the number of  $J/\psi$  candidates (i.e. events with  $|M_{\mu\mu} - M_{J/\psi}| < 250$  MeV) to obtain the background corrected number of events. In regions of small background the so called side band method will be used. The number of background events is then given by  $(N_{left} + N_{right})/600 * 500$ , where  $N_{left/right}$  is the number of events in a 300 MeV wide bin on the low/high mass region of the signal range (which is 500 MeV wide).

Width and position of the signal have been determined once for the total signal after all selection cuts (see figure 4.4 d). The values obtained in this fit will be fixed in all successive fits:

$$\begin{aligned} M_{J/\psi} &= 3.091 \pm 0.006 \text{ GeV} \\ \sigma &= 0.068 \pm 0.005 \text{ GeV} \end{aligned}$$

The measured  $J/\psi$  mass is in agreement with literature [16] ( $M_{J/\psi} = 3.09688 \pm 0.00004$  GeV). The measured width agrees with previous H1 measurements. The Monte Carlo expectation is  $\sigma_{MC} = 63$  MeV.

### 5.1.2 Determination of $ep$ Cross Sections

The differential  $ep$  cross sections are given by

$$\frac{d\sigma_{ep}}{dv} = \frac{N(v)}{\varepsilon(v) \cdot B \cdot \Delta v \cdot \mathcal{L}}, \quad (5.1)$$

where  $v$  is the considered variable,  $\Delta v$  the bin width,  $N(v)$  the background corrected weighted (see sections 4.3, 4.2.3) number of events in each bin of this variable,  $\mathcal{L}$  the integrated luminosity and  $B$  the branching ratio for the decay into two muons ( $B = 0.0601 \pm 0.0019$ , [16]).  $\varepsilon(v)$  is the total efficiency as determined from the mixed Monte Carlo simulation which was described in the previous chapter:

$$\varepsilon(v) = \frac{N_{MC}(v)}{N_{gen}(v)}. \quad (5.2)$$

In each bin  $N_{MC}$  is the number of reconstructed Monte Carlo signal events after all cuts and trigger selection.  $N_{gen}$  is the number of events which were generated in bin  $v$  and fulfill all analysis cuts.

### 5.1.3 Determination of $\gamma p$ Cross Sections

The  $ep$  cross section is related to the  $\gamma p$  cross section by

$$\sigma(ep \longrightarrow eJ/\psi + X) = \int_{y_{min}}^{y_{max}} dy \int_{Q_{min}^2}^{Q_{max}^2} dQ^2 \cdot f_{\gamma,e}(y, Q^2) \cdot \sigma_{\gamma p}(Q^2, y), \quad (5.3)$$

where  $f_{\gamma,e}$  is the virtual photon flux emitted by the electron. For photoproduction ( $Q^2 \lesssim 1 \text{ GeV}^2$ ) the photon is quasi-real and has a transverse polarization. The Weizsäcker-Williams approximation [38, 39] can be used:

$$f_{\gamma,e}(y, Q^2) \simeq \frac{\alpha}{2\pi} \frac{1}{yQ^2} \cdot \left( 1 + (1-y)^2 - \frac{2m_e^2 y^2}{Q^2} \right) \quad (5.4)$$

The integration limits are given by the acceptance region:

$$Q_{min}^2 = m_e^2 \cdot \frac{y^2}{1-y} \quad (5.5)$$

$$Q_{max}^2 = 1 \text{ GeV}^2 \quad (5.6)$$

$\sigma_{\gamma p}$  varies only slightly as a function of  $Q^2$  (for  $Q^2 < 1 \text{ GeV}$ ) and within a given  $y$  range and can be moved in front of the integral. The  $\gamma p$  cross section is then given by

$$\sigma(\gamma p \longrightarrow J/\psi + X) \simeq \sigma(ep \longrightarrow eJ/\psi + X)/\Phi, \text{ where} \quad (5.7)$$

$$\Phi = \int_{y_{min}}^{y_{max}} \int_{Q_{min}^2}^{Q_{max}^2} dQ^2 \cdot f_{\gamma,e}(y, Q^2). \quad (5.8)$$

A numerical integration yields the integrated flux factors  $\Phi$  listed in table 5.1.

$W_{\gamma p}$ range [GeV]	$y$ range	integrated flux $\Phi$
40 – 90	0.018 – 0.090	0.0742
90 – 140	0.090 – 0.218	0.0320
140 – 190	0.218 – 0.401	0.0173
190 – 300	0.401 – 1.000	0.0175
40 – 300	0.018 – 1.000	0.1410
90 – 300	0.090 – 1.000	0.0668
50 – 180	0.028 – 0.360	0.0980

**Table 5.1:** Integrated photon flux ( $Q^2 < 1 \text{ GeV}^2$ ) for each  $W_{\gamma p}$  range which is used in this analysis.

#### 5.1.4 Statistical and Systematic Errors

The square root of the number of  $J/\psi$  candidates before background subtraction will be taken as statistical error. In regions of large background an error due to the unknown exact shape of the background contributions will be estimated by changing the background fit function from a Gaussian to an exponential law  $c \cdot e^{-\kappa M}$ . This error will be added in quadrature to the statistical error.

error type	value
reconstruction and trigger efficiencies	10 %
branching ratio $J/\psi \rightarrow \mu\mu$	3 %
luminosity	3 %
photon flux	4 %
parton density functions	10%...20% (see text)

**Table 5.2:** Systematic errors in the determination of cross sections.

Table 5.2 lists the systematic errors taken into account. All systematic errors will be added in quadrature to obtain the total systematic error. In the present analysis the subtrigger efficiencies were obtained from optimized Monte Carlo simulations. The remaining uncertainties including reconstruction and trigger efficiencies were estimated to be  $\sim 10\%$ . The error which is due to the approximation used in the calculation of the photon flux was adopted from [11]. The dominant error arises from the uncertainty in the parameterization of the photon and parton density functions. The total selection efficiency for different combinations of proton and photon PDFs is shown in figure 5.1. An error of 20% for the lowest  $z$  bin and 10% for the other bins was estimated from this.

An additional error arises from model dependencies: In the high  $z$  region a diffractive Monte Carlo was used to describe the data. If the measured contributions at high  $z$  are interpreted as color octet contributions one has to keep in mind that an additional systematic error has

to be added due to the *wrong* model which has been used to describe the data. It is hard to quantify this error but it is mentioned here for completeness. The same applies for the low  $z$  region, where a color singlet resolved Monte Carlo has been used to describe the data. However the kinematics of color octet resolved processes are similar to the ones of color singlet resolved processes. The color octet graph for  $J/\psi$  mesons from  $^3S_1$  states is identical with the color singlet graph (see figure 2.6 *a*). In the leading order octet graph for  $^1S_0$  and  $^3P_J$  states a gluon is radiated before the bound  $c\bar{c}$  state is formed and the transition to a colorless final state is accomplished by the radiation of soft gluons (see figure 2.6 *b*). One would not expect this to change the kinematics drastically.

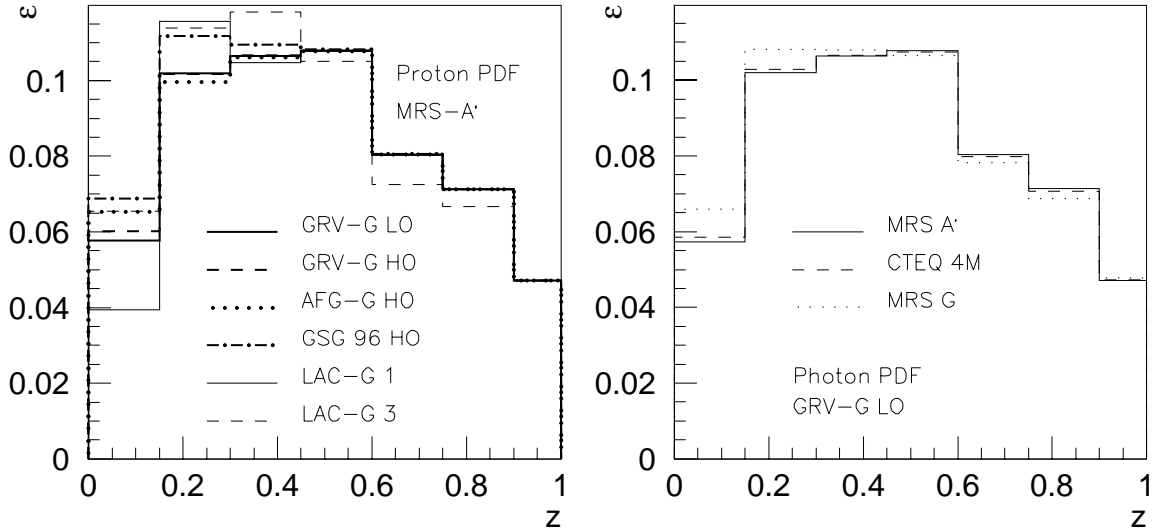


**Figure 5.1:** The total selection efficiency as determined from the mixed Monte Carlo simulation with different parameterizations of the photon and proton parton density functions. All cuts are listed in table 4.1.

## 5.2 Measured Cross Sections

The inclusive  $ep \rightarrow eJ/\psi + X$  cross sections have been determined in the kinematical range:

- $Q^2 < 1 \text{ GeV}^2$  (photoproduction)
- $40 < W_{\gamma p} < 300 \text{ GeV}$  and  $90 < W_{\gamma p} < 300 \text{ GeV}$
- $p_{t,J/\psi} > 1 \text{ GeV}$

Before the results are presented a few remarks should be made: no  $z$  cut will be applied and  $W_{\gamma p}$  will be included up to its kinematic limit (which is given by the HERA center of mass energy  $\sqrt{s}$ ). This is necessary since the detector acceptance for resolved photon events has a maximum at  $W_{\gamma p, max} \sim 200 \text{ GeV}$  (see figure 4.14, histogram *d*) compared to  $W_{\gamma p, max} \sim 100 \text{ GeV}$  for events of intermediate or high  $z$  (see figure 4.16, histogram *d*). The cross section will also be determined for  $90 < W_{\gamma p} < 300 \text{ GeV}$  – this is the range where resolved photon events are actually measured.

The cut on  $p_{t,J/\psi}$  has several reasons: a) it improves the signal to background ratio at low  $z$ , b) it excludes the region of phase space with lowest selection efficiency (see figure 2.9 c)), c) it eliminates a large amount of diffractive contributions at  $z$  close to unity and d) predictions are not believed to be reliable for  $p_{t,J/\psi} < 1$  GeV (the COM factorization formula breaks down [9]).

When the binned cross sections are compared to a continuous theoretical prediction  $g(x)$ , the data points are drawn at the point  $x'$  where the value of the predicted function is equal to its mean value over the bin [42]:

$$g(x') = \frac{1}{\Delta x} \int_{x_1}^{x_2} g(x) dx, \quad (5.9)$$

where  $\Delta x$  is the bin width and  $x_{1/2}$  are the bin's lower and upper bound.

### $\gamma p$ Cross Section as a Function of $W_{\gamma p}$

The  $\gamma p$  cross section as a function of  $W_{\gamma p}$  for  $p_{t,J/\psi} > 1$  GeV is shown in figure 5.2. Figure 5.3 shows the corresponding invariant mass signals in bins of  $W_{\gamma p}$ . Table 5.3 summarizes the relevant data for the determination of the cross section. In contrast to the  $ep$  cross section (not shown) the  $\gamma p$  cross section increases with  $W_{\gamma p}$ . The measured  $W_{\gamma p}$  cross section can be fitted with a power law  $W_{\gamma p}^\alpha$  with

$$\alpha = 0.95 \pm 0.02 \quad (5.10)$$

Note that the shown cross section includes the full  $z$  range and thus cannot easily be compared to previous analyses (H1 [11], ZEUS [40]). See section 5.3 for a comparison in a restricted kinematic range.

$W_{\gamma p}$ [GeV]	40 – 90	90 – 140	140 – 190	190 – 300
# events	$264 \pm 17$	$372 \pm 22$	$137 \pm 15$	$78 \pm 13$
$\varepsilon$ [%]	6.31	11.67	6.57	2.00
$\sigma_{ep}$ [nb]	3.93	2.98	1.99	3.69
$\Phi$	0.0742	0.0320	0.0173	0.0175
$\sigma_{\gamma p}$ [nb]	$53 \pm 5 \pm 7$	$93 \pm 8 \pm 15$	$115 \pm 16 \pm 18$	$211 \pm 47 \pm 33$

**Table 5.3:** Numbers for the determination of the  $W_{\gamma p}$  cross section for  $p_{t,J/\psi} > 1$  GeV. The corresponding invariant mass signals are shown in figure 5.3.

### Differential $\gamma p$ Cross Sections as a Function of $z$

The differential  $\gamma p$  cross section as function of  $z$  for  $p_{t,J/\psi} > 1$  GeV and  $40 < W_{\gamma p} < 300$  GeV is shown in figure 5.5. In the same figure the higher order predictions (see section 2.5) by Kniehl and Kramer [17] for contributions from direct and resolved and from color singlet and color octet states and the sum of all contributions are shown. The same data are compared to the corresponding leading order predictions by the same authors in figure 5.6. The numbers for the determination of the cross section are summarized in table 5.4. The cross section has been

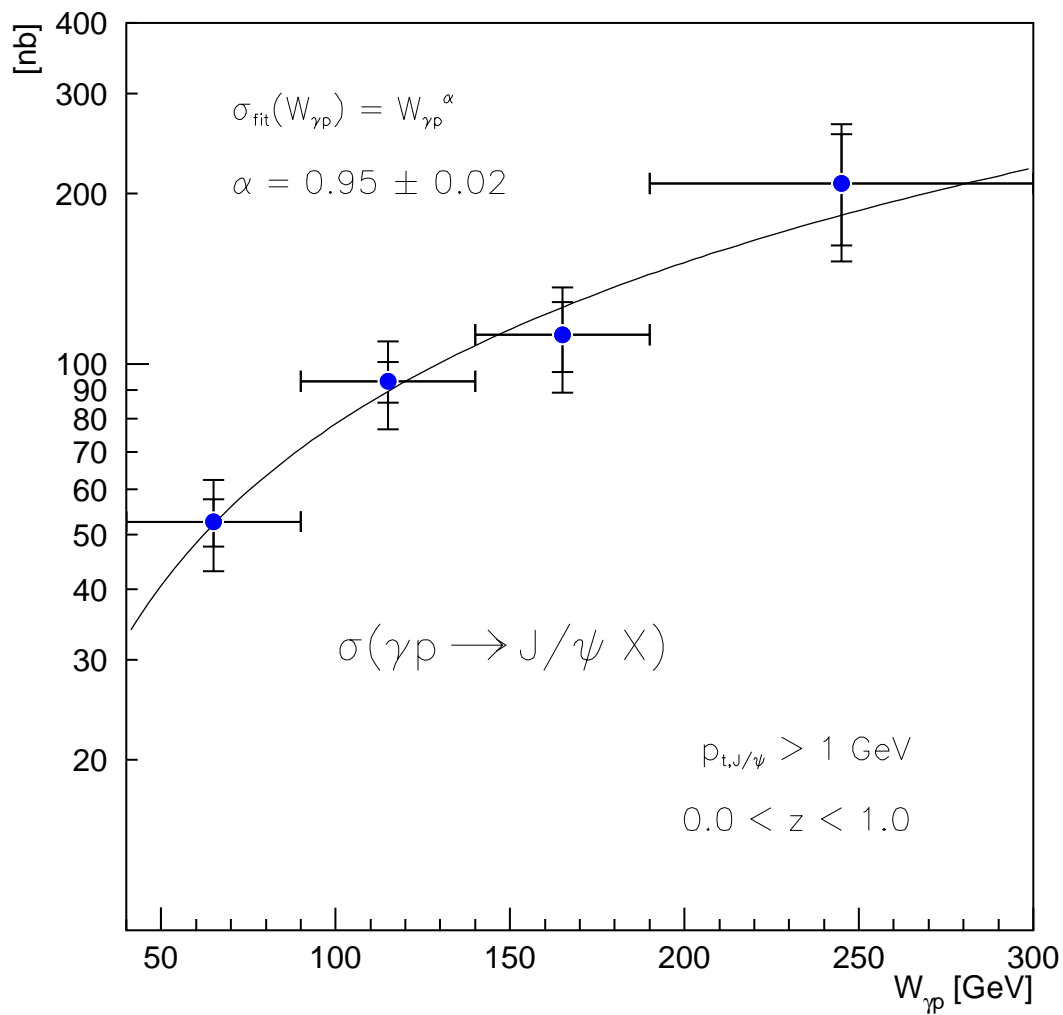


**Figure 5.2:** Measured  $\gamma p$  cross section for  $p_{t,J/\psi} > 1 \text{ GeV}$  as a function of  $W_{\gamma p}$ . The line shows a fit to the data of the form indicated. The inner error bars indicate the statistical uncertainty, the outer error bars the quadratic sum of statistical and systematic uncertainties.

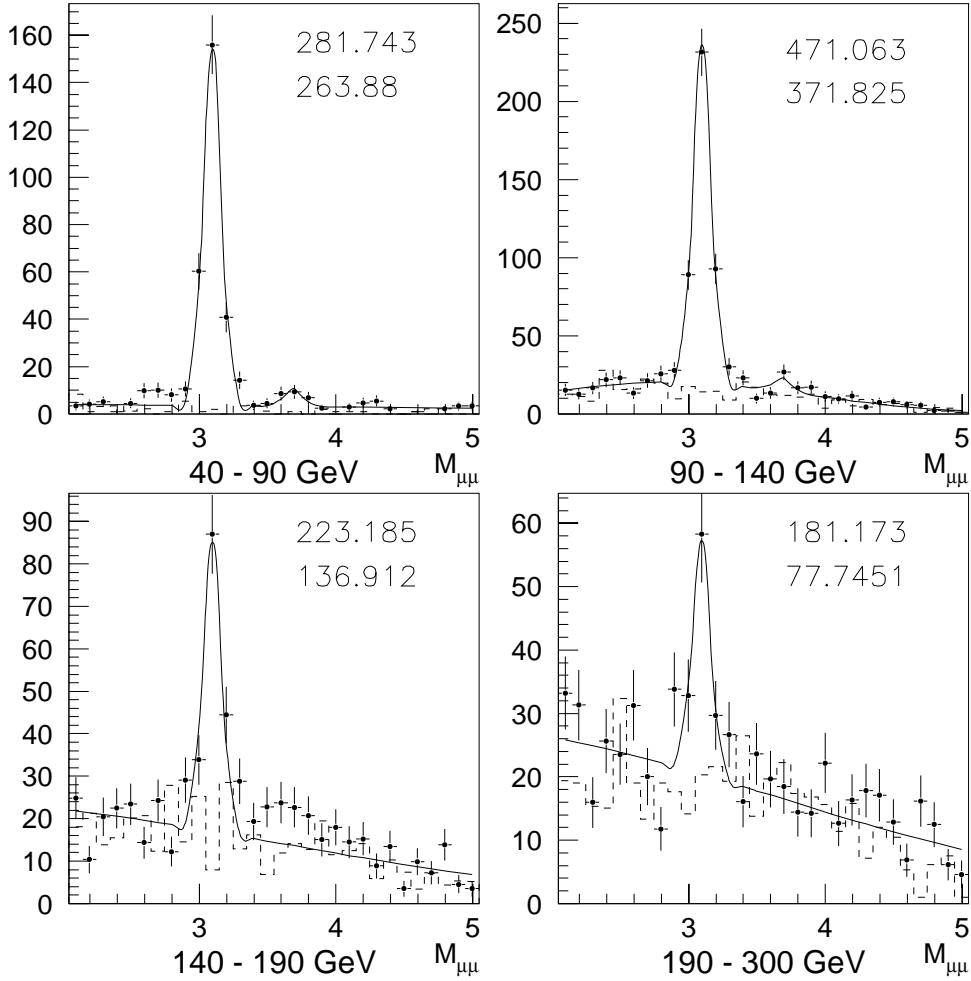


**Figure 5.3:** Invariant mass signal in bins of  $W_{\gamma p}$  for  $p_{t, J/\psi} > 1$  GeV. The number of events in the  $J/\psi$  mass range before (top) and after (bottom) background subtraction is shown in each histogram. The full line is a fit used for subtracting background. The dashed histogram shows the background spectrum of muons with equal charge.

obtained by dividing the measured  $ep$  cross section by the integrated photon flux of the full  $W_{\gamma p}$  range. The invariant mass signals are shown in figure 5.4. The theoretical predictions for the low  $z$  region are summarized in table 5.5.

The detector acceptance for  $J/\psi$  mesons in resolved photon processes has its maximum at  $W_{\gamma p} \simeq 200$  GeV. In figure 5.7 the cross sections is thus shown in a limited kinematic range  $90 < W_{\gamma p} < 300$  GeV which is more adequate for resolved photon processes. The corresponding higher order predictions are shown as well.

Good agreement in the shape of the  $z$  distributions and higher order predictions in the color octet model is observed in the full  $z$  range and for both  $W_{\gamma p}$  ranges. The predictions need to be scaled by a substantial  $k$  factor of 3.0 to achieve a match in overall normalization. Kniehl and Kramer suggest such a  $k$  factor as a result of still missing NLO corrections. The cross section at low  $z$  is not compatible with resolved color singlet contributions alone (only within  $\sim 3\sigma$ ). The same applies for large  $z$ .

The agreement of data and LO color octet predictions is poor. Predictions overshoot data at low  $z$  by roughly a factor 4 as well as at high  $z$  by an even larger factor. The data show an excess over resolved color singlet contributions alone.

$z$	0–0.15	0.15–0.3	0.3–0.45	0.45–0.6
# events	$51 \pm 12$	$61 \pm 13$	$69 \pm 11$	$95 \pm 11$
$\varepsilon$ [%]	5.76	10.20	10.65	10.78
$\sigma_{\gamma p}$ [nb]	$39 \pm 11 \pm 10$	$26 \pm 7 \pm 4$	$29 \pm 6 \pm 4$	$39 \pm 6 \pm 6$
$z$	0.6–0.75	0.75–0.9	0.9–1.0	
# events	$122 \pm 12$	$148 \pm 13$	$312 \pm 18$	
$\varepsilon$ [%]	8.04	7.13	4.71	
$\sigma_{\gamma p}$ [nb]	$67 \pm 10 \pm 10$	$92 \pm 12 \pm 13$	$440 \pm 38 \pm 67$	

**Table 5.4:** Numbers for the determination of the differential cross section as a function of  $z$  for  $p_{t,J/\psi} > 1$  GeV and  $40 < W_{\gamma p} < 300$  GeV. The corresponding invariant mass signals are shown in figure 5.4.

$\sigma_{\gamma p}$ [nb]	$0 < z < 0.15$	$0.15 < z < 0.3$
data	$39 \pm 11 \pm 10$	$26 \pm 7 \pm 4$
HO CS resolved	$\sim 10$	$\sim 1.1$
HO CO resolved	$\sim 22.5$	$\sim 3.3$
HO CS direct	$\sim 1.5$	$\sim 13.2$
HO CO direct	$\sim 0.0$	$\sim 0.4$
sum HO CS	$\sim 11.5$	$\sim 14.3$
sum HO CS+CO	$\sim 34$	$\sim 18$
LO CS resolved	$\sim 4.7$	$\sim 0.0$
LO CO resolved	$\sim 125$	$\sim 16$
LO CS direct	$\sim 0.3$	$\sim 5.1$
LO CO direct	$\sim 0.0$	$\sim 2.0$
sum LO CS	$\sim 5.0$	$\sim 5.1$
sum LO CS+CO	$\sim 130$	$\sim 23.1$

**Table 5.5:** Leading order (LO) and higher order (HO) predictions by Kniehl and Kramer [46] for  $40 < W_{\gamma p} < 300$  GeV and  $p_{t,J/\psi} > 1$  GeV in the color singlet (CS) and color octet (CO) model compared to data in the low  $z$  range.

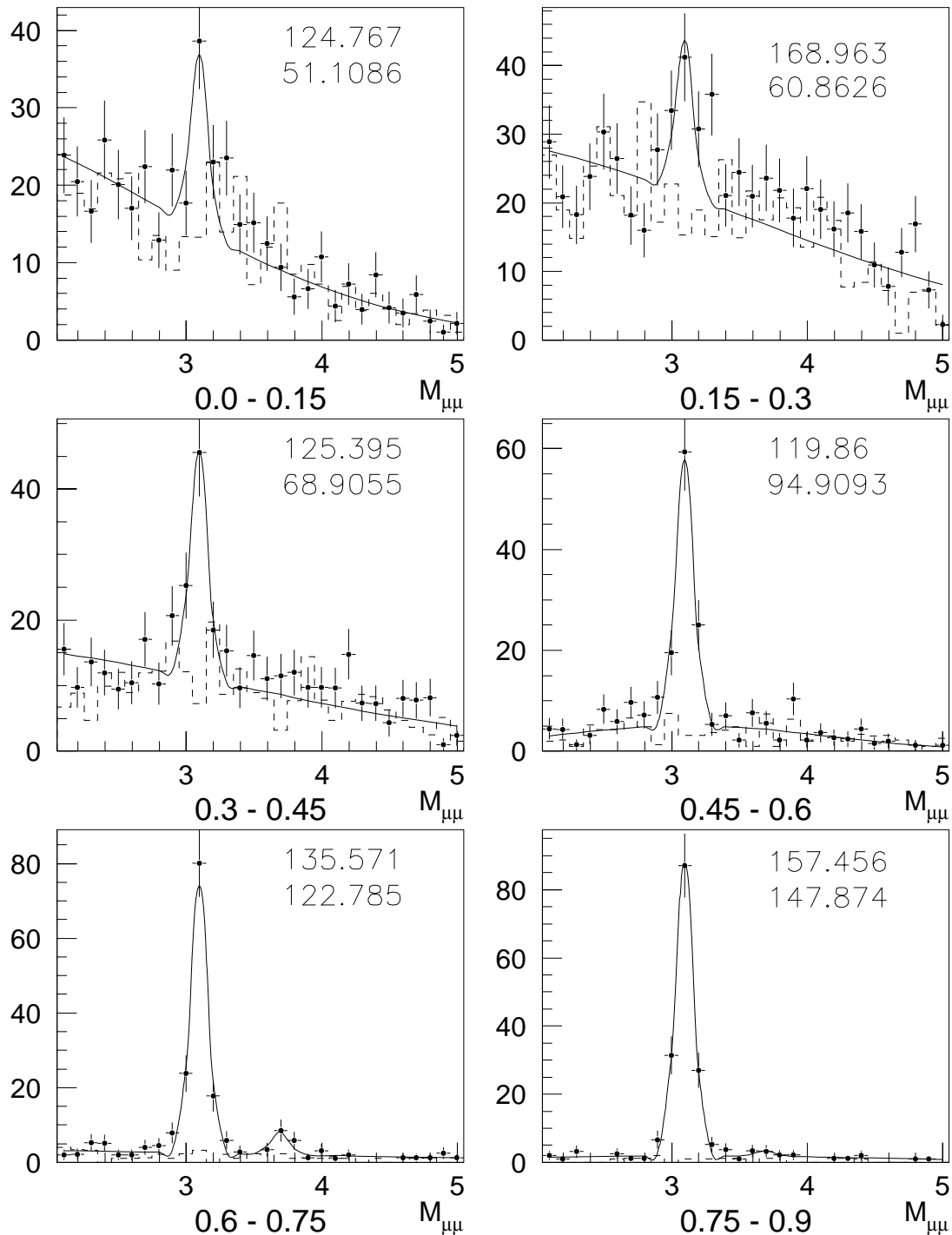


**Figure 5.4:** Invariant mass signal in bins of  $z$  for  $p_{t,J/\psi} > 1$  GeV and  $40 < W_{\gamma p} < 300$  GeV. The number of events in the  $J/\psi$  mass range before (top) and after (bottom) background subtraction is shown in each histogram. The dashed histogram shows the background spectrum of muons with equal charge.

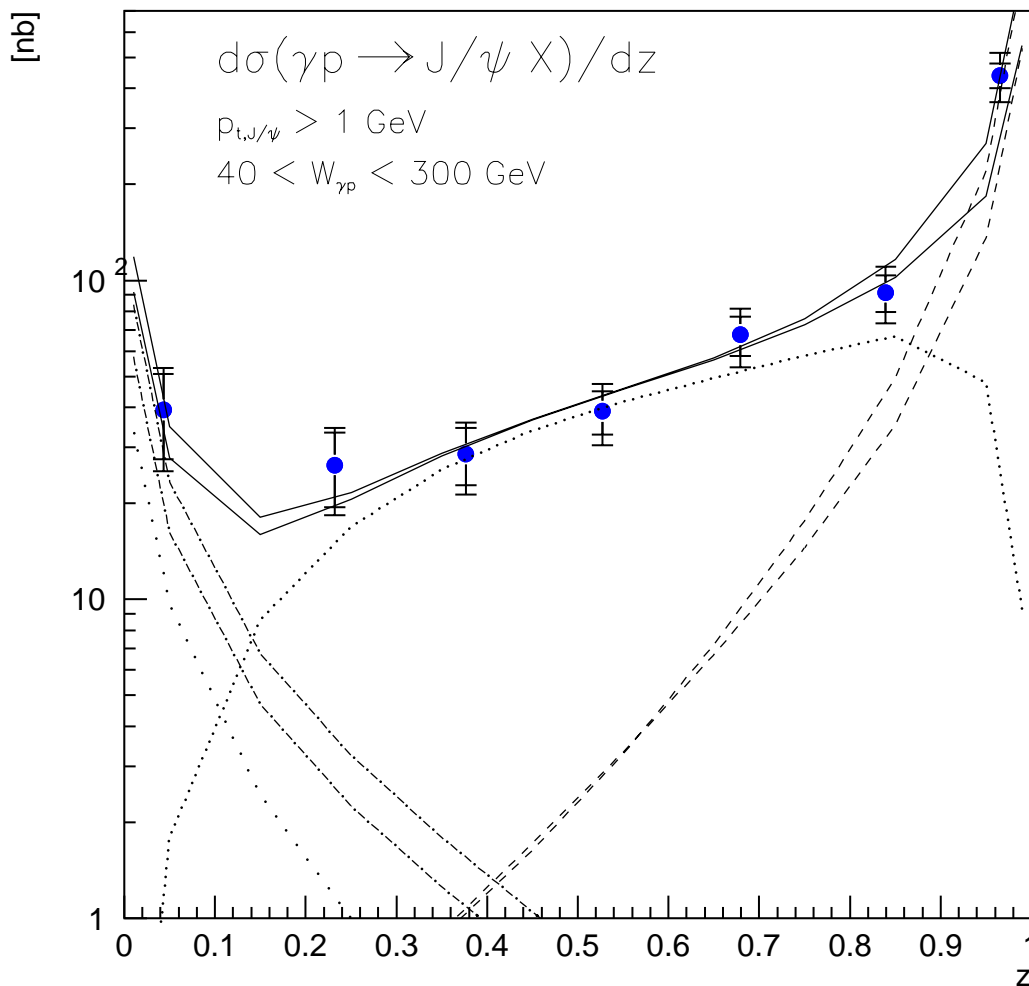


**Figure 5.5:** Differential  $\gamma p$  cross section for  $p_{t,J/\psi} > 1$  GeV and  $40 < W_{\gamma p} < 300$  GeV as a function of  $z$ . The inner error bars indicate the statistical uncertainty, the outer error bars the quadratic sum of statistical and systematic uncertainties. The **higher order** predictions for various processes are shown as lines [46]: Resolved photon in the color singlet model (wide dots) and additional contributions in the color octet model (dash dotted); boson gluon fusion color singlet (narrow dots) and additional color octet contributions (dashed). The sum of all contributions is shown as a solid line. A  **$k$  factor of 3.0** has been applied to the predictions, 15% contributions from  $\psi(2S)$  are included. GRV-HO and CTEQ4M are the photon and proton PDFs used in the predictions. For each color octet process two predictions are shown corresponding to the uncertainty in the color octet matrix elements which is due to the fact that the fit to Tevatron data fixes only a linear combination of matrix elements.

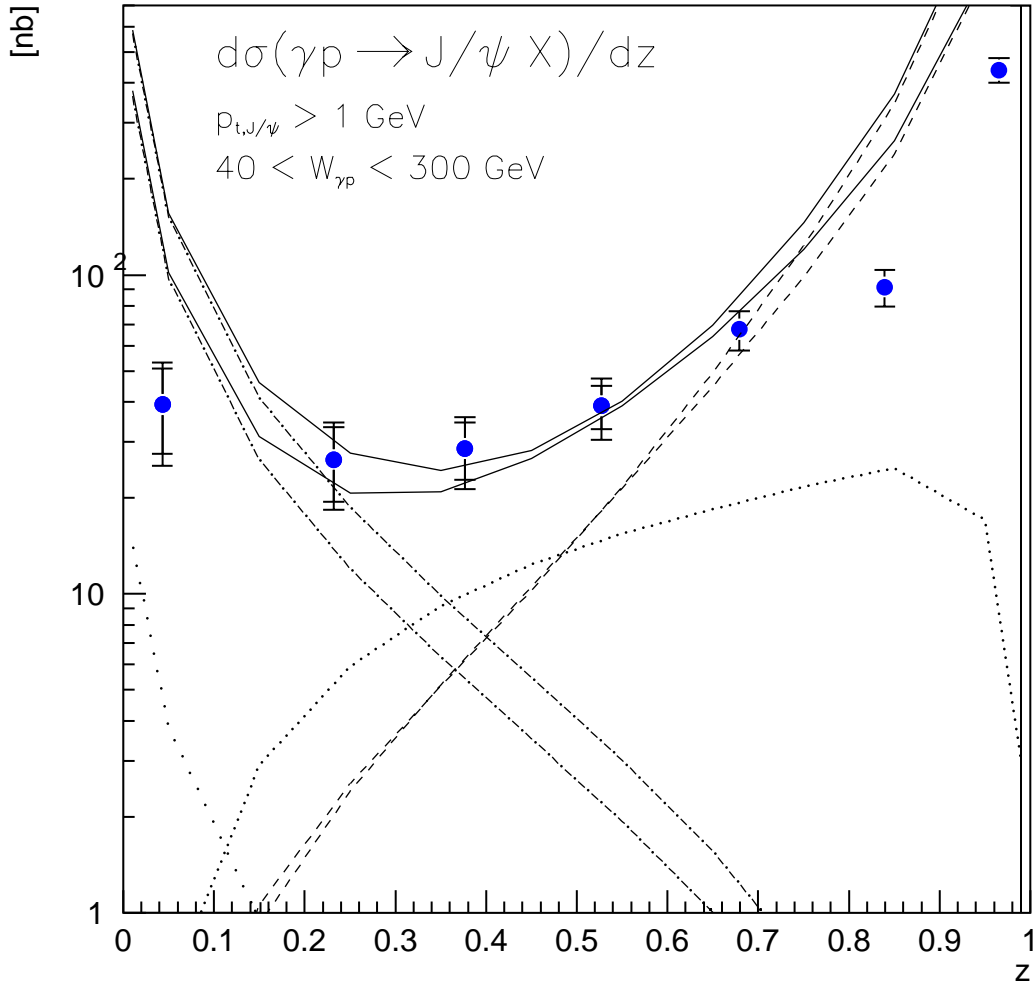


**Figure 5.6:** Differential  $\gamma p$  cross section for  $p_{t,J/\psi} > 1 \text{ GeV}$  and  $40 < W_{\gamma p} < 300 \text{ GeV}$  as a function of  $z$ . The inner error bars indicate the statistical uncertainty, the outer error bars the quadratic sum of statistical and systematic uncertainties. The **leading order** predictions for various processes are shown as lines [46] (**no  $k$  factor**): Resolved photon in the color singlet model (wide dots) and additional contributions in the color octet model (dash dotted); boson gluon fusion color singlet (narrow dots) and additional color octet contributions (dashed). The sum of all contributions is shown as a solid line. 15% contributions from  $\psi(2S)$  are included. GRV-HO and CTEQ4M are the photon and proton PDFs used in the predictions. For each color octet process two predictions are shown corresponding to the uncertainty in the color octet matrix elements which is due to the fact that the fit to Tevatron data fixes only a linear combination of matrix elements.

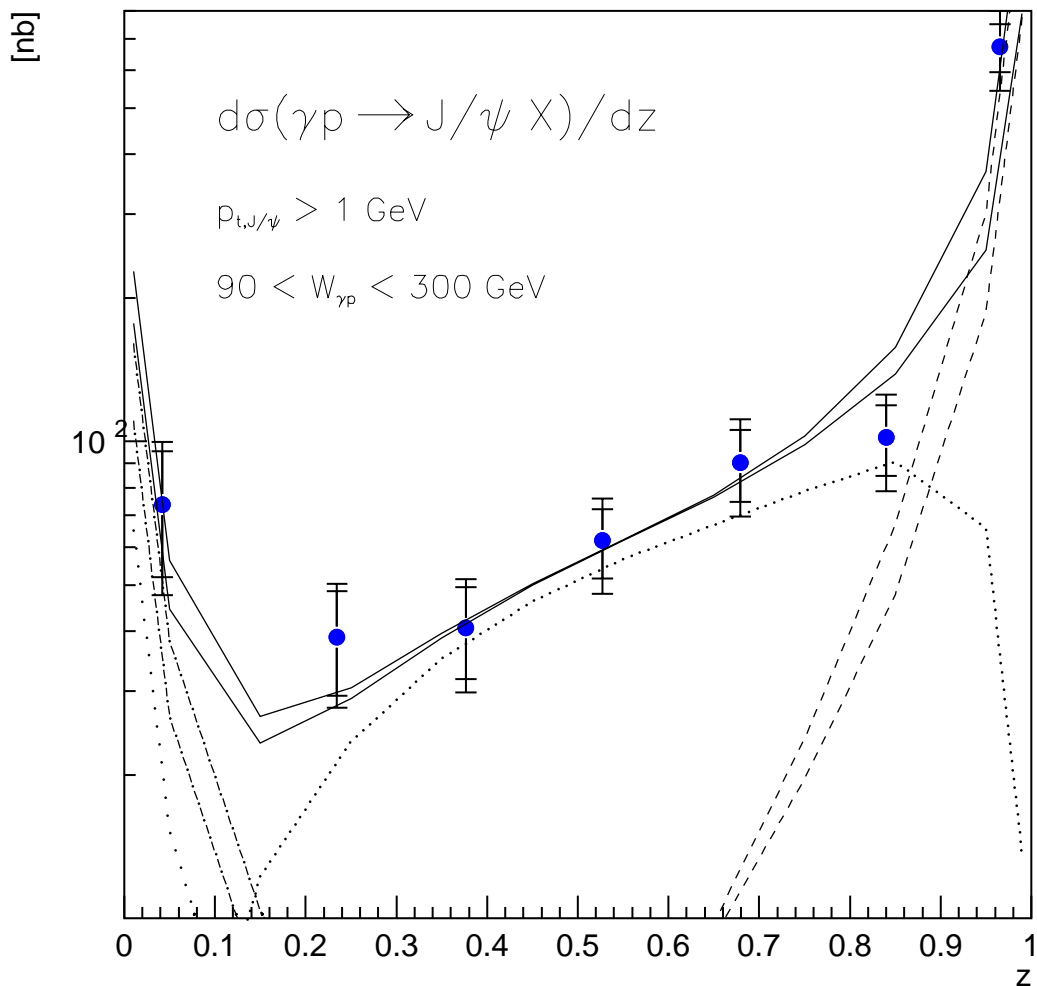


**Figure 5.7:** Differential  $\gamma p$  cross section for  $p_{t,J/\psi} > 1 \text{ GeV}$  and  $90 < W_{\gamma p} < 300 \text{ GeV}$  as a function of  $z$ . The inner error bars indicate the statistical uncertainty, the outer error bars the quadratic sum of statistical and systematic uncertainties. The **higher order** predictions for various processes are shown as lines [46]: Resolved photon in the color singlet model (wide dots) and additional contributions in the color octet model (dash dotted); boson gluon fusion color singlet (narrow dots) and additional color octet contributions (dashed). The sum of all contributions is shown as a solid line. A  **$k$  factor of 3.0** has been applied to the predictions, 15% contributions from  $\psi(2S)$  are included. GRV-HO and CTEQ4M are the photon and proton PDFs used in predictions. For each color octet process two predictions are shown corresponding to the uncertainty in the color octet matrix elements which is due to the fact that the fit to Tevatron data fixes only a linear combination of matrix elements.

### 5.3 Comparison to Previous Measurements

In previous measurements cross sections have been determined in a restricted kinematic range. The cross sections will also be determined in this restricted kinematic range with the aim of testing the used procedure:

- $0.4 < z < 0.9$
- $50 < W_{\gamma p} < 180$
- $p_{t,J/\psi} > 1 \text{ GeV}$

The results (dots) are shown together with the results from ZEUS (triangles, based on data from 1997, [40]) in figures 5.8 and 5.9. Good agreement is observed in  $d\sigma_{\gamma p}/dz$  as well as in  $\sigma_{\gamma p}(W_{\gamma p})$ . The highest  $W_{\gamma p}$  data point from this analysis is lower than the ZEUS measurement but agrees within the errors. The  $z$  distribution of the present analysis shows some excess at high inelasticities compared to the ZEUS analysis. This could be an effect of a cut on the calorimetric energy deposition in the forward region which has been applied in the ZEUS analysis. The motivation of this cut was to reduce contributions from diffractively produced  $J/\psi$  mesons. The amount of energy which is deposited in the forward calorimeter is correlated to the invariant mass  $M_X$  of the proton remnant system. One expects low invariant masses ( $M_X \lesssim 15 \text{ GeV}$ ) for diffractively produced  $J/\psi$  mesons [43]. Theoretical NLO predictions in the color singlet model are shown as solid lines.

The differential cross section as a function of  $p_{t,J/\psi}^2$  for  $50 < W_{\gamma p} < 180 \text{ GeV}$  and  $0.4 < z < 0.9$  is compared to the ZEUS 1994 analysis in figure 5.10. The higher order predictions from Kniehl and Kramer [17] with a  $k$  factor of 3.0 are also shown. Good agreement of both measurements is observed in the overlapping  $p_{t,J/\psi}^2$  regions. The observed mismatch of data and predictions can be interpreted in at least three ways: a) When normalizing the theoretical predictions to the measurement at  $p_{t,J/\psi}^2 \sim 1 \text{ GeV}^2$  one observes that the measured spectrum is flatter (harder) than predicted. The mismatch is often ascribed to missing NLO corrections. b) When ignoring the low  $p_{t,J/\psi}^2$  data points good agreement is observed. A possible interpretation is that the color octet model is only reliable for  $p_{t,J/\psi}^2 \gtrsim 2 \text{ GeV}^2$ . c)  $J/\psi$  mesons from  $B$  meson decays contribute at large  $p_{t,J/\psi}$  (see figure 2.11). It is not clear whether these are negligible.

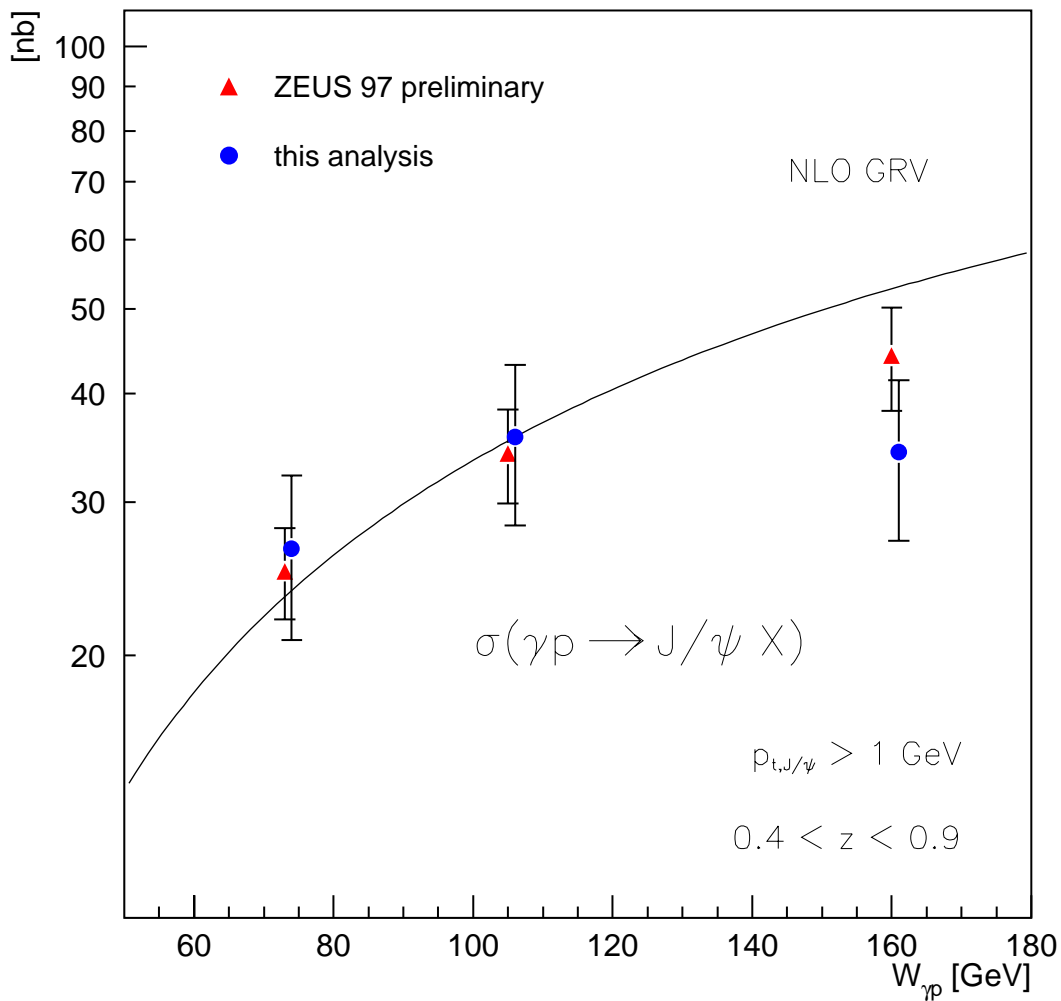


**Figure 5.8:** The inelastic photoproduction cross section as a function of  $W_{\gamma p}$  for  $0.4 < z < 0.9$  and  $p_{t,J/\psi} > 1 \text{ GeV}$ . The results from this analysis (points) are compared to ZEUS results (triangles). The line represents the NLO prediction in the color singlet model using the GRV proton density function,  $m_c = 1.4 \text{ GeV}$  and  $\Lambda_{QCD} = 300 \text{ GeV}$ . The curve is scaled by a factor 1.15 to take into account the contributions from  $\psi' \rightarrow J/\psi X$ . The error bars show the quadratic sum of statistical and systematic uncertainties.

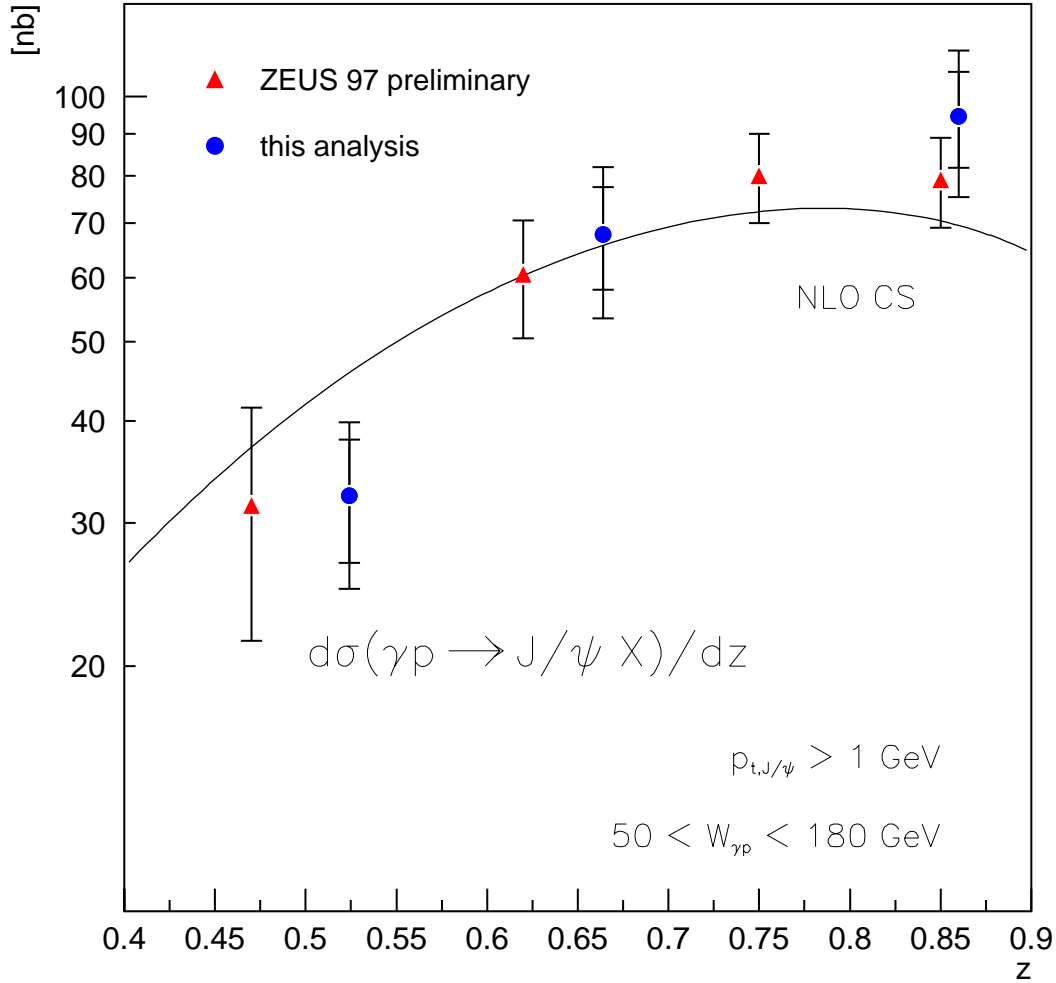


**Figure 5.9:** Differential  $\gamma p$  cross section for  $p_{t,J/\psi} > 1 \text{ GeV}$  and  $40 < W_{\gamma p} < 300 \text{ GeV}$  as a function of  $z$ . The results from this analysis (points) are compared to ZEUS results (triangles). The line represents the NLO prediction in the color singlet model using the GRV proton density function,  $m_c = 1.4 \text{ GeV}$  and  $\Lambda_{QCD} = 300 \text{ GeV}$ . The inner error bars indicate the statistical uncertainty, the outer error bars the quadratic sum of statistical and systematic uncertainties. For the ZEUS points the quadratic sum of statistical and systematic uncertainties is shown.

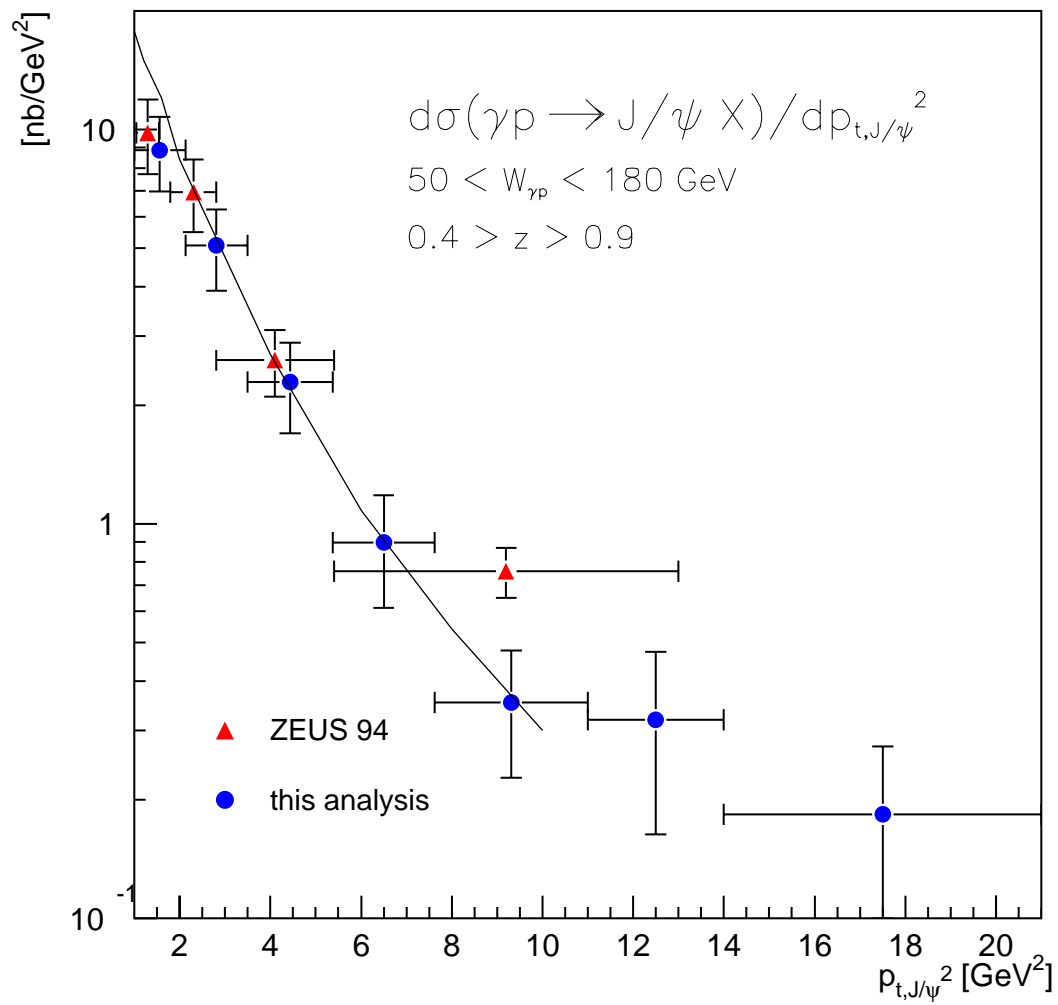


**Figure 5.10:** Differential  $\gamma p$  cross section for  $0.4 < z < 0.9$  and  $50 < W_{\gamma p} < 180$  GeV as a function of  $p_{t,J/\psi}^2$ . The theoretical higher order prediction by Kniehl and Kramer with a  $k$  factor 3.0 is shown as a solid line. The error bars show the quadratic sum of statistical and systematic uncertainties.

## Chapter 6

# Conclusions and Outlook

In this thesis an inclusive  $J/\psi$  selection using the decay channel  $J/\psi \rightarrow \mu\mu$  was presented. The data have been collected with the H1 detector at the  $ep$  collider HERA and correspond to an integrated luminosity of approximately  $18 \text{ pb}^{-1}$ . A mixed Monte Carlo simulation containing resolved photon, photon gluon fusion and diffractive processes was optimized to describe the data. It was used to extract differential cross sections as a function of the photon proton center of mass energy  $W_{\gamma p}$ , the  $J/\psi$  meson's inelasticity  $z$  and its squared transverse momentum  $p_{t,J/\psi}^2$ . The data were compared to leading order and higher order predictions for  $J/\psi$  meson production in the color singlet and color octet models.

The full  $z$  range was included in the data selection. Including resolved photon processes required an improved reconstruction of the scaling variable  $y$ . The existing method was extended to include the Spacal cells to take account of the photon remnant when applying the Jacquet Blondel Method. In addition a method which is able to separate photoproduction from DIS without discarding events with activity from the photon remnant in the Spacal had to be developed. The increasing background at low  $z$  required an additional cut on the polar angle of the decay leptons. This cut was motivated by Monte Carlo studies. Furthermore it was found that a cut on the transverse momentum of the  $J/\psi$  meson is not only desirable from a theoretical point of view, but it also excludes the kinematic region of lowest selection efficiency and largest background contributions. It was pointed out that the poor forward tracking detector invariant mass resolution and problems with the reconstruction efficiency of the forward muon detector and linking of inner and outer tracks in the forward region did not allow the inclusion of the forward region in the present inelastic  $J/\psi$  analysis.

The measured cross sections agree with previous measurements in a kinematic range which is common to both. In a kinematic range extended towards low and high inelasticities  $z$  data and higher order color octet model predictions agree well in normalization and shape, if a  $k$  factor of 3.0 is applied. The smaller values of the color octet matrix elements which are obtained from new fits to the Tevatron data cure the discrepancies between HERA color octet model predictions and data at large  $z$ . It was shown that the cross section at low  $z$ , which is dominated by resolved photon processes, is compatible with these higher order predictions. The measured  $z$  dependence, both at large and at small  $z$ , is not compatible with significantly larger color octet matrix elements which were obtained by Tevatron fits in earlier publications. With the new smaller matrix elements a consistent picture is obtained in the light of the color octet model, however the color singlet model cannot be ruled out by the data. The color singlet and color

octet models have a normalization uncertainty which is due to the used scale, the value of  $\alpha_s$  and the parton density functions. Together with experimental uncertainties the measured cross section at low  $z$  is still compatible with the color singlet model, though data favors the color octet model. One should keep in mind that a non negligible part of the low  $z$  signal might be caused indirectly by  $J/\psi$  mesons from decaying  $\chi$  mesons – resulting in an even lower real  $J/\psi$  cross section.

For the high  $z$  region an important objection that can be raised against the interpretation of the large measured cross section as originating from color octet processes is that diffractive processes may produce the same  $z$  and  $p_{t,J/\psi}$  distributions as photon gluon fusion color octet processes. Traditionally diffractive processes were believed to produce  $J/\psi$  mesons with low transverse momenta ( $p_{t,J/\psi} < 1$  GeV) [23]. In the BFKL approach [44, 45] this is not true. It is possible that the  $J/\psi$  mesons at large inelasticities  $z$  can fully or in part be described by diffractive processes.

It will be the task of future analyses to decide whether the color octet contributions in  $J/\psi$  meson production are required to describe the data or whether the color singlet model is sufficient. An answer to this question will probably only be possible when considering both the direct and the resolved production process. Here are some ideas for future analyses:

- The Monte Carlo generator EPJPSI should be extended to simulate color octet processes. Efficiencies should be determined from color octet Monte Carlo simulations.
- Development of dedicated low  $z$  subtriggers: one could drop the requirement of a link between FMD and drift chamber track (trigger level 4). To reduce background one could make use of the fact that the decay muons from low  $z$   $J/\psi$  mesons are dominantly found in the forward detector region. A condition on the total energy in the Spacal might be better (to trigger on the photon remnant) than the IET trigger. Finally the neural net muon trigger can be optimized for  $J/\psi$  mesons at low inelasticities.
- Study of the contributions from  $B$  meson decays ( $B \rightarrow J/\psi + X$ ) with the help of the newly installed silicon micro-vertex detector.
- It may be that the invariant mass resolution can be improved by the use of the micro-vertex detector. In regions of large background the invariant mass window around the  $J/\psi$  mass can then be narrowed and background can be rejected more efficiently.
- Study of the  $J/\psi$  meson's decay angular distributions. These have no theoretical normalization uncertainty and predictions for the color singlet and octet model are available [41]. More luminosity is required for this analysis since the angular distributions of the two models differ clearly only at large  $p_{t,J/\psi}$ .
- The influence of different track multiplicities in data and Monte Carlo needs further study. The DCR\_Ph and z-Vertex trigger elements may depend on track multiplicities [48].
- The statistical error can be reduced with more luminosity.

# Appendix A

## Lee West Track Selection

combined tracks		forward tracks	
$p_t$	$> 0.150 \text{ GeV}/c$	$p_t$	$> 0.150 \text{ GeV}/c$
$\theta$	$> 0.0^\circ$	$\theta$	$> 6.0^\circ$
	$< 180.0^\circ$		$< 25.0^\circ$
$R_{start}$	$< 50.0 \text{ cm}$	$R_0$	$< 10.0 \text{ cm}$
$ DCA $	$< 5.0 \text{ cm}$	$\chi^2_{trackfit}$	$< 10.0$
central tracks		$\chi^2_{vertexfit}$	$< 25.0$
$p_t$	$> 0.150 \text{ GeV}/c$	$N_{prim+sec}$	$\geq 1$
$\theta$	$> 20.0^\circ$	$N_{planar+radial}$	$\geq 2$
	$< 160.0^\circ$	$\sigma_p/p$	$< 1$
$ DCA $	$< 2.0 \text{ cm}$		
$R_{start}$	$< 50.0 \text{ cm}$		
track length	$> 10.0 \text{ cm for } \theta < 150^\circ$		
track length	$> 5.0 \text{ cm for } \theta > 150^\circ$		

**Table A.1:** Track selection cuts.

The following abbreviations have been used in the above table:

- $p_t$ : transverse momentum
- $\theta$ : polar angle
- $R_0$ : radial distance to the nominal H1 primary vertex
- $\chi^2_{trackfit}$ :  $\chi^2$  of the track fit to the drift chamber hits
- $\chi^2_{vertexfit}$ :  $\chi^2$  of the primary vertex fit
- $N_{prim+sec}$ : number of primary and secondary forward tracker segments
- $N_{planar+radial}$ : number of planar and radial forward tracker segments
- $\sigma_p/p$ : relative error of momentum measurement
- $R_{start}$ : radial distance of the first hit to the z-axis

## Appendix B

# Lee West Muon Selection

forward endcap		backward endcap	
$\rho_x$	$< 100$ cm	$\rho_x$	$< 100$ cm
$\rho_y$	$< 100$ cm	$\rho_y$	$< 100$ cm
$N_{layers}$	$\geq 6$	$N_{layers}$	$\geq 6$
$i_{firstlayer}$	$\leq 5$	$i_{firstlayer}$	$\leq 8$
$i_{lastlayer}$	$\geq 6$	$i_{lastlayer}$	$\geq 3$
barrel		calorimeter muons	
$\rho$	$< 100$ cm	quality class $Q_c$	$\geq 2$
$z_0$	$< 100$ cm	separation angle	$> 12^\circ$
$N_{layers}$	$\geq 2$		
$i_{firstlayer}$	$\leq 5$		
$i_{lastlayer}$	$\geq 2$		

**Table B.1:** Muon selection cuts

The following abbreviations have been used in the above table:

- $\rho, \rho_x, \rho_y$ : radial distance of the extrapolated iron track to the primary vertex and its x- and y- component
- $z_0$ : z-coordinate at the iron tracks starting point
- $N_{layers}$ : number of hit iron layers (not including the boxes)
- $i_{firstlayer}, i_{lastlayer}$ : Number of the first/last hit iron layer

## Appendix C

# Definition of Subtriggers and Trigger Elements

Table C.1 shows the definition of all subtriggers which are relevant for this analysis. Tables C.2, C.3 and C.4 list the trigger elements of the instrumented iron, the tracking chambers and the remaining relevant trigger elements. In these tables the symbols  $\parallel$  and  $\&\&$  have been used for a logical *or* and logical *and*.

ST	definition	avg. prescale
S15	(Mu_ECQ $\parallel$ Mu_Bar) $\&\&$ DCR_Ph-Ta $\&\&$ zVtx_Sig	1.165
S19	Mu_Bar $\&\&$ DCR_Ph_CNH $\&\&$ zVtx_Sig>1	1.247
S22	Mu_ECQ $\&\&$ DCR_Ph_CNH $\&\&$ zVtx_Sig>1	1.247
S56	Mu_Any $\&\&$ DCR_Ph-Ta $\&\&$ (SPCLE_IET>1 $\parallel$ SPCLe_IET_Cen_2)	1.000
S87	Mu_Any $\&\&$ DCR_Ph-Ta $\&\&$ (LU_ET_44 $\parallel$ eTag)	1.003

**Table C.1:** Definition and average prescale factors of the relevant subtriggers for this analysis. Some veto trigger elements have been omitted for simplicity.

TE	description
Mu_Bar	barrel
Mu_FIEC	forward inner endcap
Mu_FOEC	forward outer endcap
Mu_BIEC	backward inner endcap
Mu_BOEC	backward outer endcap
Mu_2_BIoIEC	backward inner or outer endcap
Mu_ECQ	abbreviation for Mu_FOEC  Mu_BOEC  Mu_2_BIoIEC
Mu_Any	abbreviation for Mu_ECQ  Mu_FIEC

**Table C.2:** Trigger elements of the instrumented iron.

TE	description
DCR_Ph_Ta	at least one mask fired ( $p_t > 450$ MeV)
DCR_Ph_Tc	at least three masks fired ( $p_t > 450$ MeV)
DCR_Ph_Tneg	at least one negative mask fired ( $p_t > 450$ MeV)
DCR_Ph_Thig	at least one mask $p_t \geq 800$ MeV fired

**Table C.3:** Trigger elements of the tracking chambers.

TE	description
LU_ET_44	Electron tagger at $z = -44$ m
eTag	Electron tagger at $z = -33$ m
zVtx_sig	z-vertex histogram significance
zVtx_sig>1	z-vertex histogram good significance
SPCLe_IET>1	Spacal inclusive electron trigger, $E_{threshold} = 2$ GeV
SPCLe_IET_Cen_2	same as SPCLe_IET>1, but for central region

**Table C.4:** Other relevant trigger elements.

# Appendix D

## Event Class 24

Events are assigned to one or more event classes on L5 (event classification). The present analysis selects events from class 24. The definition of class 24 is summarized here. The following abbreviations are used:

- $z_0$ :  $z$ -coordinate at the point closest to the nominal primary vertex in the  $r\phi$  plane
- $R_{start}$ : radial distance of the first hit to the  $z$ -axis
- $N_{planar\ segments}$ : number of hit planar FTD segments
- $N_{segments}$ : number of hit planar and radial FTD segments
- $\theta_{vertex}$ : polar angle of the vertex fitted track
- $p, p_t$ : momentum and transverse momentum
- $\chi^2_{track\ fit}$ :  $\chi^2$  of the track fit
- $\chi^2_{vertex\ fit}$ :  $\chi^2$  of the vertex fit
- NDF: number of degrees of freedoms
- $R_0$ : radial distance of the non vertex fitted track to the nominal primary vertex
- $\rho$ : radial distance of the extrapolated iron track to the primary vertex
- $N_{layers}$ : number of limited streamer tube chamber layers, not including the so called boxes (layers outside the iron return yoke)
- $z_{vertex}$ :  $z$ -component of the primary event vertex
- $\chi^2_{fit}$ :  $\chi^2$  of the FMD track fit
- $\phi_{first\ hit}, \phi_{last\ hit}$ : azimuthal angle of the 1st/last iron hit
- $P(\chi^2)$ : "probability" of the inner/outer track link

<b>selection criteria of the muon class</b>	
• 1 muon (identified in the instr. iron or FMD)	or
• $\geq 2$ muons (identified in instr. iron, FMD or LAr-calorimeter)	or
• 1 muon and $\leq 5$ additional tracks in CJC/FTD	or
• 1 lepton and exactly 1 more track in CJC/FTD	
<b>tracks in CJC/FTD</b>	
• vertex fitted track only with $ z_0  \leq 40$ cm	and
• central tracks: $\geq 10$ hits in CJC/FTD	and
$R_{start} < 50$ cm	and
• forward tracks: $N_{planar\ segments} \geq 1$	and
$N_{segments} \geq 2$ for $\theta_{vertex} \leq 20^\circ$	and
$p \geq 1.0$ GeV	and
$p_t \geq 0.150$ GeV	and
$\chi^2_{track\ fit}/NDF \leq 10.0$	and
$\chi^2_{vertex\ fit}/NDF \leq 50.0$	and
$R_0 \leq 10$ cm	and
• combined tracks: no further cuts	
<b>tracks in muon system</b>	
• iron track with $\rho \leq 100$ cm	and
$N_{layers} \geq 6/2/3$ (FEC/Barrel/BEC)	or
• FMD track with $-400 \text{ cm} \leq z_{vertex} \leq 300$ cm	and
$\chi^2_{fit} \leq 20$	and
$ \phi_{first\ hit} - \phi_{last\ hit}  \leq 1.0$ rad	
<b>link of inner and outer track</b>	
• $P(\chi^2) > 0.0001$	
<b>lepton identification in LAr-calorimeter</b>	
• muon: $Q_c \geq 2$	
• electron: $Q_c \geq 2$	

**Table D.1:** Definition of class 24 in the data taking period 1997.

## Appendix E

# Monte Carlo Generators

The settings which have been used for Monte Carlo generation are summarized in table E.1. The generated Monte Carlo files are listed in table E.2.

generator	option	value
EPJPSI	proton PDF	MRS $A'$
	photon PDF	GRV-G LO
	relativistic corrections	on
	initial parton shower	on
	final parton shower	off
	$\alpha_s$	fixed, $\alpha_s = 0.3$
	width of $J/\psi$	QCD corrected
	scale for PDFs	$m_{J/\psi}^2$
	software version	33
DIFFVM	slope parameter $b$	4.8 (elas.)/ 1.6 (diss.)
	$\varepsilon$ (intercept-1)	0.225
	$n$	3.0
	$\Lambda$	3.0 GeV
	$\zeta$	1.0
	$\chi$	0.0
	$\alpha'$	0.0
	software version	10

**Table E.1:** Monte Carlo generator settings used in the present analysis.

file	generator	# of events	intrinsic $\sigma_{ep}$ [nb]
97/JPSIBGFMU...	EPJPSI	40000	11.45
97/resolv_inips...	EPJPSI	20000	1.787
bbbar10000	EPJPSI	10000	0.104
97/JPSIELAS4.MUMU...	DIFFVM	20000	815
97/JPSIPDIS4.MUMU...	DIFFVM	20000	786

**Table E.2:** Generated Monte Carlo files.

# List of Figures

1.1	Layout of HERA and its pre-accelerators. . . . .	8
1.2	Side view of the H1 detector . . . . .	9
1.3	Side view of the tracking chambers. . . . .	10
1.4	Modules of the instrumented iron. . . . .	11
1.5	Schematic view of the luminosity system. . . . .	12
1.6	Principle of operation of the z-Vertex Trigger. . . . .	14
1.7	Principle of operation of the Spacal IET trigger. . . . .	15
2.1	Level diagram of the system of charmonium bound states . . . . .	18
2.2	HERA coordinate system and Feynman diagram for $ep$ scattering. . . . .	19
2.3	Feynman diagrams for photon gluon fusion . . . . .	21
2.4	Number of photon gluon fusion events generated with EPJPSI as a function of $z$ , $W_{\gamma p}$ and $p_{t,J/\psi}$ . . . . .	22
2.5	Recent parameterizations of parton density functions . . . . .	23
2.6	Feynman diagrams for resolved photon processes . . . . .	24
2.7	Polar angle and momentum distribution of the decay leptons . . . . .	24
2.8	Number of resolved events generated with EPJPSI as a function of $z$ , $W_{\gamma p}$ and $p_{t,J/\psi}$ . . . . .	26
2.9	Selection efficiency as a function of $z$ , $W_{\gamma p}$ and $p_{t,J/\psi}$ determined from resolved photon Monte Carlo . . . . .	27
2.10	$x_\gamma$ and $x_g$ distribution for resolved photon events . . . . .	28
2.11	Number of $B \rightarrow J/\psi + X$ decays generated with EPJPSI as a function of $z$ , $W_{\gamma p}$ and $p_{t,J/\psi}$ . . . . .	29
2.12	Feynman diagrams for $J/\psi$ meson production in fragmentation. . . . .	30
2.13	Feynman diagrams for diffractive processes . . . . .	31
2.14	Number of diffractive proton dissociative events generated with DIFFVM as a function of $z$ , $W_{\gamma p}$ and $p_{t,J/\psi}$ . . . . .	32
2.15	Lepton pair production via two photon exchange . . . . .	33
3.1	Reconstruction of the kinematic variables $z$ and $W_{\gamma p}$ . . . . .	36
3.2	$z$ and $W_{\gamma p}$ bin purities . . . . .	37
3.3	$y_{j\bar{b}}$ compared to the electron method . . . . .	38
3.4	Reconstruction of the kinematic variable $x_\gamma$ . . . . .	39

3.5	Generated $Q^2$ distribution of a boson gluon fusion Monte Carlo for photoproduction and DIS events. . . . .	40
3.6	Invariant mass resolution for $J/\psi$ mesons with muons in the forward direction . .	41
3.7	Reconstruction efficiency of the forward muon detector in data and Monte Carlo	42
4.1	Display of a resolved photon candidate event . . . . .	46
4.2	Display of an elastic candidate event . . . . .	47
4.3	Lepton identification efficiency in data and Monte Carlo . . . . .	48
4.4	Invariant mass spectrum . . . . .	49
4.5	Number of $J/\psi$ candidates per luminosity . . . . .	50
4.6	Invariant mass spectrum for the relevant subtriggers . . . . .	51
4.7	Subtrigger efficiencies (S15,S19,S22) as determined from different Monte Carlos .	53
4.8	Subtrigger efficiencies (S56,S87,all) as determined from different Monte Carlos . .	54
4.9	Efficiencies of the instrumented iron's trigger elements . . . . .	55
4.10	Efficiency of the z Vertex histogram trigger elements . . . . .	56
4.11	Acceptance function of the electron taggers. . . . .	57
4.12	Efficiency of the neural network trigger. . . . .	58
4.13	Invariant mass signals for different $z$ ranges. . . . .	60
4.14	Comparison of data ( $z < 0.3$ ) and resolved photon Monte Carlo . Part A . . . . .	62
4.15	Comparison of data ( $z < 0.3$ ) and resolved photon Monte Carlo . Part B . . . . .	63
4.16	Comparison of data ( $0.3 < z < 0.9$ ) and photon gluon fusion Monte Carlo . Part A	64
4.17	Comparison of data ( $0.3 < z < 0.9$ ) and photon gluon fusion Monte Carlo . Part B	65
4.18	Comparison of data ( $z > 0.9$ ) and diffractive Monte Carlo . Part A . . . . .	66
4.19	Comparison of data ( $z > 0.9$ ) and diffractive Monte Carlo . Part B . . . . .	67
4.20	Expected number of events compared to data . . . . .	69
4.21	Comparison of data and mixed Monte Carlo . Part A . . . . .	70
4.22	Comparison of data and mixed Monte Carlo . Part B . . . . .	71
5.1	Total selection efficiency with different PDFs . . . . .	76
5.2	$\gamma p$ cross section as a function of $W_{\gamma p}$ . . . . .	78
5.3	Invariant mass signal in bins of $W_{\gamma p}$ . . . . .	79
5.4	Invariant mass signal in bins of $z$ . . . . .	81
5.5	Differential $\gamma p$ cross section as function of $z$ for $40 < W_{\gamma p} < 300$ GeV compared to higher order predictions . . . . .	82
5.6	Differential $\gamma p$ cross section as function of $z$ for $40 < W_{\gamma p} < 300$ GeV compared to leading order predictions . . . . .	83
5.7	Differential $\gamma p$ cross section as a function of $z$ for $90 < W_{\gamma p} < 300$ GeV . . . . .	84
5.8	$\gamma p$ cross section as a function of $W_{\gamma p}$ for $0.4 < z < 0.9$ and $p_{t,J/\psi} > 1$ GeV . . . . .	86
5.9	Differential $\gamma p$ cross section as function of $z$ . . . . .	87
5.10	Differential $\gamma p$ cross section as function of $p_{t,J/\psi}^2$ . . . . .	88

# List of Tables

1.1	HERA technical figures. . . . .	7
1.2	Spacial performance figures. . . . .	11
2.1	Influence of different polar angle and momentum cuts for the decay leptons . . .	25
2.2	Values of the color octet matrix elements . . . . .	34
4.1	Cuts used in the final data selection . . . . .	45
4.2	Run ranges. . . . .	46
4.3	Number of events per subtrigger combination . . . . .	52
4.4	Effective prescale weight . . . . .	59
5.1	Integrated photon flux per $W_{\gamma p}$ range . . . . .	75
5.2	Systematic errors in the determination of cross sections. . . . .	75
5.3	Numbers for the determination of the $W_{\gamma p}$ cross section for $p_{t,J/\psi} > 1$ GeV . . .	77
5.4	Numbers for the determination of the differential cross section as a function of $z$ for $p_{t,J/\psi} > 1$ GeV and $40 < W_{\gamma p} < 300$ GeV . . . . .	80
5.5	Leading and higher order predictions by Kniehl and Kramer in the low $z$ range .	80
A.1	Track selection cuts . . . . .	91
B.1	Muon selection cuts . . . . .	92
C.1	Definition of the relevant subtriggers for this analysis . . . . .	93
C.2	Trigger elements of the instrumented iron . . . . .	94
C.3	Trigger elements of the tracking chambers . . . . .	94
C.4	Other trigger elements . . . . .	94
D.1	Definition of class 24 in the data taking period 1997. . . . .	96
E.1	Monte Carlo generator settings used in the present analysis. . . . .	97
E.2	Generated Monte Carlo files. . . . .	97

# Bibliography

- [1] H1 Collaboration, *The H1 detector at HERA*, Nuclear Instruments and Methods in Physics Research, Section A 386 (1997) 310-347
- [2] H1 Collaboration, *The tracking, calorimeter and muon detectors of the H1 experiment at HERA*, Nuclear Instruments and Methods in Physics Research, Section A 386 (1997) 348-396
- [3] H1 Collaboration, *Guide to Simulation Program H1SIM*, October 1991
- [4] J.E. Augustin et al., Physics Review Letters 33 (1974) 1406
- [5] J.J. Aubert et al., Physics Review Letters 33 (1974) 1404
- [6] E. Leader, E. Predazzi, *An Introduction to Gauge Theories and Modern Particle Physics*, Cambridge University Press, 1996
- [7] Leonid Frankfurt, *Diffraction Heavy Quarkonium Photo- and Electroproduction in QCD*, hep-ph/9702216v4, February 1997
- [8] Geoffrey T. Bodwin, Eric Braaten, G. Peter Lepage *Rigorous QCD analysis of inclusive annihilation and production of heavy quarkonium*, Phys. Review D, Vol. 51, No. 3, February 1995
- [9] Eric Braaten, *Production of Heavy Quarkonium in High Energy Colliders*, hep-ph/9602374, February 1996
- [10] Gerhard A. Schuler, *Systematics of Quarkonium Production*, hep-ph/9606410, June 1996
- [11] Stephan Schiek, *Untersuchung der inelastischen Photoproduktion von  $J/\psi$ -Mesonen im H1-Detektor bei HERA*, PhD thesis, Hamburg 1996
- [12] Katja Krüger, *Inelastische Produktion von  $J/\psi$ -Mesonen am Speicherring HERA*, Diploma thesis, September 1997
- [13] Hannes Jung, *Monte Carlo Generator EPJPSI for  $J/\psi$  mesons in high energy  $\gamma p$ ,  $ep$ ,  $\mu p$ ,  $p\bar{p}$  and  $pp$  collisions*, Documentation, September 1994
- [14] G.A. Schuler, *Theoretical aspects of low- $Q^2$  physics at HERA*, CERN-TH-6427-92, March 1992
- [15] Michael Krämer, *Inclusive  $J/\psi$  Photoproduction at HERA*, hep-ph/9707449, July 1997
- [16] Particle Data Group, *Review of Particle Physics*, July 1996

- 
- [17] Bernd Kniehl, Gustav Kramer *Tevatron-HERA Colour Octet Charmonium Anomaly Versus Higher-Order QCD Effects*, hep-ph/9803256, March 1998
- [18] S. Frixione, M.L. Mangano, P. Nason, G. Ridolfi, *Total Cross Sections For Heavy Flavour Production at HERA*, Phys. Lett. B348 (1995) 633
- [19] Martin Kander, *Bestimmung des ep-Wirkungsquerschnittes von Beauty-Quarks durch ihren semi-leptonischen Zerfall in Myonen mit dem H1-Detektor bei HERA*, PhD thesis Hamburg, June 1998
- [20] J.C. Collins, D.E. Soper, *The Theorems of Perturbative QCD*, Ann. Rev. Nucl. Part Sci., 37:383 (1987)
- [21] Bernd A. Kniehl, Gustav Kramer, *Color-Octet Contributions to  $J/\psi$  Photoproduction via Fragmentation at HERA*, DESY 97-036, hep-ph/9703280, March 1997
- [22] J.J. Sakurai, M. Gell-Mann, F. Zachariasen, *Form-Factors and Vector Mesons*, Ann. Phys. (NY) (1960) 1, Phys. Rev. 124 (1961) 953
- [23] A. Donnachie, *Soft Interactions*, hep-ph/9703366, March 1997
- [24] B. Cano-Coloma, M.A. Sanchis-Lozano *Charmonia Production in Hadron Colliders and the Extraction of Colour-Octet Matrix Elements*, hep-ph/9706270, June 1997
- [25] K. Sridhar, A.D. Martin, W.J. Stirling  *$J/\psi$  production at the Tevatron and HERA: the effect of  $k_t$  smearing*, hep-ph/9806253, June 1998
- [26] P. Cho and A.K. Leibovich, *Color Octet Quarkonia Production II*, hep-ph/9511315, April 1996
- [27] Andreas Meyer, *Measurement of the Structure Function  $F_2(x, Q^2)$  of the Proton at Low  $Q^2$  with the H1 Detector at HERA using the New Detector Components Spacal and BDC*, PhD thesis Hamburg, October 1997
- [28] Lee West, *How to use the Heavy Flavour Working Group Track, Muon and Electron Selection Code*, December 2, 1997
- [29] B. Naroska, S. Schiek, G. Schmidt, *Lepton Identification in the H1 Detector at Low Momenta*, Internal H1 note 05/97-518
- [30] H1 Collaboration, *Photo-production of  $\psi(2S)$  mesons at HERA*, Physics Letters B, 421 (1998) 385-394
- [31] V. Andreev, *Acceptance Determination of Electron Tagger*, H1 internal note, October 1996
- [32] Sergej Levonian, *Help for the e-tagger related analyses*, H1 WWW detector documentation, December 1997
- [33] Susanne Mohrdieck, *Neuronaler Netzwerktrigger für Myonen im H1 Detektor bei HERA*, Diploma thesis, August 1997
- [34] MPI Munich, *Netsim User Manual*, documentation, November 1997
- [35] Helge Wollatz, *Private communication*, October 1998

- 
- [36] S. Egli, *Calculating Event Weights in Case of Downscaling on Trigger Levels 1-4*, H1 internal note H1-04/97-517, April 1997
- [37] Arnd Meyer, *Charmonium Production in Deep Inelastic Scattering at HERA*, PhD thesis, April 1998
- [38] John R. Smith, *An Experimentalist's Guide to Photon Flux Calculations*, H1 internal note H1-12/92-259, December 1992
- [39] A. Rostovtsev, *Corrections to the Weizsäcker-Williams Approximation of Photon Flux in ep Collisions*, H1 internal note H1-08/93-309, August 1993
- [40] ZEUS Collaboration, *Measurement of Inelastic  $J/\psi$  Photoproduction at HERA*, Talk submitted to ICHEP98 Vancouver, 23-29 July 1998
- [41] M. Beneke, *Inelastic Photoproduction of polarised  $J/\psi$* , hep-ph/9709376, Sept. 1997
- [42] G.D. Lafferty, *Where to Stick Your Data Points: The Treatment of Measurements Within Wide Bins*, CERN-PPE/94-72, May 1994
- [43] Sean Fleming, *Leptoproduction of  $J/\psi$* , hep-ph/9707365, July 1997
- [44] G. Zweig, *An  $SU(3)$  Model for Strong Interaction Symmetry and its Breaking*, CERN-Report, CERN-TH-412, 1964
- [45] F. Lehner, *Bestimmung und QCD-Analyse der Protonstrukturfunktion  $F_2(x, Q^2)$  bei kleinen Bjorken- $x$  und  $Q^2$  mit Hilfe des verbesserten Rückwärtsbereichs des H1-Detektors*, DESY PhD thesis, March 1998
- [46] B. Kniehl, *Private communication, Predictions based on [17]*, October 1998
- [47] P. Cho and A.K. Leibovich, *Color Octet Quarkonia Production*, Phys. Rev. D53 (1996) 150, hep-ph/9505329, May 1995
- [48] Katja Krüger, *Private communication*, October 1998

# Danksagung

Bei Frau Prof. Naroska bedanke ich mich für die interessante Aufgabenstellung und die hervorragende Betreuung während der Zeit meiner Diplomarbeit. Herrn Prof. Volker Blobel danke ich für die Übernahme des Gutachtens. Herrn Prof. Georg Zimmerer danke ich für die Erlaubnis, die Diplomarbeit in englischer Sprache verfassen zu dürfen.

Ein besseres Verständnis physikalischer Zusammenhänge verdanke ich Diskussionen mit Katja, Arnd und der ganzen F22 Gruppe. Christopher Hilton, Katja, Nicole und Niels danke ich fürs aufmerksame Korrekturlesen. Tim war immer zur Stelle, wenn Linux streikte. Und dann gab's da noch die Kaffeerunde, die ich sehr vermissen werde...

Meinen Eltern danke ich für die Ermöglichung des Studiums.

## Erklärung

Hiermit versichere ich, diese Arbeit selbständig und nur unter Verwendung der angegebenen Quellen verfaßt zu haben.